# Modulated gates for improved ion control

A master's thesis submitted to the faculty of mathematics, computer science and physics, of the University of Innsbruck in partial fulfillment of the requirements for the degree of

Master of Science (MSc)

carried out at the Institute of Experimental Physics under the supervision of

Ass.-Prof. Dr. Thomas Monz

presented by

Florian Kofler



Institute for Experimental Physics University of Innsbruck July 2025

### **Abstract**

Quantum systems and their utility for quantum information processing rely critically on our ability to isolate them from the environment while simultaneously admitting control fields to drive coherent evolution. These two requirements are intrinsically at odds and much effort has been devoted to reconcile the two. In state-of-the-art quantum information processors environmental shielding is now often so effective that the main contributors to noise are introduced via the control fields themselves. In this work, we apply a technique from optimal control to mitigate experimental imperfections in the coherent control of quantum systems, specifically calcium-40 ions in a linear Paul trap. To this end, we enable control over additional degrees of freedom in the radio frequency pulse-generation and integrate this functionality into the existing experimental control software using the ARTIQ and Sinara ecosystem. Among several competing modulation techniques, we opt for a balanced Gaussian amplitude modulation scheme for the two-qubit entangling gate based on the Mølmer-Sørensen interaction, which has previously been shown to reduce the unwanted effects of mode crowding in the literature. The choice of this technique was informed by the characterization of the control electronics and a numerical simulation was implemented to aid the parameter selection for experimental calibration scans. A calibration technique was introduced to enable the time-efficient calibration of all 120 pairs in a 16-ion chain, leading to a mean state preparation fidelity of  $98.48^{+0.48}_{-0.47}\%$ , thus surpassing the previous entangling gate implementation's  $97.90^{+0.52}_{-0.47}\%$ .

# Zusammenfassung

Der Nutzen von Quantensystemen für die Quanteninformationsverarbeitung hängt entscheidend von der Fähigkeit ab, sie von der Umgebung zu isolieren und gleichzeitig externe Kontrollfelder zuzulassen, welche eine kohärente Manipulation des Zustands ermöglichen. Diese beiden Anforderungen stehen sich jedoch diametral gegenüber und es benötigt erheblichen Aufwand sie miteinander in Einklang zu bringen. In hochmodernen Quanteninformationsprozessoren ist die Abschirmung des Quantensystems von der Umgebung mittlerweile so effektiv, dass die Kontrollfelder selbst einen der größten Beiträge zum Rauschen liefern. In dieser Arbeit wenden wir eine Technik der optimalen Steuerung an, um experimentelle Imperfektionen der kohärenten Kontrolle von Calcium-40-Ionen in einer linearen Paulfalle zu reduzieren. Die Kontrolle zusätzlicher Freiheitsgrade bei der Erzeugung von Radiofrequenzpulsen wird dafür ermöglicht und diese Funktionalität in die bestehende, experimentelle Kontrollsoftware unter Verwendung des ARTIQund Sinara-Ökosystems integriert. Für das zwei-Qubit-Verschränkungsgatter basierend auf der Mølmer-Sørensen-Wechselwirkung entschieden wir uns unter zahlreichen Modulationstechniken für eine ausgeglichene Gauß-Amplitudenmodulation. Im Experiment konnte diese Technik bereits zeigen, dass sie die unerwünschten Auswirkungen der Modenverdichtung nachweislich reduziert. Die Wahl dieser Technik wurde durch die Charakterisierung der Radiofrequenz-Hardware begründet und zudem wurde eine numerische Simulation implementiert, um die Parameterauswahl für experimentelle Kalibrierungsscans zu unterstützen. Die zeitsparende Kalibrierung aller 120 Paare in einer 16 Ionen Kette wird durch die Einführung einer Kalibrierungstechnik ermöglicht, mit deren Hilfe eine mittlere Zustandspräparationsgüte von  $98.48^{+0.48}_{-0.47}\%$  erreicht wurde. Das erzielte Ergebnis stellt somit eine Verbesserung gegenüber dem Wert von  $97.90^{+0.52}_{-0.47}\%$  der vorherigen Gatterimplementierung dar.

# **Acknowledgements**

I want to start this thesis by thanking all people who supported me during my course of studies and during my Master's thesis project, the people who made this whole project possible.

First I want to thank my supervisor Thomas Monz for giving me the opportunity to carry out my Master's project in his group on a cutting-edge experimental platform, for providing me with a topic I really enjoyed working on, and for correcting my thesis.

Being part of the AQTION team over the course of the last 1 1/2 years was a great joy, and I am really grateful for the experience. I want to thank Christian Marciniak for always having time to answer my countless questions about the project and physics in general, for helping me steer the project in the right direction, and for proofreading my thesis and spotting the many (and sometimes also unintentionally hilarious) errors I managed to include. I would also like to thank Ivan Pogorelov for introducing me to the topic of modulated gates, showing me the previous work that has been carried out on the topic and helping me with his experience on how gates work on the setup.

The measurements on the setup wouldn't have been possible without the help of Alex Steiner, Robert Freund and Marcel Meyer, who not only supported me tirelessly during the experimental runs, but also made the lab time genuinely fun and were just as emotionally invested as me in hoping that the gates would finally behave as expected.

A big thank you also goes out to the people in the AG Quantum Optics and Spectroscopy and to my office mates for the many interesting discussions we had, to Norman Krackow for all his help regarding Sinara and ARTIQ, and everyone at AQT who kindly helped in answering my sometimes rather simple coding related questions.

One of the main reasons I truly enjoyed studying physics was my group of study colleagues, who not only managed to make even the toughest problem sheets and projects surprisingly entertaining, but also made the time outside university genuinely memorable.

Most importantly, I want to thank my parents for their unwavering support and encouragement in all of my pursuits over the years, and I want to dedicate this work to "Omi" for always believing in me from early on, your belief in me has been a constant source of strength.

Thank you all!

# Contents

Ta	Table of contents				
1. Introduction					
2.	Theoretical framework				
	2.1. Control theory	3			
	2.2. Quantum optimal control theory	5			
	2.2.1. Quantum information processing	5			
	2.2.2. Light-matter interaction	7			
	2.2.3. Physical constraints and performance measure	18			
	2.3. Ion trap quantum computing platform	20			
	2.3.1. Linear Paul trap and motional modes	20			
	$2.3.2.$ $^{40}\mathrm{Ca^{+}}$ as a qubit	22			
	2.3.3. AC-stark shift compensation	24			
3.	Experimental setup	27			
	3.1. Radio frequency generation and control	27			
	3.2. Coherent operations with 729 nm laser	29			
4.	Frequency-robust entangling gate using amplitude modulation	32			
	4.1. Limitations of current setup	32			
	4.2. Theoretical motivation	37			
	4.3. Numerical optimization	40			
	4.4. Experimental calibration procedure	43			
<b>5</b> .	Characterization of the ARTIQ and Sinara ecosystem	44			
	5.1. RF generation capabilities	44			
	5.2. Phaser device characteristics	45			
6.	Experimental results	50			
	6.1. Experimental results for a 2-ion chain	50			
	6.2. Experimental results for a 16-ion chain	53			
<b>7</b> .	. Conclusion and outlook				
Α.	A. Analysis method for parity oscillations				
В.	B. Bihliography				

# 1. Introduction

Mounting inconsistencies between empirical observations and the predictions of classical physics emerged at the turn of the 20th century, hinting at the incomplete nature of the prevailing theory at the time. Noteworthy examples include the prediction of an ultraviolet catastrophe for black-body radiation and the inability to describe the stability of atoms. These discrepancies could only be reconciled with the advent of quantum physics in the first half of the 20th century, which offered a mathematical way to accurately describe and model problems at the atomic scale. Beyond advancing humanity's collective understanding of nature to new regimes, the theory also laid the groundwork for various technological innovations to come.

In the so called *first quantum revolution*, these newfound insights were used to construct entirely new types of devices, marking the beginning of the information or silicon age. The name comes from the transistor, a semiconductor device made out of pure<sup>1</sup> silicon that acts as an electronic switch, with modern computer chips containing billions of them. Enabled by the invention of the laser, photolithography played a key role in the continuous miniaturization of transistors over the last few decades, leading to a significant increase in computational capabilities [2]. However the rate of progress is slowing, as it becomes ever more difficult (and expensive) to create smaller transistors. This necessitates research into new production methods in addition to the exploration of different computational models.

Rather than building devices based on insights gained from quantum mechanics, the emphasis of the second quantum revolution is on the direct manipulation of single quantum systems, with the focus in this thesis being on quantum computers as a new computational paradigm [3]. The underlying idea is to create an engineered quantum system and harness its quantum properties like entanglement in such a way that its capabilities significantly surpass those achievable on a completely classical system. For example the Shor Algorithm promises a superpolynomial speedup in finding the prime factors of an integer when compared to the best known classical algorithm [4]. For this to work however, the quantum system needs to be well isolated from its surrounding environment such that it retains its desirable properties, while at the same time being amenable to control by external fields for the manipulation of its state. Significant effort has been devoted to bringing those two opposing requirements together to realize quantum computers capable of solving relevant problems.

Given that information is a physical entity as described in the similar titled reference [5], quantum information can be encoded into several different physical systems. One of the first quantum computing platforms was realized in 1998 using Nuclear Magnetic Resonance techniques [6] with other platforms soon following suit. Among the most promising and matured platforms to date are superconducting circuits [7], neutral atoms [8], and trapped-ions [9, 10]. The latter one is used in this thesis to encode a quantum mechanical two-level system or quantum bit (qubit) into two electronic states of  $^{40}\text{Ca}^+$ . Multiple ions are trapped in a linear string by means of time-

<sup>&</sup>lt;sup>1</sup>Silicon wafers always contain trace impurities, but the requirement for advanced semiconductors is a purity of 12 Nines (12N), meaning that at most one out of a trillion atoms is non-silicon [1].

#### 1. Introduction

varying electric fields created with a Paul trap and their quantum state is manipulated with laser beams. Incidentally, these control fields are also one of the main contributors to errors because the shielding of the quantum system from the environment is sufficiently high in state-of-the-art quantum information processors.

This becomes particularly evident in our experimental platform where all ions are confined within a single trapping potential. In this system, one of the key limitations for two-qubit entangling gates based on the Mølmer Sørensen interaction is radial mode crowding, which leads to residual spin-motion entanglement. This issue becomes more pronounced in larger ion chains and limits scaling efforts in our system. Hence the focus of this thesis is on the implementation of an optimal control technique as a way to realize quantum gates exceeding the performance of the current implementation. This directly addresses one of the main outstanding challenges in quantum computing, namely scaling up the number of qubits while at the same time reducing errors induced by the control field, with the latter being of primary concern here.

The outline of this thesis is as follows: Chapter 2 presents the framework of control theory and its adaption to quantum information processing. In addition the relevant light-matter interaction responsible for the qubit state manipulation is presented, followed by a brief introduction of the ion trap quantum computing platform. The setup relevant for the execution of the two-qubit entangling gates is then outlined in Chap. 3, focusing on the radio frequency signal generation as well as the optical setup. Chapter 4 then presents the optimal control method of balanced frequency-robust entangling gates pursued in this thesis. It was chosen based on an analysis of the main error sources in the setup and a characterization of the capabilities and limitations of the radio frequency signal generation in Chap. 5. Experimental results for both a 2- and 16-ion chain are shown in Chap. 6. The thesis concludes in Chap. 7 with a summary and discussion of the obtained results as well as an outlook towards possible future improvements.

# 2. Theoretical framework

This chapter will summarize the theoretical foundation needed for this thesis by starting with a brief introduction to control theory in Sec. 2.1, which offers an abstract way of describing control problems. These concepts will then be mapped to quantum information processing in Sec. 2.2 and the chapter concludes in Sec. 2.3 with a focus on trapped-ion quantum computing as one particular platform for quantum information processing.

# 2.1. Control theory

In this section the basic terminology of control theory relevant to this thesis is introduced, starting with the definition of control systems and which components they consist of, followed by a comparison of open- and closed-loop control systems, and concluding with the problem of optimal control.

A control system is "an arrangement of physical components connected or related in such a manner as to command, direct, or regulate itself or another system" [11]. Given this definition, it is not surprising that control systems encompass a broad range of devices in reality, ranging from simple light switches for controlling a ceiling light, to thermostats for setting and regulating the room temperature all the way to complex control systems that are able to autonomously land a rocket on a drone ship.

All these mentioned control systems can be described by control theory under a unified framework and terminology, which is based on the components that are schematically shown in Fig. 2.1 and described following Ref. 12. Common to all control systems is the *plant* or *process*, which is the system over which one wants to exert control in a precise and reproducible manner. The plant is mathematically modelled in this thesis using first order ordinary differential equations of the form

$$\dot{\mathbf{s}}(t) = \mathbf{a}(\mathbf{s}(t), \mathbf{u}(t), t), \tag{2.1}$$

where the state vector  $\mathbf{s}(t) = (s_1(t), s_2(t), \dots, s_n(t))$  consists of n state variables  $s_i(t)$  describing the state of the plant at time  $t \in [t_i, t_f]$  between the initial  $t_0$  and final time  $t_f$ . In Fig. 2.1, the state of the plant  $\mathbf{s}(t)$  is referred to as *actual output*, which can be manipulated using m external control inputs  $u_j(t)$ , where the control vector containing all control inputs is defined as  $\mathbf{u}(t) = (u_1(t), u_2(t), \dots, u_m(t))$ .

The aim of control theory is to find a suitable control vector  $\mathbf{u}(t)$  such that the *actual output* matches the *desired output* of the plant. In particular, given a system state  $\mathbf{s}(t)$ , the *controller* computes a control signal that implements the necessary control inputs using one or multiple *actuators* to physically alter the state of the plant. If the control signal is computed correctly, this should move the actual closer to the desired output of the plant. A distinction has to be made between open- and closed-loop control systems, which differ in how the actual output is returned back to the controller.

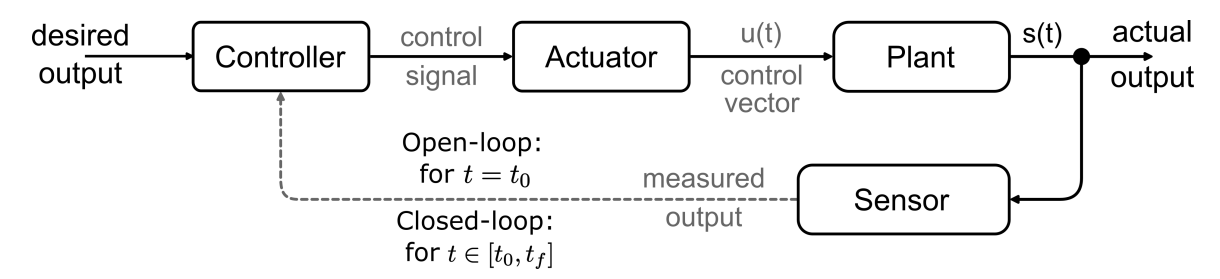


**Figure 2.1.:** Schematic overview of control loops. The goal is to physically alter the actual output of a plant by using actuators, which are fed a control signal that is calculated by a controller taking into account the desired and actual output. For open-loop control systems, only the initial state of the plant is considered whereas for closed-loop control systems the actual output for all times is fed back to the controller.

If the actual output  $\mathbf{s}(t)$  for  $t > t_0$  is fed back to the controller and is taken into account for computing the desired input control values, then one refers to the control system as closed-loop control system. Note that for this one has to measure the actual output with a *sensor*, which given its physical implementation alters the actual to a measured output and this systematic error needs to be taken into account. Closed-loop control systems possess the ability to find suitable control vectors  $\mathbf{u}(t)$  for arbitrary state vectors  $\mathbf{s}(t)$ . This allows these control systems to respond to externally induced changes to the plant and further minimize the time required to achieve the desired state. One disadvantage of closed-loop control systems is their potential instability, as the measured output is used for computing the control input and this can result in unstable behavior when the system design is not carefully chosen.

Open-loop control systems either assume a particular state for the initial time  $\mathbf{s}(t_0)$  or measure the actual output only for  $t_0$  with a sensor and compute the control input values given this assumed or measured state. As a consequence, an accurate model of the behaviour of the plant is needed for open-loop control systems in order to account for possible external perturbations occurring at times  $t > t_0$ . Since no feedback signal is used in the open loop controller, the ability of the model to reliably predict the behaviour of the plant has to be checked in a separate fashion. Given that open-loop control is evidently simpler in terms of implementation, it is preferable to use for systems whose behavior is thoroughly understood. What remains to be discussed is how the controller computes the control signal, which in turn corresponds to the control input signals manipulating the plant, and if there is an optimal solution for this problem.

Optimal control theory addresses this problem and aims to find a suitable control vector  $\mathbf{u}(t)$  by simultaneously adhering to system constraints and/or performance measures. System constraints in this context refer to admissible values for the state vector  $\mathbf{s}(t)$  and the control vector  $\mathbf{u}(t)$ . For the example of an automatic rocket landing, the velocities the rocket can reasonable withstand can be bounded from above as values higher than a threshold velocity would lead to the destruction of the rocket. The same holds for the control input values, where the limiting factor is that certain control input values cannot be realized given the set of available actuators. With this it becomes apparent that the formulation of an optimal control problem is an interplay between recognizing the boundaries of physically realized systems and incorporating those boundaries into a model that accurately predicts the system behaviour.

After modelling the physical system using differential equations and incorporating possible system constraints, there can often exist multiple solutions in terms of control input values for reaching a desired state given an actual state of the system. These solutions can differ in various aspects, for

example in the time it takes to reach the desired state given an initial state, and minimum-time problems aim to find the shortest time to achieve this. Furthermore in terminal control problems, the difference between the actually realized state of the plant at time  $t_f$  is compared to the desired state. In minimal control-effort problems a cost is assigned to required control input values in terms of how the duration of the assumed control input is related to energy expenditure (for example fuel or power consumption) or what impact changes of control input values have on the energy expenditure. Those performance criteria can be mathematically formulated by using a cost function J of the general form

$$J = h(\mathbf{s}(t_f), t_f) + \int_{t_0}^{t_f} g(\mathbf{s}(t), \mathbf{u}(t), t) \, \mathrm{d}t, \tag{2.2}$$

where h and g are scalar functions and the result for given control input values  $\mathbf{u}(t)$  and states  $\mathbf{s}(t)$  is a number. The goal of optimal control theory is to find control input values  $\mathbf{u}(t)$  that minimize the cost function globally by simultaneously adhering to the physical constraints of the system that should be modelled. Precisely these constraints are the reason why the existence of a solution is not guaranteed, as possible solutions may simply be unfeasible to achieve in a given system. In the next section we will map those concepts to quantum information processing.

## 2.2. Quantum optimal control theory

In this section, the concepts of control theory introduced in the previous section will be embedded into the context of quantum information processing. The necessary formalism to model the quantum system of interest is introduced in Sec. 2.2.1, followed by an overview of how the quantum state can be manipulated with light in Sec. 2.2.2. The section concludes with a brief discussion about physical constraints and the performance measures used in this thesis in Sec. 2.2.3.

#### 2.2.1. Quantum information processing

We will first introduce classical information processing and then proceed to quantum information processing in order to illustrate their difference. The treatment in this section draws from Ref. 13. The fundamental unit of information in classical computing is called binary digit or short bit, and it can only take one of two states 0 and 1 as the name suggests, without any intermediate states. This representation of information is advantageous when one considers that information is encoded in noisy physical signals. For example a single bit can be encoded into voltage signals, where a clear separation between a low and high voltage signal ensures the accurate differentiation between the two states even in the presence of noise. The quantum analog to the bit as the fundamental unit of information is called quantum bit or short qubit. One key difference to the bit is that the state of the qubit, which is represented by a quantum state vector  $|\psi\rangle$ , can not only assume the orthogonal basis states  $|0\rangle$  and  $|1\rangle$ , but also any superposition of them in the form

$$|\psi\rangle = \alpha |0\rangle + \beta |1\rangle,$$
 (2.3)

with coefficients  $\alpha, \beta \in \mathbb{C}$ . A measurement of the state vector  $|\psi\rangle$  projects it with probability  $p_0 = |\langle 0|\psi\rangle|^2 = |\alpha|^2$  into the state  $|0\rangle$  and with probability  $p_1 = |\langle 1|\psi\rangle|^2 = |\beta|^2$  into the state  $|1\rangle$ . For a normalized state vector  $|\langle \psi|\psi\rangle|^2 = 1$  the condition  $p_0 + p_1 = 1$  holds, such that the quantum state can be described by a unit vector in a complex vector space called Hilbert space H. The size of the Hilbert space is two-dimensional for a single qubit and in general is of finite-dimension

for the quantum information processing purposes used in this thesis. In addition to the states  $|0\rangle$  and  $|1\rangle$ , four other orthonormal basis states  $|\pm i\rangle$  and  $|\pm\rangle$  can be defined as follows:

$$|\pm i\rangle = \frac{1}{\sqrt{2}} (|0\rangle \pm i |1\rangle)$$
  $|\pm\rangle = \frac{1}{\sqrt{2}} (|0\rangle \pm |1\rangle)$  (2.4)

It is useful to describe the state vector  $|\psi\rangle$  of a single qubit in spherical coordinates and visualize it on the Bloch sphere as follows

$$|\psi\rangle = e^{i\chi} \left(\cos\frac{\theta}{2}|0\rangle + e^{i\varphi}\sin\frac{\theta}{2}|1\rangle\right),$$
 (2.5)

where the angle  $\theta$  and the phase  $\varphi$  uniquely define pure states lying on the surface of the Bloch sphere with radius 1. State vectors that posses equal values of  $(\theta, \varphi)$  but differ in their global phase  $\chi$  will yield the same measurement result. They are thus indistinguishable from each other with respect to their physical properties and hence the global phase can be omitted for practical purposes. The time evolution of the system for pure quantum states is described by the Schrödinger equation

$$i\hbar \frac{\mathrm{d}}{\mathrm{d}t} |\psi(t)\rangle = \hat{\mathcal{H}}(t) |\psi(t)\rangle$$
 (2.6)

where  $\hbar$  is the reduced Planck constant and  $\hat{\mathcal{H}}(t)$  the time-dependent Hamilton operator.

A quantum state can not only be described by a state vector  $|\psi\rangle$  but also by a density matrix  $\rho$  using the density matrix formalism. Both descriptions are mathematically equivalent for pure states  $\operatorname{tr}(\rho^2) = 1$  but the latter one is more convenient when describing for example ensembles of pure quantum states  $\{p_i, |\psi_i\rangle\}$  called mixed states

$$\rho \equiv \sum_{n} p_n |\psi_n\rangle\langle\psi_n|, \tag{2.7}$$

where  $p_n$  is the probability to find the system in the pure state  $|\psi_n\rangle$ , with the index n denoting all possible or considered states. The density matrix is a hermitian, positive semi-definite operator with  $\operatorname{tr}(\rho) = 1$  and it is describing a pure state if  $\operatorname{tr}(\rho^2) = 1$  and a mixed state if  $\operatorname{tr}(\rho^2) < 1$ . It can be shown that every density matrix for qubits can be expressed in term of its Bloch vector  $\mathbf{r} = (r_x, r_y, r_z)^{\top}$  representation

$$\rho = \frac{\mathbb{1}_2 + \mathbf{r} \cdot \boldsymbol{\sigma}}{2} = \frac{1}{2} \begin{pmatrix} 1 + r_z & r_x - ir_y \\ r_x + ir_y & 1 - r_z \end{pmatrix}$$
(2.8)

by using the two-dimensional identity matrix  $\mathbb{1}_2$  and the trace-less Pauli matrices  $\boldsymbol{\sigma} = (\sigma_x, \sigma_y, \sigma_z)$  defined as

$$\sigma_x = \begin{pmatrix} 0 & 1 \\ 1 & 0 \end{pmatrix}, \qquad \sigma_y = \begin{pmatrix} 0 & -i \\ i & 0 \end{pmatrix}, \qquad \sigma_z = \begin{pmatrix} 1 & 0 \\ 0 & -1 \end{pmatrix}.$$
 (2.9)

With that an arbitrary single qubit state can be represented on the Bloch sphere by either using Eq. 2.5 for a pure state lying on the surface of the Bloch sphere with radius 1, or Eq. 2.8 for a mixed state that will lie within the sphere. The maximally mixed state  $\rho = \mathbb{1}_2/2$  would be located at the center of the Bloch sphere with  $\mathbf{r} = 0$ . In Fig. 2.2 the state vector  $|\psi\rangle$  is shown together with its polar  $(\cos\varphi\sin\theta,\sin\varphi\sin\theta,\cos\theta)$  as well as Cartesian  $\mathbf{r}$  coordinates.

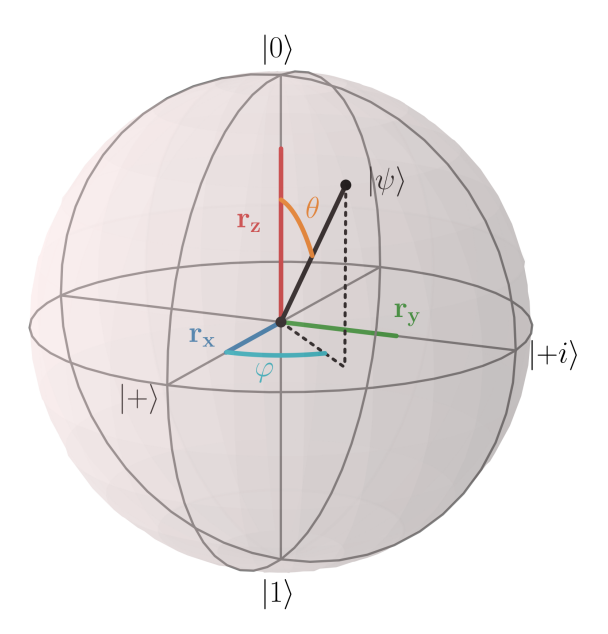


**Figure 2.2.:** Bloch sphere representation of the state of a single qubit for pure and mixed states. Points on the surface of the Bloch sphere correspond to pure states, whereas points inside correspond to mixed states. The maximally mixed state is located in the center of the sphere.

Similar to how the Schrödinger equation 2.6 governs the time evolution for state vectors, the time evolution for the density matrix formalism is described by the von Neumann equation

$$\frac{\mathrm{d}\rho}{\mathrm{d}t} = -\frac{i}{\hbar} \left[ \hat{\mathcal{H}}(t), \rho \right] \tag{2.10}$$

where  $[\cdot,\,\cdot]$  is the commutator following the relation  $\left[\hat{a},\hat{b}\right]=\hat{a}\hat{b}-\hat{b}\hat{a}$  with  $\hat{a},\,\hat{b}$  being operators.

Depending on the situation we can identify either the Schrödinger equation 2.6 or the von Neumann equation 2.10 as the first-order differential equation underlying the optimal control problem in Eq. 2.1. What is left is to find an expression for the Hamiltonian  $\hat{\mathcal{H}}$  modelling the system of interest and to identify free parameters of the system that can be controlled by a suitable controller in order to induce the desired changes in the quantum state.

#### 2.2.2. Light-matter interaction

After having introduced the general notation for quantum information processing in the previous section, this section will focus on the mathematical treatment of how to manipulate quantum mechanical two-level systems confined in a harmonic potential. Control over the system is achieved by changing the available parameters of an applied electric field. The aim of this section is to derive the Hamiltonian function governing this light-matter interaction and to identify suitable and experimentally accessible parameters of the electric field to achieve the desired state manipulation.

The system we want to model can be described by a total system Hamiltonian  $\hat{\mathcal{H}}_{sys}$  consisting of a time-independent part  $\hat{\mathcal{H}}_{0}$  and a time-dependent part  $\hat{\mathcal{H}}_{lm}$  that models the light-matter interaction, as follows:

$$\hat{\mathcal{H}}_{\text{sys}} = \underbrace{\hat{\mathcal{H}}_{\text{el}} + \hat{\mathcal{H}}_{\text{mot}}}_{\hat{\mathcal{H}}_{0}} + \hat{\mathcal{H}}_{\text{lm}}(t). \tag{2.11}$$

#### 2. Theoretical framework

The first term  $\hat{\mathcal{H}}_{\mathrm{el}}$  models a quantum mechanical two-level system with a ground state  $|g\rangle$  and an excited state  $|e\rangle$ , separated by an energy difference of  $\hbar\omega_{\mathrm{eg}}$ . This system can be regarded as a qubit, allowing the computational basis states  $|0\rangle := |g\rangle$  and  $|1\rangle := |e\rangle$  to be encoded into those two energy levels. When considering N identical two-level systems indexed by  $j=1,\,2,\ldots,\,N$ ; the energy levels of system j are are eigenstates of the  $\hat{\sigma}_{z,j} = |1\rangle_j \, \langle 1|_j - |0\rangle_j \, \langle 0|_j$  operator, which is acting solely on system j. Thus it is natural to express the Hamiltonian as

$$\hat{\mathcal{H}}_{el} = \sum_{j=1}^{N} \frac{\hbar \omega_{eg}}{2} \hat{\sigma}_{z,j}.$$
 (2.12)

The second term  $\hat{\mathcal{H}}_{mot}$  concerns the trapping potential, which in first order can be approximated as a quadratic potential in three dimensions and modelled as three separate, one-dimensional harmonic oscillators. When trapping N two-level systems in this potential, there exist in each direction N motional eigenfrequencies  $\omega_k$  of the coupled system, which for three dimensions yields for the mode index k the values k = 1, 2, ..., 3N. These eigenfrequencies  $\omega_k$  can be numerically calculated following Ref. 14 and the Hamiltonian then takes on the form

$$\hat{\mathcal{H}}_{\text{mot}} = \sum_{k=1}^{3N} \hbar \omega_k \left( \hat{a}_k^{\dagger} \hat{a}_k + \frac{1}{2} \right) = \sum_{k=1}^{3N} \hbar \omega_k \left( \hat{n}_k + \frac{1}{2} \right). \tag{2.13}$$

Here,  $\hat{a}_k^{\dagger}(\hat{a}_k)$  is the motional creation (annihilation) operator and  $\hat{n}_k = \hat{a}_k^{\dagger}\hat{a}_k$  is the number operator of mode k that has the number of phonons in the harmonic oscillator of mode k as its eigenvalue. The joint system, consisting of N two-level systems confined in a harmonic potential, is assumed to be static and this time-independent part of the system Hamiltonian  $\hat{\mathcal{H}}_{\text{sys}}$  is denoted as  $\hat{\mathcal{H}}_0$ .

The third term  $\hat{\mathcal{H}}_{lm}(t)$  models the interaction of an electric field with the joint system  $\hat{\mathcal{H}}_0$  and can be regarded as a perturbation to an otherwise known system. As such it is more convenient to describe the time evolution in the interaction picture, where the state in the interaction picture  $|\psi_I(t)\rangle$  takes on the form  $|\psi_I(t)\rangle = \hat{U}_0(t)|\psi(t=0)\rangle$  with  $\hat{U}_0(t) = \exp(-i\hat{\mathcal{H}}_0 t/\hbar)$ . The time evolution can then be obtained with the equation

$$i\hbar \frac{\mathrm{d}}{\mathrm{d}t} |\psi_I(t)\rangle = \hat{\mathcal{H}}_{\mathrm{int}}(t)|\psi_I(t)\rangle = \hat{U}_0^{\dagger}(t)\hat{\mathcal{H}}_{\mathrm{lm}}(t)\hat{U}_0(t)|\psi_I(t)\rangle$$
 (2.14)

where  $\hat{\mathcal{H}}_{int}(t)$  is the Hamiltonian in the interaction representation. In the case of a vanishing electric field ( $\hat{\mathcal{H}}_{lm} = 0$ ), there is no time evolution of the state in the interaction picture and in the presence of an electric field, the time evolution is driven by the light-matter interaction part of the Hamiltonian  $\hat{\mathcal{H}}_{lm}$ .

We will now examine two different cases. In the first case described in Sec. 2.2.2, the coupling of a monochromatic light field to a single qubit leads to a manipulation of the internal quantum state and hence realizes a single qubit gate. In the second case described in Sec. 2.2.2, a bichromatic light field simultaneously illuminates two qubits and entanglement is created by means of the Mølmer Sørensen interaction. Note that in this chapter qubits are treated as an abstract concept for quantum mechanical two-level systems and one possible physical realization of qubits is outlined in Sec. 2.3.

#### Monochromatic light field

In this section the Hamiltonian governing the manipulation of the quantum state of a single qubit trapped in a harmonic potential is derived. Given that the two-level system is confined in a harmonic potential, the relative orientation  $\mathbf{k}\mathbf{x}$  between the position  $\mathbf{x}$  of the two-level system with respect to the wave vector  $\mathbf{k}$  of the incident light field has to be considered. We model the monochromatic light field here as a plane wave and it is given as a function of position  $\mathbf{x}$  and time t by

$$\mathbf{E}(\mathbf{x},t) = \mathbf{E}_0 \cos(\omega_L t + \mathbf{k}\mathbf{x} + \varphi_L), \tag{2.15}$$

where the electric field is described by its frequency  $\omega_L$ , phase  $\varphi_L$ , wave vector **k** as well as the field amplitude  $\mathbf{E}_0$ . The light-matter Hamiltonian then takes on the form

$$\hat{\mathcal{H}}_{lm} = \hbar\Omega \cos(\omega_L t + \mathbf{k}\mathbf{x} + \varphi_L)\hat{\sigma}_x \tag{2.16}$$

with the Rabi frequency  $\Omega$  being proportional to the electric field strength  $E_0$  and accounting for the coupling strength between the two energy states due to the light-matter interaction [15]. Changing into the interaction picture with respect to  $\hat{\mathcal{H}}_0$  results in

$$\hat{\mathcal{H}}_{\rm int} = \hbar \Omega e^{i(\hat{\mathcal{H}}_{\rm el} + \hat{\mathcal{H}}_{\rm mot})t/\hbar} \cos \left( \omega_L t + \sum_k \eta_k (\hat{a}_k + \hat{a}_k^{\dagger}) + \varphi_L \right) e^{-i(\hat{\mathcal{H}}_{\rm el} + \hat{\mathcal{H}}_{\rm mot})t/\hbar}, \tag{2.17}$$

where the term  $\mathbf{k}\mathbf{x}$  was rewritten using the Lamb-Dicke (LD) parameter  $\eta_k$  and the index of the motional mode k to  $\mathbf{k}\mathbf{x} = \sum_k \eta_k (\hat{a}_k + \hat{a}_k^{\dagger})$ . Here,  $\eta_k$  relates the size  $x_0$  of the ground state of the harmonic oscillator to the wavelength of the laser light  $|\mathbf{k}| = 2\pi/\lambda$  with the relation

$$\eta_k = \mathbf{k} \mathbf{e}_r x_0 \cos \theta_r = \frac{2\pi}{\lambda} \sqrt{\frac{\hbar}{2m\omega_k}} \cos \theta_r,$$
(2.18)

where  $\mathbf{e}_r$  is the unit vector in direction  $r \in \{x, y, z\}$  corresponding to the direction of the motional mode k. The angle between this axis r and the  $\mathbf{k}$ -vector of the laser beam is denoted as  $\theta_r$  and the mass of the two-level system confined in the trapping potential as m. The further simplification of Eq. 2.17 involves a rotating wave approximation, where sum frequency terms of the form  $\omega_L + \omega_{\rm eg}$  are dropped as they average out over the considered timescale, resulting in

$$\hat{\mathcal{H}}_{\text{int}} = \frac{\hbar\Omega}{2} \left\{ e^{-i(\Delta t - \varphi_L)} \hat{\sigma}_+ \exp\left[i\sum_k \eta_k \left(\hat{a}_k e^{i\omega_k t} + \hat{a}_k^{\dagger} e^{i\omega_k t}\right)\right] + \text{h.c.} \right\}, \tag{2.19}$$

where the electronic raising and lowering operators  $\hat{\sigma}_{\pm} = (\hat{\sigma}_x \pm i\hat{\sigma}_y)/2$  have been introduced and the cosine term was rewritten using  $\cos(x) = (e^{ix} + e^{-ix})/2$ . The detuning of the laser frequency  $\omega_L$  from the bare transition frequency  $\omega_{\rm eg}$  is defined as  $\Delta = \omega_L - \omega_{\rm eg}$  and h.c. is short for the hermitian conjugate. There are only 3 motional modes to consider here (one in each direction) because only a single two-level system is considered. For simplicity only the highest frequency motional mode  $\omega_{\rm tr}$  and hence one LD parameter  $\eta_{k={\rm tr}}$  is considered in the following calculations. A detailed derivation of Eq. 2.19 can be found in Ref. 16.

An important regime to consider is the LD regime, where the extent of the ground state wave function is much smaller then the wavelength of the incident electric field. In this regime the condition  $\eta_k^2(2\bar{n}_k+1) \ll 1$  holds for all motional modes k, with  $\bar{n}_k$  the mean phonon number of mode k. This necessitates cooling of the system to achieve a low phonon number  $\bar{n}$  in conjunction

with the LD parameter satisfying  $\eta \ll 1$ , called the LD limit. In the LD regime the exponential function in Eq. 2.19 is expanded up to first order yielding for the interaction Hamiltonian

$$\exp\left[i\eta\left(\hat{a}e^{-i\omega_{\rm tr}t} + \hat{a}^{\dagger}e^{i\omega_{\rm tr}t}\right)\right] = \mathbb{1} + i\eta(\hat{a}e^{-i\omega_{\rm tr}t} + \hat{a}^{\dagger}e^{i\omega_{\rm tr}t}) + \mathcal{O}(\eta^2) \tag{2.20}$$

$$\Rightarrow \hat{\mathcal{H}}_{\rm int} \approx \frac{\hbar\Omega}{2} \left\{ e^{-i(\Delta t - \varphi_L)} \hat{\sigma}_+ \left[ \mathbb{1} + i\eta \left( \hat{a} e^{-i\omega_{\rm tr}t} + \hat{a}^\dagger e^{i\omega_{\rm tr}t} \right) \right] + \text{h.c.} \right\}, \tag{2.21}$$

with higher order terms indicated by  $\mathcal{O}(\eta^2)$ . There are now two different regimes of interest based on the relationship between the trapping frequency  $\omega_{\rm tr}$  and the Rabi frequency  $\Omega$ .

In the unresolved sideband regime with  $\omega_{\rm tr} \ll \Gamma(\Omega)$ , the spacing of the sidebands is much smaller than the absorption width of the transition, hence the sidebands cannot be individually addressed by an electric field. The focus in this section is on the resolved sideband regime with  $\omega_{\rm tr} \gg \Gamma(\Omega)$ , where the motional sidebands are resolved and can be individually addressed. An additional rotating wave approximation can then be applied to Eq. 2.21, where terms oscillating with the trapping frequency  $\omega_{\rm tr}$  can be dropped as they average out over the course of the induced dynamics. From this three distinct cases can be identified, depending on the choice of the detuning  $\Delta$ .

#### 1. Carrier transition ( $\Delta = 0$ ):

When the frequency of the electric field is resonant with the transition frequency  $\omega_{\rm eg}$ , a carrier transition  $|0,n\rangle\leftrightarrow|1,n\rangle$  is driven, where the phonon number stays constant as the raising and lowering operators  $\hat{a}^{\dagger}$  and  $\hat{a}$  drop out. The resulting Hamiltonian for the carrier transition takes on the form

$$\hat{\mathcal{H}}_{CAR} = \frac{\hbar \Omega_{n,n}}{2} \left( \hat{\sigma}_{+} e^{i\varphi_{L}} + \hat{\sigma}_{-} e^{-i\varphi_{L}} \right), \tag{2.22}$$

with the modified Rabi frequency  $\Omega_{n,n} \approx \Omega(1-\eta^2 n)$ , where higher order terms in the expansion of the exponential function in Eq. 2.20 were taken into account. The choice of  $\Delta = 0$  enables the implementation of resonant, single qubit operations as the time evolution assumes the form

$$\hat{R}(\theta, \varphi_L) = e^{-i\hat{\mathcal{H}}_{CAR}t/\hbar} = \begin{pmatrix} \cos(\frac{\theta}{2}) & -ie^{-i\varphi_L}\sin(\frac{\theta}{2}) \\ -ie^{i\varphi_L}\sin(\frac{\theta}{2}) & \cos(\frac{\theta}{2}) \end{pmatrix}$$
(2.23)

$$= \exp\left(-i\frac{\theta}{2}(\hat{\sigma}_x \cos\varphi_L + \hat{\sigma}_y \sin\varphi_L)\right). \tag{2.24}$$

Visualized on the Bloch sphere, this single qubit operation rotates the state it acts upon and the rotation is characterized by the two variables  $\varphi_L$  and  $\theta$ . Specifically, the rotation axis lies in the equatorial plane of the Bloch sphere spanned by the x and y axis and is set by the phase of the electric field  $\varphi_L$ . Meanwhile, the rotation angle  $\theta = (1 - \eta^2 n) \int_0^t \Omega(t') dt'$  for a time-dependent Rabi frequency corresponds to the pulse area of the applied electric field. The expression simplifies to  $\theta = \Omega_{n,n} \cdot t$  when assuming a time-independent Rabi frequency  $\Omega$  over time t.

#### 2. Sideband transitions ( $\Delta = \pm \omega_{\rm tr}$ ):

Compared to the carrier transition where the phonon number stays constant  $\Delta n = 0$ , in sideband transitions the phonon number is changed by  $\Delta n = \pm 1$  depending on the driven sideband transition. Note that transitions with higher order changes in the phonon number  $|\Delta n| > 1$  are strongly suppressed in the LD regime by a factor of  $\eta^{|\Delta n|}$  and thus are not considered further. The blue sideband (BSB) transition is driven when the frequency of the electric field  $\omega_L$  is positively detuned by the trap frequency  $\omega_{\rm tr}$ , so  $\omega_L = \omega_{\rm eg} + \omega_{\rm tr}$ , leading to transitions of the form  $|0, n\rangle \leftrightarrow |1, n+1\rangle$ . For the red sideband (RSB) transition however a negative detuning is used, so  $\omega_L = \omega_{\rm eg} - \omega_{\rm tr}$ , with transitions  $|0, n\rangle \leftrightarrow |1, n-1\rangle$  if n > 0. Note that for n = 0, the system is already in the motional ground state and hence no red sideband transition to a lower energy state can be driven. The resulting Hamiltonians then take on the form

$$\hat{\mathcal{H}}_{\text{BSB}} = i\eta \hbar \frac{\Omega_{n,n+1}}{2} \left( \hat{\sigma}_{+} \hat{a}^{\dagger} e^{i\varphi_{L}} - \hat{\sigma}_{-} \hat{a} e^{-i\varphi_{L}} \right)$$
(2.25)

$$\hat{\mathcal{H}}_{RSB} = i\eta \hbar \frac{\Omega_{n,n-1}}{2} \left( \hat{\sigma}_{+} \hat{a} e^{i\varphi_{L}} - \hat{\sigma}_{-} \hat{a}^{\dagger} e^{-i\varphi_{L}} \right)$$
(2.26)

with the Rabi frequency  $\Omega_{n,n+1} = \eta \sqrt{n+1}\Omega$  for the BSB and  $\Omega_{n,n-1} = \eta \sqrt{n}\Omega$  for the RSB. Starting in the state  $|0,n\rangle$  with n > 0, Rabi oscillations can be driven to the state  $|1,n'=n\rangle$  (CAR),  $|1,n'=n+1\rangle$  (BSB) or  $|1,n'=n-1\rangle$  (RSB) and the state after time t takes on the form

$$|\psi(t)\rangle = R(\theta, \varphi_L)|0, n\rangle = \cos\frac{\theta}{2}|0, n\rangle + e^{i\varphi_L}\sin\frac{\theta}{2}|1, n'\rangle,$$
 (2.27)

with the pulse area  $\theta = \Omega_{n,n'} \cdot t$  depending on the driven transition. The coupling strengths  $\Omega_{n,n'}$  for these three transitions are summarized in Fig. 2.3a, with examples of resonant operations illustrated in Fig. 2.3b through their state trajectory on the Bloch sphere. Furthermore, the excited state population  $p_1(t)$  from Eq. 2.27 is shown in blue  $(\Delta = 0)$  in Fig. 2.4. The time it takes to transfer 100% of the population to the excited state  $|1,n'\rangle$  is referred to as " $\pi$ -time" in this thesis because the rotation angle is equal to  $\theta = \pi$ . It is an important reference time for the calibration and execution of quantum gates.

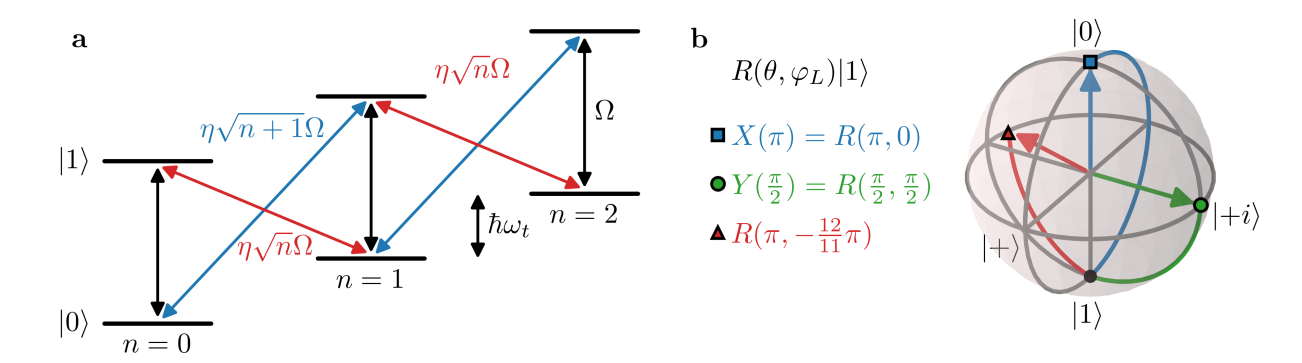


Figure 2.3.: a, A two-level system coupled with a harmonic oscillator exhibits carrier transitions (black) as well as blue and red sideband transitions, with their respective coupling strengths indicated for operation within the LD regime. b, Three examples of resonant operations with initial state  $|1\rangle$  and  $\Delta=0$ , implementing either a  $\pi$ -pulse with varying phase (square and triangle indicate the final state) or a  $\pi/2$ -pulse (circle). Resonant operations can be driven on the carrier, blue, or red sideband if operating in the LD regime.

## 3. Off-resonant transitions ( $|\Delta| \gg 0$ and $|\Delta \pm \omega_{\rm tr}| \gg 0$ ):

The electric field can not only be resonant ( $\Delta = 0$ ) with respect to the carrier and the two sideband transitions, but it can also be detuned from those transitions and hence be off-resonant. The excitation probability for both the resonant and off-resonant case is given by

$$p_1(t) = \left(\frac{\Omega}{\Omega_{\text{eff}}}\right)^2 \sin^2\left(\frac{\Omega_{\text{eff}} \cdot t}{2}\right),$$
 (2.28)

with the effective Rabi frequency  $\Omega_{\rm eff} = \sqrt{\Omega^2 + \Delta^2}$  [17]. For resonant transitions with  $\Delta = 0$ , the effective Rabi frequency becomes equal to the Rabi frequency  $\Omega_{\rm eff} = \Omega$  and the excitation

probability reduces to  $p_1 = \sin^2(\theta/2)$ , consistent with Eq. 2.27. Note that for larger values of the detuning  $\Delta$ , the amplitude of the excited state probability decreases in tandem with an increase of the frequency, as shown in Fig. 2.4.

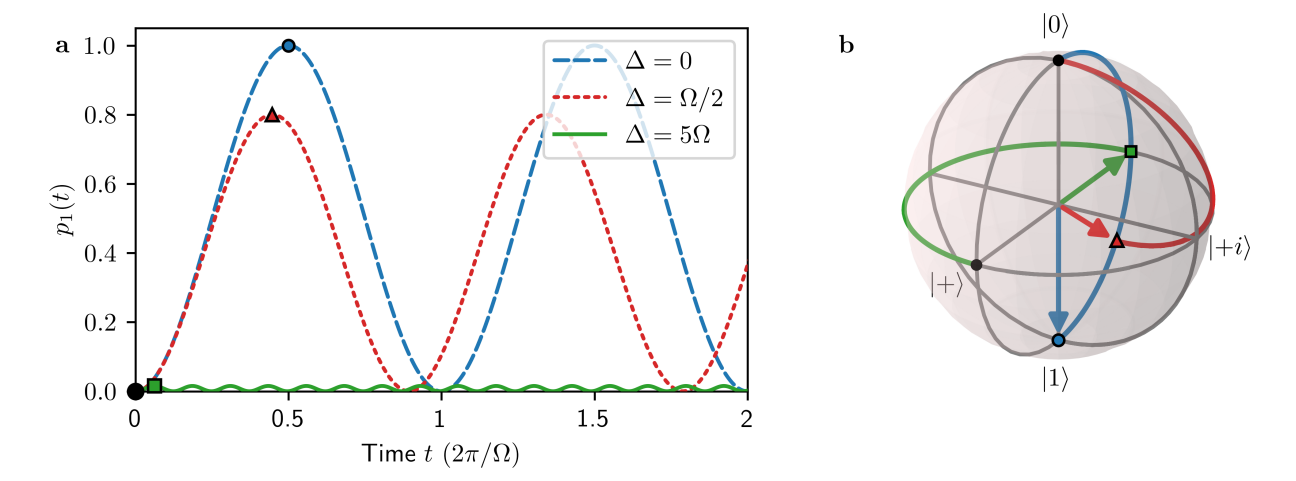


Figure 2.4.: a, Rabi oscillations for different choices of detuning  $\Delta$ , where the excited state population  $p_1(t)$  is plotted for an arbitrary Rabi frequency  $\Omega$ . Larger values of the detuning lead to an increase in the effective Rabi frequency and a decrease in the amplitude of the oscillations. b, Bloch sphere picture showing how the choice of the detuning  $\Delta$  affects the Bloch sphere trajectory, with black points showing the initial state and coloured shapes the respective final state. For large values of the detuning  $\Delta$ , no population is exchanged but an overall phase is accumulated which realizes a phase gate.

In the case of a far off-resonant transition from the carrier  $|\Delta| \gg 0$  or the two sideband transitions  $|\Delta \pm \omega_{\rm tr}| \gg 0$ , there is no population transfer from the ground to the excited state. In addition, the AC-Stark effect causes a shift in the transition frequency  $\Delta_{\rm AC}$  compared to the case of a vanishing electric field with  $\Omega = 0$ , which can be expressed as

$$\Delta_{\rm AC} = -\frac{\Omega^2}{2\Delta}.\tag{2.29}$$

Following the approach outlined in Ref. 18 and Ref. 19, an effective Hamiltonian for the case of a large detuning  $\Delta$  can be derived, yielding the expression

$$\hat{\mathcal{H}}_{\text{eff}} = \frac{1}{\hbar\Delta} \left[ \hat{\sigma}_{-}, \hat{\sigma}_{+} \right] = \frac{\hbar\Delta_{\text{AC}}}{4} \hat{\sigma}_{z}, \tag{2.30}$$

where only the time average over a period  $T \gg 2\pi/\Delta$  has been considered. From this it becomes apparent that this operation induces a phase shift between the states  $|0\rangle$  and  $|1\rangle$  and acts as a phase gate. In the experiment, rather than physically changing the phase by applying an off-resonant laser pulse, virtual phase gates are employed that work by changing the applied phase to all subsequent pulses on the software level [20]. An undesired phase shift from off-resonant transitions can nevertheless occur in the experiment and methods for compensating this shift are discussed in Sec. 2.3.3.

<sup>&</sup>lt;sup>1</sup>When operating in the LD regime within the two-level atom approximation, these three are the only relevant transitions that need to be considered. In a physical atom more levels need to be considered.

#### Bichromatic light field

The previous section introduced the Hamiltonian function describing the interaction of a single two-level system or qubit with a monochromatic electric field, which led to the possibility of resonant single-qubit gates by adjusting the pulse area  $\theta$  as well as the axis of rotation by changing the phase  $\varphi_L$  of the electric field. In this section, a bichromatic light field is used to address a pair of qubits and subsequently create entanglement between them. The following section introduces this Mølmer Sørensen (MS) gate [21] and describes, which parameters of the light field can be changed.

More specifically, multiple qubits  $(N \geq 2)$  are confined in a single trapping potential and an electric field simultaneously illuminates two out of the N qubits, denoted here with indices  $j_1$  and  $j_2$ . The Hamiltonian describing this system takes on the form

$$\hat{\mathcal{H}}_{\text{svs}} = \hat{\mathcal{H}}_0 + \hat{\mathcal{H}}_{\text{int}}^{j_1} + \hat{\mathcal{H}}_{\text{int}}^{j_2} \tag{2.31}$$

where the time-independent part  $\hat{\mathcal{H}}_0$  is the same as in Eq. 2.12 and Eq. 2.13, accounting for N qubits with M=3N motional modes. The time-dependent part consists of two terms  $\hat{\mathcal{H}}_{\mathrm{int}}^{\nu}$ , with each term modelling the interaction of the laser beam with a single qubit indexed by  $\nu \in \{j_1, j_2\}$ . Instead of applying a single frequency tone, here the electric field is bichromatic with the frequencies  $\omega_{\mathrm{eg}} \pm (\omega_{\mathrm{tr}} + \delta)$ , where the plus sign indicates the blue detuned frequency component  $\omega_{\mathrm{b}}$  and the minus sign the red detuned frequency component  $\omega_{\mathrm{r}}$ . Both frequency tones are detuned by  $\delta$  from the highest motional frequency  $\omega_{\mathrm{tr}}$  and similar to the previous section only this mode is considered. For simplicity, the entire detuning from the transition frequency or carrier frequency  $\omega_{\mathrm{eg}}$  is denoted as  $\delta_c = \omega_{\mathrm{tr}} + \delta$ . The bichromatic field is then a sum of the two contributions

$$\mathbf{E}_{b/r}(x,t) = \mathbf{E}_0 \cos \left[ \left( \omega_{\text{eg}} \pm \left( \omega_{\text{tr}} + \delta \right) \right) t + \mathbf{k} \mathbf{x} + \varphi_{b/r} \right]. \tag{2.32}$$

where the phase for the blue (red) detuned frequency is denoted as  $\varphi_b(\varphi_r)$  and the electric field amplitude  $\mathbf{E}_0$  is assumed to be the same for both frequency components. The resulting electric field can then be written as

$$\mathbf{E}(t) = \mathbf{E}_b(t) + \mathbf{E}_r(t) = 2\mathbf{E}_0 \cos\left[\omega_{\text{eg}}t + \mathbf{k}\mathbf{x} + \varphi_s\right] \cdot \cos\left[(\omega_{\text{tr}} + \delta)t + \varphi_m\right]$$
(2.33)

which corresponds to an amplitude modulated wave with carrier  $\omega_{\rm eg}$  and modulation frequency  $\omega_{\rm tr} + \delta$  [22] and is shown in Fig. 2.5a. Here two phases have been introduced called the spin-phase  $\varphi_s$  and the motional phase  $\varphi_m$  with their respective definitions

$$\varphi_s = \frac{\varphi_b + \varphi_r}{2} \quad \text{and} \quad \varphi_m = \frac{\varphi_b - \varphi_r}{2}.$$
(2.34)

Similarly to the derivation of the monochromatic Hamiltonian, the starting point for the bichromatic Hamiltonian is the interaction Hamiltonian in Eq. 2.21, assuming the system is in the LD regime. Accounting for an additional electric field and using the definitions of the spin and motional phase results in the transformation

$$e^{-i(\Delta t - \varphi_L)} \to e^{-i(\delta_c t - \varphi_b)} + e^{i(\delta_c t + \varphi_r)} \to e^{i\varphi_s} \left( e^{-i(\delta_c t - \varphi_m)} + e^{i(\delta_c t - \varphi_m)} \right)$$
 (2.35)

that can be applied to Eq. 2.21. Assuming equal electric field amplitudes at both ions and hence equal Rabi frequencies  $\Omega_{j_1} = \Omega_{j_2} = \Omega$  as well as equal LD parameters yields

$$\hat{\mathcal{H}}_{\rm int}^{\nu} \approx \frac{\hbar\Omega}{2} \left\{ e^{i\varphi_s} \left( e^{-i(\delta_c t - \varphi_m)} + e^{i(\delta_c t - \varphi_m)} \right) \sigma_+ \left[ 1 + i\eta \left( \hat{a}e^{-i\omega_{\rm tr}t} + \hat{a}^{\dagger}e^{i\omega_{\rm tr}t} \right) \right] + \text{h.c.} \right\}$$
(2.36)

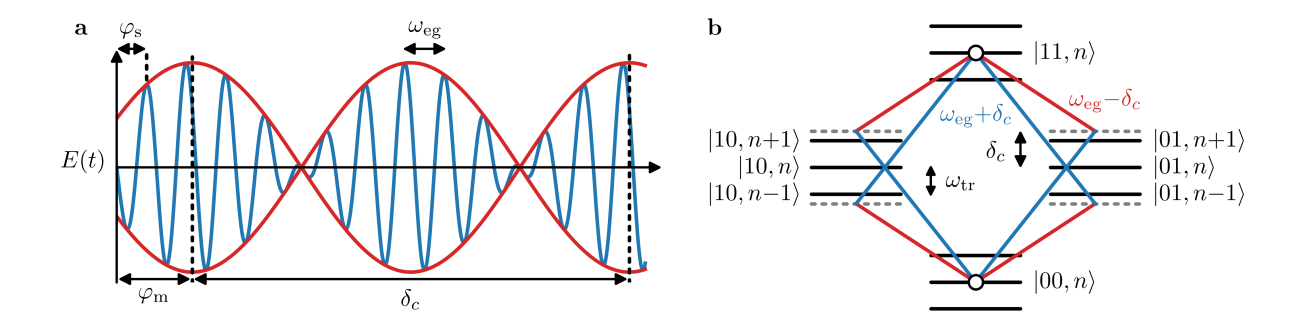


Figure 2.5.: a, Time evolution of the bichromatic electric field, consisting of the frequency tones  $\omega_{\rm eg} \pm \delta_c$ , that is used for the MS gate, with respective parameters shown. b, Relevant energy levels of the joint system consisting of two qubits trapped in a harmonic potential. The transition paths induced by the bichromatic field used in the MS gate couple the ground with the excited state via intermediate states. For an ideal MS gate, destructive interference of intermediate-state amplitudes leaves no remaining population in these states after the gate time  $\tau$ .

for the qubit with index  $\nu$ . Summing up the contributions of both qubits  $\hat{\mathcal{H}}_{\mathrm{int}}^{j_1}$  and  $\hat{\mathcal{H}}_{\mathrm{int}}^{j_2}$  and using the relation  $\cos(x) = (e^{ix} + e^{-ix})/2$  yields for the time-dependent part of the Hamiltonian

$$\hat{\mathcal{H}}_{\text{int}} = 2\hbar\Omega\cos\left(\delta_c t - \varphi_m\right)\hat{S}_{-\varphi_s} \tag{2.37}$$

$$- \hbar \eta \Omega \hat{S}_{\frac{\pi}{2} - \varphi_s} \left( \hat{a}^{\dagger} e^{i[(\omega_{\text{tr}} - \delta_c)t + \varphi_m]} + \hat{a} e^{-i[(\omega_{\text{tr}} - \delta_c)t + \varphi_m]} \right)$$
 (2.38)

$$- \hbar \eta \Omega \hat{S}_{\frac{\pi}{2} - \varphi_s} \left( \hat{a}^{\dagger} e^{i[(\omega_{\text{tr}} + \delta_c)t - \varphi_m]} + \hat{a} e^{-i[(\omega_{\text{tr}} + \delta_c)t - \varphi_m]} \right), \tag{2.39}$$

where  $\hat{S}_{\varphi} = \sum_{\nu} \cos(\varphi) \hat{\sigma}_{x}^{\nu} + \sin(\varphi) \hat{\sigma}_{y}^{\nu}$  is a rotation in the x-y-plane acting simultaneously on qubits  $j_{1}$  and  $j_{2}$  [23]. The first term  $\propto \hat{S}_{-\varphi_{s}}$  describes off-resonant coupling to the carrier transitions without changing the phonon number, which is undesired for the entangling operation but can be reduced by choosing a Rabi frequency that is much smaller than the detuning from the carrier transition  $\Omega \ll \delta_{c}$ . This term coined "direct coupling" also vanishes in the case that the two conditions outlined in Eq. 2.50 are fulfilled, requiring precise control over the duration and intensity of the laser beam [24]. In the following derivation of the Hamiltonian, this off-resonant carrier coupling term will be omitted. Another rotating wave approximation can be carried out by dropping the two terms in the last line with frequencies  $\omega_{\rm tr} + \delta_{c} = 2\omega_{\rm tr} + \delta$ , when the laser detuning is placed sufficiently close to the motional mode frequency such that  $|\delta_{c} - \omega_{\rm tr}| \ll \delta_{c}$  holds [24]. For the choices  $\varphi_{s} = -\pi/2$  and  $\varphi_{m} = 0$ , corresponding to  $\varphi_{b} = \varphi_{r} = -\pi/2$ , the Hamiltonian describing the interaction of a bichromatic electric field with two qubits confined in a single trapping potential assumes the form

$$\hat{\mathcal{H}}_{BIC} = \hbar \eta \Omega \hat{S}_x \left( \hat{a} e^{-i\delta t} + \hat{a}^{\dagger} e^{i\delta t} \right), \tag{2.40}$$

with the substitution  $\hat{S}_x = -\hat{S}_\pi = (\hat{\sigma}_x^{j_1} + \hat{\sigma}_x^{j_2})$ . In the derivation we implicitly assumed the use of amplitude pulse shaping at the beginning and end of the pulse in the experiment. If a simple square pulse would be realized instead, than the interaction basis  $\hat{S}_x$  would be dependent on whether the gate operation starts at the minimum or maximum intensity of the amplitude modulated laser beam. This effect vanishes when amplitude pulse shaping is used [22, 25].

Having derived the relevant Hamiltonian for the Mølmer Sørensen gate interaction, the next step is to investigate the time evolution and how a bichromatic electric field can create spin-spin

interaction between a pair of qubits. The relevant energy levels for creating the spin-spin interaction are shown in Fig. 2.5b, where the states  $|00\rangle$  and  $|11\rangle$  are coupled via intermediate states accompanied by a change in phonon number. The Hamiltonian in Eq. 2.40 is time-dependent and for times  $t_1 > t_2$  the commutator relation  $[\hat{\mathcal{H}}_{BIC}(t_2), \hat{\mathcal{H}}_{BIC}(t_1)]$  is nonzero. The time evolution operator is then obtained with the Magnus expansion given by

$$\hat{U}(t) = \exp\left(-\frac{i}{\hbar} \int_0^t dt_1 \,\hat{\mathcal{H}}_{BIC}(t_1) - \frac{1}{2\hbar^2} \int_0^t dt_2 \, \int_0^{t_1} dt_1 \, \left[\hat{\mathcal{H}}_{BIC}(t_2), \hat{\mathcal{H}}_{BIC}(t_1)\right] + \ldots\right). \tag{2.41}$$

Considering only the first two terms of the expansion, since higher order terms of the Magnus expansion for  $\hat{\mathcal{H}}_{\mathrm{BIC}}$  vanish, leads to the propagator

$$\hat{U}(t) = \hat{D}\left(\alpha(t)\hat{S}_x\right)e^{i\Phi(t)\hat{S}_x^2},\tag{2.42}$$

where the displacement operator  $\hat{D}(\alpha(t)\hat{S}_x) = \exp[(\alpha(t)\hat{a}^{\dagger} - \alpha^*(t)\hat{a})\hat{S}_x]$  has been introduced. Note that both the phase space trajectory  $\alpha(t)$  and the entangling phase  $\Phi(t)$  will be introduced in the following paragraphs.

The aim in this thesis is to create maximally entangled states with high-fidelity, which is achieved for  $\alpha(\tau) = 0$  and  $\Phi(\tau) = \pm \pi/2$  at the end of the gate time  $t = \tau$ , resulting in the MS gate

$$MS(\Phi = \pi/2) |00\rangle = e^{i\frac{\pi}{2}\hat{S}_x^2} |00\rangle = \frac{1}{\sqrt{2}} (|00\rangle + i |11\rangle).$$
 (2.43)

Even though the Bloch sphere picture generalizes to arbitrary multi-qubit states, already its visualization for two qubits would have to be drawn in 4 dimensions. One helpful way to investigate the time evolution of the two-qubit state during the gate operation is in phase space. The horizontal axis of phase space corresponds to the real part of the phase-space trajectory  $\text{Re}(\alpha(t))$  and the vertical axis to the imaginary part  $\text{Im}(\alpha(t))$ . Note that the phase space is drawn in the interaction picture and thus in a rotating frame of reference with respect to the actual physical system. The state of the two-qubit system at the start of the entangling gate t=0 is assumed to be located at the center of phase space and it evolves along a phase space trajectory  $\alpha(t)$  that can be derived from the first order Magnus expansion and is equal to

$$\alpha(t) = i\eta \Omega \int_0^t e^{-i\delta t'} dt'$$
(2.44)

$$= \eta \frac{\Omega}{\delta} (1 - e^{-i\delta t}). \tag{2.45}$$

Given that  $|00\rangle = \frac{1}{2}(|++\rangle + |--\rangle + |+-\rangle + |-+\rangle)$ , it becomes apparent that the displacement  $\hat{D}(\alpha(t)\hat{S}_x)$  of the two-qubit state in phase space is state-dependent. Its amplitude is given by  $\eta\Omega/\delta(1-e^{-i\delta t})\hat{S}_x|\dots\rangle$ , with  $|\dots\rangle$  the state it acts on. As the LD factor for the COM mode has the same sign for every ion that couples to it, only the states  $|++\rangle$  and  $|--\rangle$  are displaced in phase space by the spin-dependent force exerted by the MS gate. The states  $|-+\rangle$  and  $|+-\rangle$  are not displaced in phase space, as  $\hat{S}_x|+-\rangle=\hat{S}_x|-+\rangle=0$ . This is indicated in Fig. 2.6b. Furthermore a displacement from the center of phase space  $\alpha\neq 0$  corresponds to entanglement between the internal degree of freedom of the two-level system (spin in the case of atoms) and the motional modes. At the end of the gate time  $t=\tau$  the aim is to achieve  $\alpha(\tau)=0$  in order to have no residual entanglement between qubit and motional modes. From Eq. 2.45 it follows that the condition  $\tau_{\tilde{m}}=2\pi\tilde{m}/|\delta|$  needs to be fulfilled for the gate time  $\tau_{\tilde{m}}$ , with  $\tilde{m}\in\mathbb{N}$ . For a

constant Rabi frequency  $\Omega$  during the gate time this corresponds to a closed circle in phase space which starts and ends at the origin.

Although the position in phase space returns back to the origin in the ideal case, the state has accumulated a phase during the evolution called geometric phase. This phase of the entangling gate  $\Phi$  can be derived from the second order term in the Magnus expansion in Eq. 2.42 and takes on the form

$$\Phi(t) = \frac{i}{2} \int_0^t \left( \frac{d\alpha(t')}{dt'} \alpha^*(t') - \alpha(t') \frac{d\alpha^*(t')}{dt'} \right) dt'$$
(2.46)

$$= \left(\eta \frac{\Omega}{\delta}\right)^2 \left[\delta t - \sin(\delta t)\right],\tag{2.47}$$

and corresponds to the enclosed area in phase space after time t. For the condition  $t = 2\pi \tilde{m}/|\delta|$ , when no residual spin-motion entanglement is present, it follows for the entangling phase that

$$\Phi(\tau_{\tilde{m}}) = \left(\eta \frac{\Omega}{\delta}\right)^2 2\pi \tilde{m} \operatorname{sign}(\delta). \tag{2.48}$$

The only free parameter than can be changed is the Rabi frequency, as the detuning and gate time  $\tau$  are in a fixed relation to guarantee a closed phase space trajectory. Maximally entangled states with  $\Phi = \pm \pi/2$  are achieved for the choice  $\Omega = |\delta|/(2\sqrt{\tilde{m}}\eta)$ , with the sign of the entangling phase depending on whether the detuning  $\delta$  is positive or negative with respect to  $\omega_{\rm tr}$ . Summarized, an ideal gate operation can be obtained by the following choice of parameters for a single mode:

$$t = \frac{2\pi\tilde{m}}{|\delta|} \Rightarrow \alpha(\tau) = 0 \tag{2.49}$$

$$\Omega = \frac{|\delta|}{2\sqrt{\tilde{m}\eta}} \Rightarrow \Phi(\tau) = \operatorname{sign}(\delta) \cdot \frac{\pi}{2}.$$
 (2.50)

An example of ideally chosen parameters is shown in Fig. 2.6a through the time evolution of the state population. Starting out in  $|00\rangle$ , the MS gate is realized for a gate time of  $\tau = 300\,\mu s$  resulting in the state  $(|00\rangle + i\,|11\rangle)/\sqrt{2}$ . At the same time the intermediate state population is minimal because the two paths coupling the states  $|00\rangle$  with  $|11\rangle$  via the intermediate states, where the phonon number is changed, interfere destructively for symmetric detuning around the carrier frequency  $\omega_{eg}$ . The transition paths are shown in Fig. 2.5b. If the MS gate is applied for a total time duration of  $t = 2\tau$ , the populations of the states  $|00\rangle$  and  $|11\rangle$  are swapped compared to t = 0, with the populations returning to their initial state for  $t = 4\tau$ .

In Fig. 2.6b, the phase space trajectory for this one considered mode with frequency  $\omega_{\rm tr}$  is shown. In particular, the effect of the MS gate on particular states is shown, with the states  $|++\rangle$  and  $|--\rangle$  traversing the phase space in a circular trajectory under the assumption of a constant Rabi frequency during the whole gate duration. The enclosed area of this phase space trajectory is then equal to the acquired entangling phase at the end of the gate at  $t = \tau$ .

Up until now only the highest frequency motional mode  $\omega_{\rm tr}$  has been considered. We will now extend the Hamiltonian as well as the time evolution to include multiple motional modes  $\omega_k$ . For the Hamiltonian, one obtains

$$\hat{\mathcal{H}}_{BIC} = \hbar\Omega \sum_{k} \hat{S}_{x,k} \left( \hat{a}_k e^{-i\delta_k t} + \hat{a}_k^{\dagger} e^{i\delta_k t} \right), \tag{2.51}$$

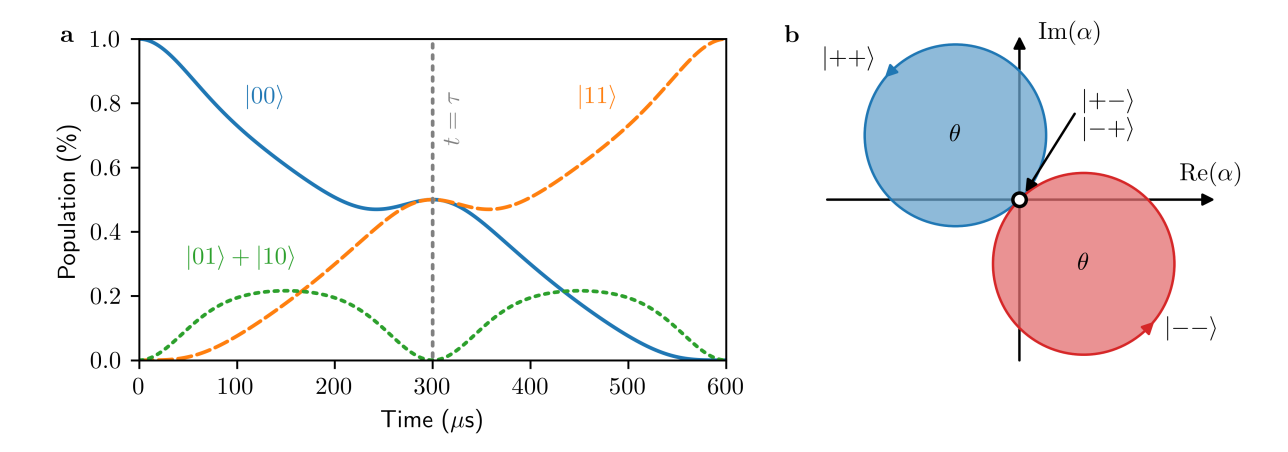


Figure 2.6.: a, Time evolution of the state populations for an MS gate with a gate time of  $\tau = 300 \,\mu\text{s}$ . b, Phase space trajectory  $\alpha$  showing the circular trajectory for a single mode. The phase space picture shows the off-resonantly driven harmonic oscillator in the interaction picture rotating with the laser frequency to be stationary. Note that the eigenstates of the  $\hat{S}_x$  operator only provide the state-dependent amplitude for the phase space picture and are not affected by the time evolution shown on the left.

with  $\delta_k = \delta_c - \omega_k$  being the detuning of the laser frequency from the motional mode  $\omega_k$ . The subscript k on the operators  $\hat{a}_k$  and  $\hat{a}_k^{\dagger}$  indicate that they only act on mode k and the LD parameters have been absorbed by the spin operator  $\hat{S}_{x,k} = (\eta_k^{j_1} \hat{\sigma}_x^{j_1} + \eta_x^{j_2} \hat{\sigma}_x^{j_2})$ . The propagator can be written as the product over motional modes

$$\hat{U}(t) = \prod_{k} \hat{U}_k(t) = \prod_{k} \hat{D}\left(\alpha_k(t)\hat{S}_{x,k}\right) e^{-i\mathcal{B}_k(t)\hat{S}_{x,k}^2}$$
(2.52)

with the phase space trajectory  $\alpha_k$  and the entangling phase  $\Phi(t)$  given by the expressions

$$\alpha_k(t) = i\Omega \int_0^t e^{-i\delta_k t'} dt'$$
(2.53)

$$\Phi(t) = \frac{i}{2} \sum_{k} \eta_k^{j_1} \eta_k^{j_2} \underbrace{\left[ \int_0^t \left( \frac{\mathrm{d}\alpha_k(t)}{\mathrm{d}t'} \alpha_k^*(t') - \alpha_k(t') \frac{\mathrm{d}\alpha_k^*(t')}{\mathrm{d}t'} \right) \, \mathrm{d}t' \right]}_{\mathcal{B}_k(t)}$$
(2.54)

Instead of having a single, circular<sup>2</sup> phase space trajectory describing the time evolution of one mode, now up to 3N trajectories corresponding to the number of considered modes needs to be taken into account. The conditions for creating a maximally entangled state are given by

$$\alpha_k(\tau) = 0 \quad \forall k \tag{2.55}$$

$$\Phi(\tau) = \pm \frac{\pi}{2} \tag{2.56}$$

where the first condition guarantees that no entanglement between spin and motion is present at the end of the gate, hence that there is no displacement error. The second condition pertains to the acquired entangling phase and it can either be positive or negative, depending on the desired operator. Similar to the single mode case, two parameters can be adjusted to achieve those conditions, namely the detuning  $\delta_c$  and the Rabi frequency  $\Omega$ .

<sup>&</sup>lt;sup>2</sup>The phase space trajectory assumes a circular trajectory for constant Rabi frequency  $\Omega$  and detuning  $\delta_k$  during the gate time.

#### 2.2.3. Physical constraints and performance measure

After having discussed how single- and two-qubit gates can be implemented using electric fields, we now turn to the question about which physical constraints exist and how one quantifies the quality of the gate.

Two main physical constraints are imposed by limitations in the choice of the Rabi frequency and the detuning. The maximum achievable Rabi frequency is limited by the maximum power that the source of the electric field can provide and this upper bound is experimentally determined. For a time-dependent Rabi frequency, there are additional physical constraints coming from the control electronics that can lead to discrepancies between simulation and experimental results. These constraints are discussed in more detail in Chap. 5. Furthermore the value of the detuning  $\delta_c$ , which in this thesis is always chosen to be constant during the gate time, is in principle only limited by the range of frequencies the RF generation hardware can provide. In practice however, it is sufficient to consider only the frequency range of the motional modes around the considered carrier transition.

The quality of the MS gate is assessed using the state preparation fidelity  $\mathcal{F}$ , which quantifies the ability of the gate to prepare the desired maximally entangled state  $|\phi\rangle$  by comparing it to the actually achieved state  $|\psi\rangle$ . For two pure states  $|\psi\rangle$  and  $|\phi\rangle$ , the state preparation fidelity is given by the overlap between those two states

$$\mathcal{F}(|\phi\rangle, |\psi\rangle) = |\langle\phi|\psi\rangle|^2 \tag{2.57}$$

with the bounds  $0 \le \mathcal{F} \le 1$ . It can be generalized to mixed states  $\rho$  and  $\sigma$  as follows:

$$\mathcal{F}(\rho,\sigma) = \left(\operatorname{tr}\sqrt{\sqrt{\rho}\sigma\sqrt{\rho}}\right)^{2}.$$
 (2.58)

For numerical simulations that compute and return the full density matrix of the system at each time step, referred to as Hamiltonian simulation in Sec. 4.1, this expression can be directly used to calculate the fidelity. If the numerical simulation does not explicitly calculate the density matrix of the system but rather uses the phase space picture to simulate the time evolution, called phase space simulation, a state preparation fidelity can be calculated following Ref. 26. Required for this are both the phase space trajectory  $\alpha_k(\tau)$  and the acquired entangling phase  $\Phi(\tau)$  at the end of the gate in conjunction with the experimentally measured mean phonon number  $\bar{n}_k$  of mode k. The average gate fidelity is then independent of the initial state and can be calculated using

$$\bar{\mathcal{F}} \approx \frac{1}{10} \left[ 4 + 2(\Gamma_{j_1} + \Gamma_{j_2}) \sin(2\Phi) + \Gamma_+ + \Gamma_- \right],$$
 (2.59)

where an equal amplitude of the electric field on both qubits was assumed. The individual terms are given by

$$\Gamma_{j_1(j_2)} = \exp\left[-2\sum_k \left| \eta_k^{j_1(j_2)} \alpha_k^{j_1(j_2)} \right|^2 \coth\left(\frac{\omega_k}{2\omega_{k,\text{max}}} \ln(1 + 1/\bar{n}_k)\right)\right],\tag{2.60}$$

$$\Gamma_{\pm} = \exp\left[-2\sum_{k} \left|\eta_{k}^{j_{1}} \alpha_{k}^{j_{1}} \pm \eta_{k}^{j_{2}} \alpha_{k}^{j_{2}}\right|^{2} \coth\left(\frac{\omega_{k}}{2\omega_{k,\text{max}}} \ln(1+1/\bar{n}_{k})\right)\right]$$
(2.61)

with  $\omega_{k,\text{max}}$  being the highest frequency mode in the direction of mode  $k^3$ .

<sup>&</sup>lt;sup>3</sup>This is only true when considering radial modes, for axial modes one would need to take the lowest frequency mode instead of the highest.

#### 2. Theoretical framework

The state preparation fidelity for experimental results  $\mathcal{F}$  is obtained with population scans and parity oscillations [27]. The density matrix of a system of N qubits, where 2 out of N qubits have been addressed with an MS gate, has in the ideal case only 4 nonzero entries that need to be measured. On the diagonal of the  $2^N \times 2^N$  density matrix are the populations of particular states and only the entries corresponding to  $|00\rangle$  as well as  $|11\rangle$  for the considered qubits should be nonzero for an ideal gate operation. These entries can be obtained by applying a single MS gate on the target qubits and measuring the population p of  $|00\rangle + |11\rangle$  after tracing out qubits that have not been addressed by the gate operation, thus the population can be inferred with  $P = p_{00} + p_{11}$ . The off-diagonal entries in a density matrix refer to the coherence between different states and in this particular case the coherence between the states  $|00\rangle$  and  $|11\rangle$  can be obtained with so called parity oscillations. Similar to before, a single MS gate is applied to the target qubits followed by a resonant single-qubit operation  $R(\theta = 0.5, \varphi_L = \varphi)$  applied to both qubits individually. This  $\pi/2$  pulse with varying phase  $\varphi$  corresponds to a local rotation and changes the parity of the entangled state given by  $\mathcal{P} = p_{00} + p_{11} - p_{10} - p_{01}$  periodically with the angle  $\varphi$ . Assuming one prepares the state  $|\psi\rangle = \text{MS}(-\pi/2)|00\rangle = (|00\rangle + i|11\rangle)/\sqrt{2}$ , for a phase of  $\varphi = 3\pi/4$  this state remains unaltered and corresponds to a parity of  $\mathcal{P} = +1$ . For  $\varphi = \pi/4$ the state  $|\Phi\rangle = (|01\rangle + |10\rangle)/\sqrt{2}$  is prepared with a parity of  $\mathcal{P} = -1$ . The amplitude of those parity oscillations  $\mathcal{P}(\varphi) = C \cdot \cos(N\varphi + \varphi_0)$ , with  $\varphi_0$  a phase offset, directly corresponds to the coherence C and hence to the sum of the off-diagonal elements of the density matrix relating the states  $|00\rangle$  and  $|11\rangle$ . The state preparation fidelity can then be calculated as the average of the population P and the coherence C as  $\mathcal{F} = (P+C)/2$ .

## 2.3. Ion trap quantum computing platform

The previous section outlined the necessary concepts for quantum information processing, without focusing on a specific physical implementation. In this section, the ion trap quantum computing platform is introduced as the platform that is used in this thesis, starting with the description of how ions are trapped using electric fields in Sec. 2.3.1. The focus then shifts to the  $^{40}\text{Ca}^+$  ion in Sec. 2.3.2, in particular to the electronic states in which the qubit is encoded and to the relevant control fields for the manipulation of the qubit states. The chapter concludes with an explanation of the AC-Stark shift and how to compensate it experimentally in Sec. 2.3.3.

#### 2.3.1. Linear Paul trap and motional modes

In the derivation of the Hamiltonian functions for the single and two-qubit gates in Sec. 2.2.2, it was assumed that the trapping potential is harmonic. This potential can be generated with a linear Paul trap that consists of two endcaps and a set of four blades as shown in Fig. 2.7.

The generation of a harmonic potential using only a static voltage  $U_{\rm DC}$  implies that the restoring force is linearly dependent on the distance from the center  $F_r = -U_{\rm DC}\alpha_r r$ , with positions in an orthogonal basis r = x, y, z and corresponding geometric factors  $\alpha_r$ . This force is produced by a parabolic potential  $F = -\nabla \Phi$  of the form

$$\Phi(x, y, z) = \frac{U_{\rm DC}}{2} (\alpha_x x^2 + \alpha_y y^2 + \alpha_z z^2).$$
 (2.62)

From this equation it becomes apparent that in order to fulfill the Laplace equation  $\nabla^2 \Phi = 0$ , at least one of the coefficients  $\alpha_r$  would need to be negative due to the condition  $\alpha_x + \alpha_y + \alpha_z = 0$ . Hence when using a time-independent trapping potential, an ion would only be confined in at most two spatial directions and anti-confined in the third direction, resulting in a loss of the ion from the trapping region. One possible way to avoid this problem is to use time-varying electric fields to confine the ions in the x-y-plane (radial direction) in addition to confining the ions in the z-direction (axial) by means of the static potential of Eq. 2.62. One approach to create the electric fields in the radial direction is to apply time-dependent radio frequency voltages to two out of the four blades that are opposite of each other, and supplying a constant voltage with a battery to the other two blades. The resulting dynamically created potential assumes the form

$$\Phi_{\rm rad}(x, y, z, t) = \frac{1}{2} (U_r + U_{\rm rf} \cos(\omega_{\rm rf} t)) (\beta_x x^2 + \beta_y y^2 + \beta_z z^2)$$
 (2.63)

where the applied radio frequency field is described by its frequency  $\omega_{\rm rf}$  and amplitude  $U_{\rm rf}$ . The geometric factors are denoted as  $\beta_r$  and  $U_r$  is a static offset voltage on two blades that generate the potential, again for  $r \in \{x, y, z\}$ . In the case of a linear Paul trap from Fig. 2.7, the geometric factors obey the relation

$$\alpha_x + \alpha_y = -\alpha_z < 0 \quad \text{and} \quad \beta_x = -\beta_y, \, \beta_z = 0.$$
 (2.64)

Note, that in order to achieve these geometric factors it is necessary to symmetrically position infinitely long hyperbolic blades in the z-direction around the point x = y = 0, which creates a harmonic potential in the whole trapping region enclosed by the hyperbolic blades. However in reality blades of finite dimensions are used, which create a harmonic trapping potential only in the vicinity of the trap center in the x-y direction. The geometric factors  $\alpha_r$  and  $\beta_r$  account for this deviation of the potential generated by the hyperbolic blades from the actually used ones.

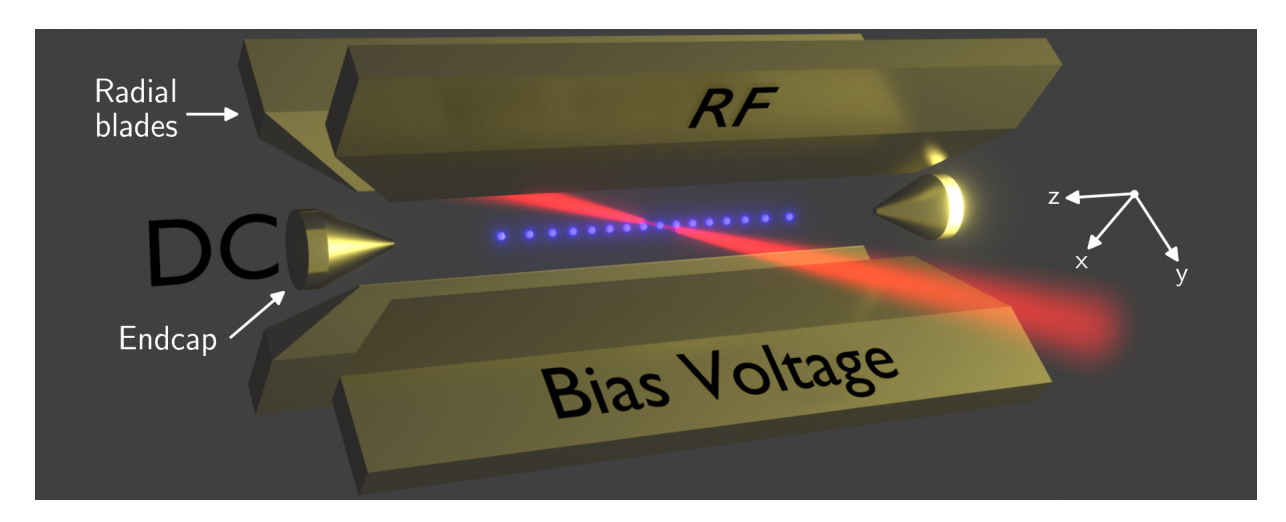


**Figure 2.7.:** Illustration of a linear Paul trap. Confinement of the ions (blue dots) in the axial or z-direction is ensured by two endcaps with an applied direct-current (DC) voltage. Confinement in the radial or x- and y-plane is achieved by applying a RF signal to two opposing radial blades, with the other two blades held at a DC bias voltage to lift the degeneracy of the radial modes. Radial addressing of the ions is depicted by the red Gaussian laser beam.

This potential confines a single ion with charge Q and mass m, which can be seen by deriving the equations of motion by solving Mathieu differential equations. We first introduce the stability parameters

$$a_x = a_y = -\frac{8QU_{\rm DC}}{mR_{\rm av}^2\omega_{\rm rf}^2} = -\frac{1}{2}a_z, \quad q_x = q_y = \frac{4QU_{\rm rf}}{mR_{\rm rad}^2\omega_{\rm rf}^2} = -\frac{1}{2}q_z$$
 (2.65)

where  $R_{\rm ax} = R_0^2 + z^2$  is the distance from the ion to the blade (tip). For stability parameters that obey the relation  $0 \le a_i \le q_i \le 1$  the trajectory of the ions can be approximated as

$$r_i(t) \approx r_i^0 \cos(\omega_i t + \phi_i) \cdot \left(1 + \frac{q_i}{2} \cos(\omega_{\rm rf} t)\right)$$
 (2.66)

and the motion can be split into two distinct parts. The first part is called *secular* motion and describes the trajectory of the ion with amplitude  $r_i^0$  and the secular frequencies  $\omega_i$  given by

$$\omega_x = \omega_y = \sqrt{\frac{(q_x \omega_{\rm rf})^2}{8} - \frac{\omega_z}{4}}$$
  $\omega_z = \sqrt{\frac{2\alpha_z U_{\rm DC} Q}{mR_{\rm ax}^2}}.$  (2.67)

Here, the degenerate secular frequencies in the radial direction  $\omega_x$  and  $\omega_y$  correspond to the highest frequency mode  $\omega_{\rm tr}$  and are called Center-Of-Mass (COM) modes, with the COM mode in the axial direction  $\omega_z$  corresponding to the lowest frequency mode. It's called COM mode because the ions' motion can be described solely by the motion of their center of mass, which for a single ion simply corresponds to the motion of the ion itself. Note that in experimental settings it is undesirable to have equal radial COM mode frequencies  $\omega_x = \omega_y$ , as this leads to problems in cooling. Instead of having two blades held at ground potential, a bias voltage is applied that lifts the degeneracy of the radial COM mode frequencies  $\omega_x$  and  $\omega_y$ . The second part of the motion in Eq. 2.66 is called *micromotion* and effectively modulates the secular harmonic motion with the frequency  $\omega_{\rm rf}$ . For more details the reader is referred to the references [15, 28, 29].

When trapping N ions in a single harmonic trapping potential, there are 2N radial mode frequencies and N axial mode frequencies to consider. For N=1 this corresponds again to the

radial COM mode frequencies  $\omega_x$  and  $\omega_y$  and the axial COM mode frequency  $\omega_z$ . For N>1 the ions form a coupled harmonic oscillator, with forces between ions mediated by the Coulomb force. If the ions are sufficiently cooled such that they form a crystal structure, distinct motional frequencies in addition to the COM mode frequencies arise. For the implementation of high-fidelity quantum gates, such as the MS gate outlined in Sec. 2.2.2, it is necessary to account for those frequencies as their presence modifies the gate dynamics.

The motional mode frequencies for a highly anisotropic potential with  $\omega_x \gg \omega_z$  and  $\omega_y \gg \omega_z$  (resulting in a linear string of ions) can be numerically calculated following Ref. 14, which is based on Ref. 30 and Ref. 31. First the equilibrium positions of the ions are calculated using the three COM mode frequencies and the mass m of the ions as input parameters. From these positions the motional mode frequencies can be obtained and with them also the LD factors following Eq. 2.18.

## **2.3.2.** $^{40}$ Ca<sup>+</sup> as a qubit

The previous section discussed linear Paul traps as a means to trap ions without focusing on a particular ion species. This section introduces the <sup>40</sup>Ca<sup>+</sup> ion as a possible choice for an ion species commonly found in ion trap quantum computers.

The calcium 40 atom has two valence electrons and it can be ionized via a two-stage photo-ionization process described in Ref. 32. First, laser light with 423 nm is used to excite specifically the <sup>40</sup>Ca isotope of calcium, which reduces the probability of unwanted excitation of background atoms. Then 375 nm laser light is used to excite the <sup>40</sup>Ca atom further to the continuum, ionizing the atom in the process.

The resulting  $^{40}\mathrm{Ca^+}$  ion has several desirable properties that make it a suitable candidate for quantum information processing. As an alkaline earth metal in group II of the periodic table, a positively charged  $^{40}\mathrm{Ca}$  atom has a single valence electron and possesses a hydrogen-like electronic level structure, with relevant levels for quantum computing shown in Fig. 2.8. These levels are the ground state  $4^2\mathrm{S}_{1/2}$ , the short-lived  $4^2\mathrm{P}_{3/2}$  and  $4^2\mathrm{P}_{1/2}$  states with lifetimes of  $\tau \sim 7\,\mathrm{ns}$  [33] and the metastable states  $3^2\mathrm{D}_{3/2}$  and  $3^2\mathrm{D}_{5/2}$ , with the latter having a lifetime of  $\tau \approx 1.168(7)\,\mathrm{s}$  before decaying to the ground state [34]. Here the notation  $q^{2s+1}l_j$  is used, where q is the principal quantum number, s the spin, l the angular momentum and j=l+s the total angular momentum quantum number.

Applying an external magnetic field lifts the degeneracy of the Zeeman states with quantum number  $m_j$ , where only the relevant levels are shown in Fig. 2.8. The qubit is then encoded in the two Zeeman sub-levels  $|0\rangle = |4^2 S_{1/2}, m_j = -1/2\rangle$  and  $|1\rangle = |3^2 D_{5/2}, m_j = -1/2\rangle$ , that are connected via an electric quadrupole transition at 729 nm. This transition is preferred among all possible transitions, as it is the least sensitive to magnetic field fluctuations.

After loading the ion(s) into the linear Paul trap, they need to be prepared to their motional ground state in order to be able to operate in the LD regime necessary for the quantum operations discussed in Sec. 2.2.2. As a first step Doppler cooling [35] is performed on the  $4^2\mathrm{S}_{1/2}\leftrightarrow 4^2\mathrm{P}_{1/2}$  transition using 397 nm laser light. Simultaneously a repumping laser with a wavelength of 866 nm is applied as population can also be trapped in the undesired  $3^2\mathrm{D}_{3/2}$  state. After Doppler cooling, sideband cooling is carried out with the 729 nm laser on the  $|4^2\mathrm{S}_{1/2},m_j=-1/2\rangle\leftrightarrow|3^2\mathrm{D}_{5/2},m_j=-5/2\rangle$  transition. The lifetime of the metastable  $3^2\mathrm{D}_{5/2}$  state is reduced by using a quench laser with 854 nm, which transfers population to the short-

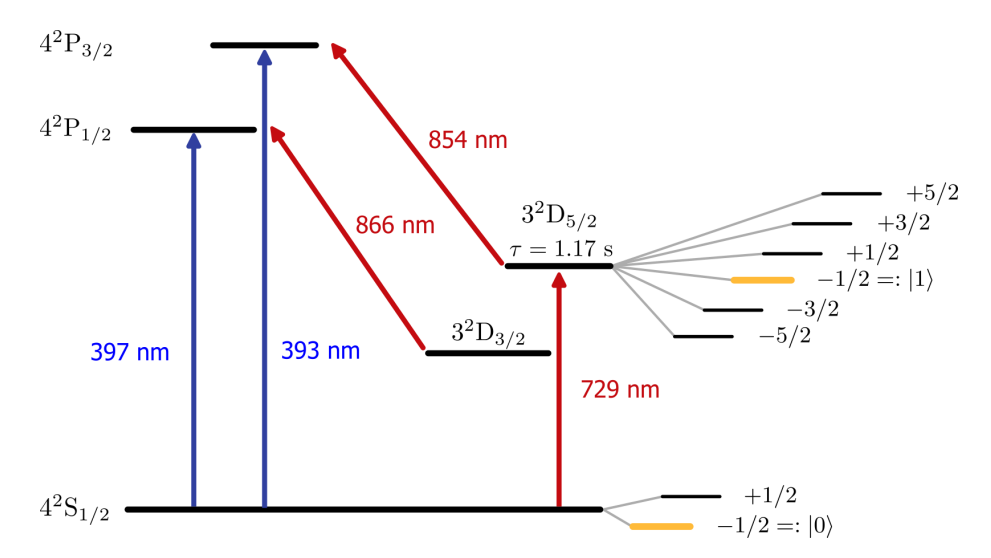


**Figure 2.8.:** Reduced level scheme of  $^{40}\mathrm{Ca^+}$  showing only the energy levels relevant for this thesis. Arrows depict transitions between states and the corresponding transition wavelengths are indicated. All transitions are accessible with laser light in the experiment except for the transition at 393 nm, which is shown here for completeness. The optical qubit is encoded in two Zeeman sub-levels of the  $^{42}\mathrm{S}_{1/2}$  ground and  $^{32}\mathrm{D}_{5/2}$  metastable state manifold, with the particular states marked in yellow.

lived  $4^2P_{3/2}$  state in order to increase the cooling rate. Optical pumping is used directly after sideband cooling as population can also decay from  $4^2P_{3/2}$  to  $|4^2S_{1/2}, m_j = +1/2\rangle$  via the  $3^2D_{3/2}$  state and would remain unaffected by sideband cooling. Optical pumping transfers this undesired population first with the qubit laser with 729 nm to the  $|4^2D_{5/2}, m_j = 1/2\rangle$  state and then with the repumping laser with 854 nm laser light to the  $3^2P_{3/2}$  state. From there, the population can decay into the desired ground state Zeeman-level with  $m_j = -1/2$ , which also initializes the qubit state to  $|0\rangle$ . Note that for both sideband cooling and optical pumping a repumping laser with 866 nm pumps undesired population out of the  $4^2D_{3/2}$  state and that sideband cooling has a smaller cooling bandwidth than Doppler cooling. As the spacing of motional frequencies is larger than the cooling bandwidth, multiply cycles of sideband cooling with varying frequency are necessary to sufficiently cool all radial modes. Thus the sequence "optical pumping followed by sideband cooling" has to be carried out multiple times. For more details see Ref. 36.

The state of the qubit is then manipulated with the qubit laser with 729 nm, where the parameters of the single-qubit resonant operations described in Sec. 2.2.2 are realized by varying the laser beam parameters incident on the ion. The pulse area of the laser pulse as the integral of power and length of the laser pulse determines the rotation angle  $\theta$ , and the axis of rotation  $\varphi$  is set by varying the phase of the laser. For two-qubit entangling gates described in Sec. 2.2.2, two time-independent frequency tones are applied to the ions in order to set the detuning of the laser from the COM mode in the frequency spectrum. Combined with a possibly time-dependent laser power, which determines the Rabi frequency of the individual ions, the entangling gate can be realized. More details are provided in Sec. 3.2.

Readout of the quantum state is carried out after qubit manipulation by means of fluorescence detection [15, 37]. The detection laser with 397 nm continuously scatters photons on the  $|4^2S_{1/2}\rangle \leftrightarrow |4^2P_{1/2}\rangle$  transition when the ion is in the  $|0\rangle$  state. These photons are detected with a charged-coupled-device (CCD) camera to obtain the quantum state of all ions that are trapped. If the ion is in state  $|1\rangle$ , then no photons are scattered and the ion remains dark. Additionally

the repumping laser with 866 nm transfers the population from the  $3^2D_{3/2}$  state.

With these mentioned steps, a complete sequence for quantum computing can be carried out. This is shown and summarized in Fig. 2.9, where the laser wavelengths used in each step are shown. Note that the ablation loading and photo-ionization steps only have to be carried out for initial loading and when ions are lost.

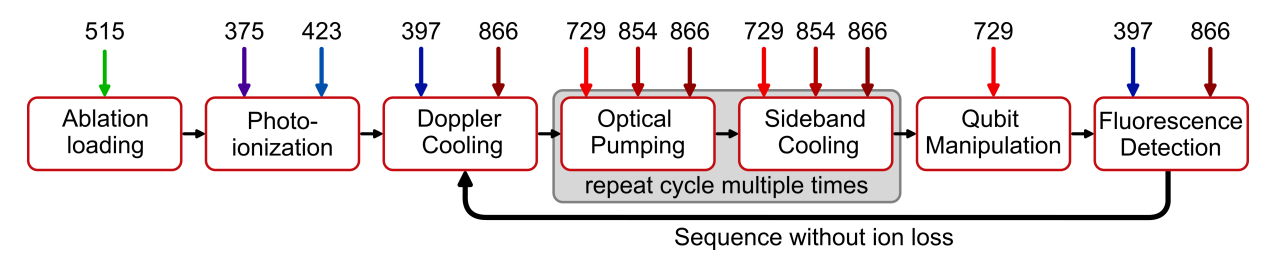


**Figure 2.9.:** Sequence for a typical quantum computation with the respective laser wavelengths indicated on top, with the first two steps only necessary when less than the required number of ions is in the trap. Depending on the number of modes to cool, the cycle of optical pumping followed by sideband cooling is repeated multiple times.

#### 2.3.3. AC-stark shift compensation

As outlined in Sec. 2.2.2 for a single two-level atom confined in a harmonic potential, a laser beam induces an AC-Stark shift that changes the atomic transition frequency by  $\Delta_{\rm AC} = -\Omega^2/(2\Delta)$  when being far-detuned from the carrier or the sideband transitions. For a bichromatic laser beam that is symmetrically detuned around the carrier transition, the induced Stark shift cancels out provided that the laser intensities are equal for the red and blue detuned frequency components. Thus the AC-Stark shift does not introduce an additional phase between the states  $|0\rangle$  and  $|1\rangle$  in an ideal two-level atom.

When using the  $^{40}$ Ca<sup>+</sup> ion in experiments however, the two-level approximation is no longer valid because in addition to the qubit transition between the states  $|0\rangle = |4^2\mathrm{S}_{1/2}, m_j = -1/2\rangle$  and  $|1\rangle = |3^2\mathrm{D}_{5/2}, m_j = -1/2\rangle$ , the coupling to additional Zeeman sublevels in the  $S_{1/2} - D_{5/2}$  manifold introduces an AC-Stark shift that is not cancelled by symmetrically detuning the red and blue frequency components of the MS gate. Moreover, the dipole-allowed transitions  $S_{1/2} \leftrightarrow P_{1/2}, S_{1/2} \leftrightarrow P_{3/2}$ , and  $D_{5/2} \leftrightarrow P_{3/2}$  also contribute to a shift in the atomic transition frequency of the qubit transition [38]. If no measure is adopted to correct for this shift, then an additional phase is accumulated during the gate operation amounting to

$$\Lambda(t) \equiv \int_0^t \omega_{\rm cl}(t') \, \mathrm{d}t', \tag{2.68}$$

with the time-dependent center line detuning defined as  $\omega_{\rm cl}(t) = \omega_{\rm eg}(t) - (\omega_r + \omega_b)/2$ . Instead of having a spin phase of  $\varphi = -\frac{\pi}{2}$  that leads to the desired rotation axis of  $\hat{S}_{\pi,m}^2 = \hat{S}_{x,k}^2$  for all modes k in Eq. 2.52, a time-dependent rotation axis will be applied during the gate operation. This leads to different path lengths of the four paths involved in the MS gate operation, shown in Fig. 2.5b, and consequently the two-photon resonance condition  $\omega_b + \omega_r = 2\omega_{\rm eg}(t)$  is violated. Compared to the case  $\omega_{\rm cl}(t) = 0$ , this results in a reduction of the gate fidelity due to displacement errors coming from unclosed modes at the end of gate time. Assuming a constant center line detuning as shown in Fig. 2.10a, the red and blue frequency components of the bichromatic laser beam

are asymmetrically positioned around the carrier transition and this shift can be compensated by different methods, two of which are outlined below.

The first method aims to account for this asymmetry by shifting both frequency tones by an asymmetric detuning  $\omega_{r,b} \to \omega_{r,b} + \Lambda(\tau) = \omega_{r,b} + \omega_{cl} \cdot \tau$  that is equal to the induced AC-Stark shift, with the last equality holding true for a constant center line detuning  $\omega_{cl}(t) = \omega_{cl}$  as shown in Fig. 2.10b. This restores the symmetry of the frequency tones if a rectangular pulse shape is used for the MS gate. However in the experiment, amplitude pulse shaping techniques are employed to reduce the off-resonant carrier excitation [22] by using a Blackman window for the slopes at the beginning and end of the pulse [39] for 10 µs each. This shaping time only constitutes a small fraction of a typical 300 µs gate time but introduces an additional phase due to the time-dependent AC-Stark shift during shaping that needs to be accounted for in subsequent gate operations [40]. This problem becomes even more pronounced when employing amplitude modulation techniques, as the time dependence of the AC-Stark shift extends over the complete gate time and leads to a fidelity reduction. Additionally, in ion chains with more than two ions, different ion pairs have to be addressed with different laser powers which leads to an undesirable calibration overhead of  $\mathcal{O}(N^2)$  parameters to ensure ideal operation of the gate.

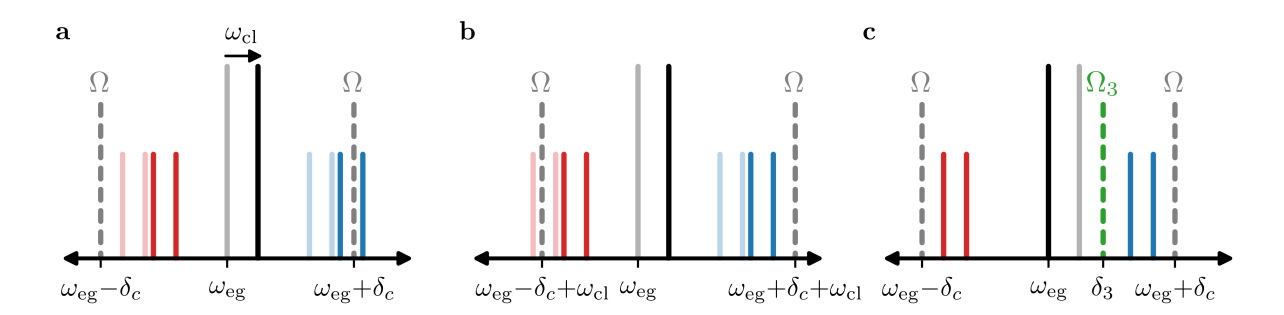


Figure 2.10.: Compensation of the AC-Stark shift, with dashed lines indicating light fields shown with their respective Rabi frequencies. **a**, AC-Stark shift of the carrier/qubit transition  $\omega_{\rm eg}$  caused by the bichromatic light field of an MS gate. This is because the  $^{40}$ Ca<sup>+</sup> ion is not a two level atom and it results in incorrect frequencies for the bichromatic light field. **b**, Center line detuning corrects for this shift by updating all frequencies in the software to account for the shifted carrier transition. **c**, Adding a third off-resonant frequency tone and calibrating its amplitude leads to an additional Stark-shift that shifts the carrier transition back.

Considering these points, a second approach is preferred that physically compensates for the induced AC-Stark shift by introducing a third frequency tone as outlined in Ref. 38 for  $^{40}$ Ca<sup>+</sup> and was first proposed for cold atoms in Ref. 41. As depicted in Fig. 2.10c, this third tone introduces an AC-Stark shift of opposite sign that cancels the AC-Stark shift originating from the bichromatic light field for appropriately chosen values of the detuning  $\delta_3$  and the power  $\Omega_3$ . The detuning is chosen such that it is not resonant with any motional sideband frequencies and stays the same for each addressed ion pair. For the power  $\Omega_3$  it is important to consider that the setup for the coherent 729 nm laser, described in Sec. 3.2, adjusts the power of the third tone always relative to that of the bichromatic frequency tones  $\Omega$  and applies it to the same laser beam. The constant power ratio  $\Omega_3/\Omega$  ensures the cancellation of the AC-Stark shift even for amplitude modulated MS gates and reduces the calibration to one ion pair, as the relative power ratio naturally accounts for the varying power required for different ion pairs. This approach also has the advantage that it is more robust against optical power fluctuations, as all three tones are

#### 2. Theoretical framework

applied onto the same laser beam and the relative power accounts for possible fluctuations. The downside is that part of the power of the bichromatic frequency tones is diverted to the third tone and less power remains available for the MS gate.

Considering all these factors, the second approach offers more desirable properties and this approach is therefore used in the experiment. After having discussed the ion trap quantum computing platform in this section, the next chapter will give an overview over the relevant electronic and optical hardware necessary for the implementation of coherent operations using the 729 nm laser

# 3. Experimental setup

The preceding Chap. 2 provided a brief theoretical basis for the ion trap quantum computing platform. This chapter will build upon this foundation and focus on the specific experimental setup that is required for the implementation of high-fidelity, addressed quantum operations.

All the experiments in this thesis have been carried out on the AQTION setup, which is short for "Advanced Quantum Computation with Trapped IONs". The goal in building this setup was to transition away from the typical laboratory environment with optical tables towards a compact and readily scalable setup, which was accomplished by fitting a fully operational quantum computer inside two 19" server racks. Instead of covering every aspect of the setup, this chapter focuses on the required hard- and software to coherently and reproducible manipulate the quantum state of ions. This necessitates the phase-coherent generation of radio frequency (RF) signals and the required control electronics and software is discussed in Sec. 3.1. These RF signals are then used to modulate a laser beam via acousto-optical modulators (AOMs) and deflectors (AODs), and the function of each optical element is outlined in Sec. 3.2. For details about the complete setup, reference [42] gives a comprehensive description of the initial setup along with characterization results and additional details regarding the setup can be found in the thesis [36].

# 3.1. Radio frequency generation and control

The focus in this section is on the hard- and software for the generation of RF signals in the AQTION setup. These signals need to fulfill certain requirements as they serve as the input signals for the AOMs and AODs, which control the amplitude, frequency, and phase of the laser beam incident on the ions. Gate operations on the trapped-ion architecture are typically performed on microsecond timescale, which requires the timing resolution of the individual pulses to be below 10 ns such that pulse length errors do not exceed 1% [42]. Ideally, the timing resolution is on the order of single nanoseconds or below. Failure to meet the timing requirement results in pulse area fluctuations that lead, as an example, to errors in the entangling phase of the MS gate. Another important requirement is the phase coherence of all generated RF signals, that are directly manipulating the laser beam needed for coherent operations. Phase coherence needs to be maintained for times much longer than typical sequence lengths on the order of 100 ms.

The control system that is used in this thesis is the Advanced Real-Time Infrastructure for Quantum physics (ARTIQ) that is tailored to meet the requirements of experiments in quantum physics. ARTIQ is a control software that provides a link between the time-critical and phase-coherent RF signal generation and the experimental control or host PC. This distinction is necessary as the latter cannot guarantee time-critical code execution because of communication latency and it also handles other tasks related to the successful operation of the experiment.

As shown in Fig. 3.1, the ARTIQ control software provides a high-level Python code interface, which differentiates between normal Python code that runs on the host PC and special kernel

functions marked with the @kernel decorator for time-critical code. These kernel functions are compiled to so called ARTIQ kernels and are sent via Ethernet to the Sinara 1124 Carrier "Kasli" hardware module [43] at the beginning of the code execution on the host PC. The "Kasli" module is equipped with the Artix-7 100T field programmable gate array (FPGA), that features Central Processing Units (CPUs) for communication with the host PC and scheduling of the pulse sequence.

If part of the Python code calls a kernel function, then the kernel CPU on the FPGA processes the respective ARTIQ kernel while utilizing the Real Time Input/Ouput (RTIO) system. This converts the ARTIQ kernel to a set of timestamps and instructions for each manipulated output channel on the daughter cards of the "Kasli". The important point for fulfilling the nanosecond timing requirement is that the timestamps of the individual instructions are aligned to an absolute wall clock that is independent of the non-deterministic timing of the normal Python code. The wall clock is generated from an external signal generator with a frequency of 10 MHz and is upconverted to 125 MHz. This set of instructions is then sent from the kernel CPU to the Scalable Event Dispatcher (SED), which is a first-in-first-out (FIFO) buffer that dispatches the instructions further to the real-time gateware. As specialized firmware on the FPGA, the gateware sends these instructions to the respective daughter cards, where they are further processed and converted to analog electric signals before being emitted at the respective output channel.

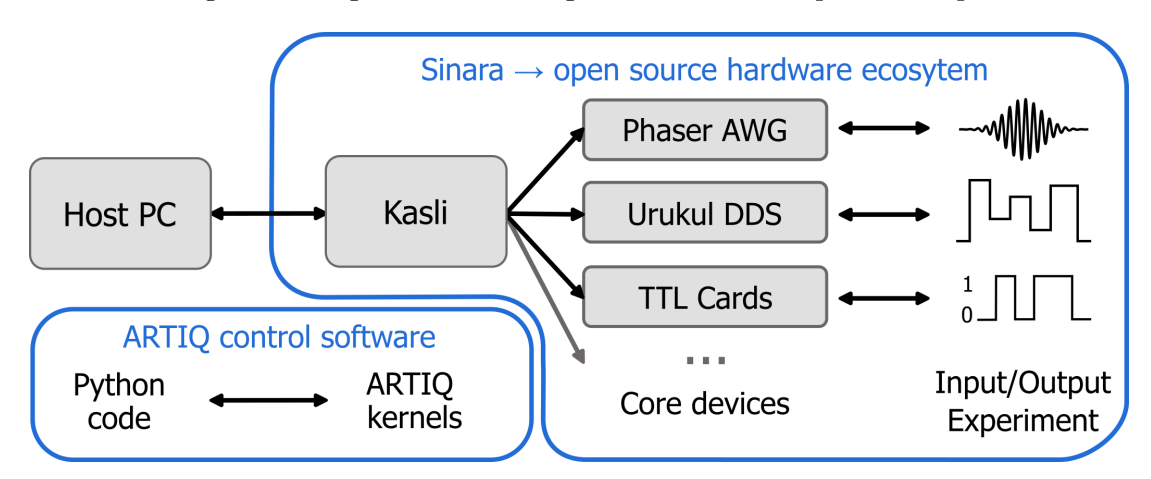


**Figure 3.1.:** Overview of the ARTIQ and Sinara hardware ecosystem. The ARTIQ control software links the asynchronous operation of the host PC with the RF signal generation using the Sinara hardware ecosystem, that guarantees nanosecond timing resolution of the emitted pulses. The "Kasli" module communicates with the host PC and relays instructions to different core devices used in the experiment, each with different signal generation capabilities. Relevant for the qubit manipulation are the Phaser AWG and Urukul DDS modules.

With currently more than 10 different core devices available, the Sinara hardware ecosystem offers a variety of devices, each of which providing different capabilities in terms of electronic signal processing/generation. Digital output signals for the experiment are provided by the Sinara 2128 Transistor-transistor-logic (TTL) card, that features eight channels per card and is used among other things to trigger the camera acquisition [44]. For quantum error correction applications, the Sinara 6302 Grabber module provides fast readout of the camera pixels to enable mid-circuit measurements [45]. The main focus in this thesis however is on the Urukul and Phaser modules, as they allow for the control of the 729 nm laser that is used for qubit manipulation.

In particular, the Sinara 4410 DDS "Urukul" offers 4 channels with dedicated direct-digital

synthesis (DDS) chips [46]. The DDS technique can create an analog output signal derived from a stable reference clock, whose frequency and phase can be digitally changed in time [47]. Urukul uses the AD9910 DDS that allows the frequency to be set in  $\sim 0.25$  Hz steps in the frequency range of 1 to 400 MHz via a 32-bit frequency tuning word (FTW) that is accessible in the Python code. Additionally, the phase is adjusted with the 16-bit phase offset word (POW) and the amplitude of the emitted analog signal is scaled with a 14-bit amplitude scale factor (ASF) [48].

The capabilities of an Arbitrary Waveform Generator (AWG) can be utilized with the Sinara 4624 AWG "Phaser" device [49]. For this, the Phaser device features a dedicated XILINX Artix-7 XC7A100T FPGA chip for signal processing tasks that allows to individually place 5 frequency tones within ±10 MHz around a common carrier frequency in the range 0 MHz to 250 MHz. Each tone is set with a 32-bit FTW, 16-bit POW and 15-bit ASF and thus Phaser offers similar capabilities in terms of parameter setting to Urukul. A more detailed description of the capabilities of Phaser is given in Ref. 50. The advantage of Phaser compared to Urukul is in the flexibility and speed regarding parameter changes due to the integrated FPGA, with more details and experimental results provided in Chap. 5. After having outlined the RF generation, the next section will focus on how to transfer these RF signals into coherent laser operations for qubit manipulation.

## 3.2. Coherent operations with 729 nm laser

This chapter will explain the link between the RF signal generation and the creation of coherent single- and two-qubit gates using the 729 nm laser in the experiment. The resulting laser-ion interaction Hamiltonian should in the ideal case implement Eq. 2.22 for resonant single-qubit operations and Eq. 2.51 for the MS two-qubit operation. Note that this chapter uses frequencies f instead of angular frequencies  $\omega = 2\pi f$ , because this is the convention adopted by ARTIQ and the experimental control software.

In the AQTION setup, all coherent operations are driven by a Toptica 729 nm laser with a linewidth of  $\approx 1\,\mathrm{Hz}$  when stabilized to a reference cavity. We denote its frequency as  $f_{\rm L}$ . As shown in Fig. 3.2, the laser beam parameters such as frequency, amplitude, phase, and beam direction are then modified by four acousto-optical devices before the laser beam is incident on the ion chain. The function of each of those four optical elements and what parameter of the laser beam is changed will now be discussed in detail.

The first optical element the laser beam passes through is a double-pass (DP) AOM controlled by a single RF output channel from the Phaser AWG module. The RF frequency input to the DP AOM  $f_{\rm DP}$  is chosen such that the sum

$$f_{\rm L} + 2 \cdot f_{\rm DP} + f_{\rm FAOM} = f_{\rm L} + 2 \cdot f_{\rm DP} + f_{\rm c}$$
 (3.1)

is resonant with a desired carrier transition, which in the AQTION setup is chosen to be the  $|4^2S_{1/2}, m_j = -1/2\rangle \leftrightarrow |3^2D_{5/2}, m_j = -1/2\rangle$  transition in  $^{40}Ca^+$  with a transition frequency of  $f_{\rm eg} = \omega_{\rm eg}/(2\pi)$ . The RF frequency applied to the second optical element, a fibre-coupled AOM (FAOM), is denoted as  $f_{\rm FAOM}$  and its center frequency is  $f_{\rm c} = 146.85\,{\rm MHz}$ . This corresponds to the frequency of the RF input signal that results in the highest transmitted light intensity in the first diffraction order of the FAOM output. Note that the laser frequency  $f_{\rm L}$  drifts over time because, among other things, the length of the reference cavity changes and these changes are corrected for by  $f_{\rm DP}$ . Control over the amplitude of the laser beam occurs also at the DP AOM,

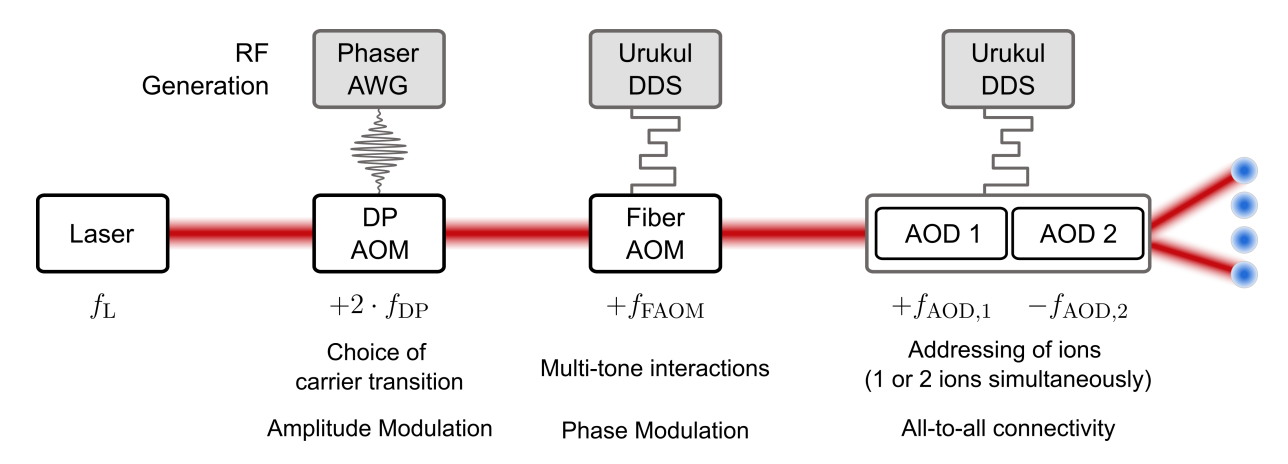


**Figure 3.2.:** Addressing setup for the 729 nm laser and the respective function of the individual optical elements. Below each element the diffraction order is displayed that is fed into the next element or to the ions (corresponds to the sign of the frequencies except for the DP, where twice the first order has been used).

with the DP AOM acting as a light switch that blocks the laser beam from reaching the ions if no RF signal is supplied. For a nonzero RF signal the amplitude of the RF signal translates roughly linearly to the amplitude of the transmitted laser beam via acousto-optic transduction when operating in the frequency region of interest. The Phaser was chosen to supply this RF signal as it provides more capabilities regarding pulse shaping than the Urukul DDS module. This is important for reducing the off-resonant carrier excitation by shaping the pulse form of the MS gate as well as for the implementation of amplitude modulated MS gates, which is discussed in Chap. 4. Note that for single-qubit gates the phase and with it the rotation axis of a resonant operation is adjusted with the Phaser.

The second element after the DP AOM is the FAOM, which receives its RF signal from up to three channels of the Urukul board. For resonant single-qubit gates, only a single frequency tone equal to the center frequency of the FAOM  $f_{\rm FAOM} = f_{\rm c}$  is applied. For MS gates, two frequency tones from two separate Urukul channels are supplied to create the bichromatic light field with frequencies  $f_c \pm \delta_c/(2\pi)$ . For both cases, the AC-Stark shift compensation using a third frequency tone is always enabled during the full qubit manipulation sequence. This third tone is also generated with the FAOM and has the frequency  $f_c + \delta_3$ . In contrast to the DP AOM, where the power of the RF signal can be set to zero, a constant power is supplied to the FAOM at all times. Given that the third tone is always on during the qubit manipulation with the same power, this means that the power of the single tone needs to match the power of the bichromatic frequency tones such that the total power going into the FAOM stays constant. This is done in order to minimize thermal effects on the FOAM that are induced by supplying varying RF input power to the FAOM. Furthermore, the phase for all applied RF signals to the FAOM is the same, which sets the desired motional phase  $\varphi_{\rm m}=0$ . The value of the spin phase  $\varphi_{\rm s}$ , that determines the rotation axis of the MS gate, is set by the AODs to account for differences in cable lengths that supply the RF signal to the optical elements.

Note that for the implementation of phase modulated entangling gates in the AQTION setup, the phase difference between the two bichromatic tones would have to be changed on the FAOM. This ensures that the interaction basis  $\hat{S}_{\pi/2-\varphi_s}$  remains constant and only the motional phase  $\varphi_{\rm m}$  is changed. However, this would necessitate the use of the Phaser instead of the Urukul module

#### 3. Experimental setup

for supplying the RF signals to the FAOM. The reason for this is that the reduced parameter update rate of Urukul would prohibit the implementation of phase modulation schemes that rely on multiple phase changes during a single MS gate.

The only remaining task is the addressing of up to two ions simultaneously with the laser beam, which is carried out by a dedicated AOD addressing unit composed of two crossed AODs that are each supplied by up to two channels of the Urukul. The setup is shown in Ref. 42 and has the advantage, that by using the +1st diffraction order for the first AOD and the -1st diffraction order for the second AOD, no net frequency shift is introduced to the laser beam when the RF frequencies to the AODs  $f_{AOD,1} = f_{AOD,2}$  are the same. The addressing unit allows for the horizontal displacement of the laser beam (along the ion chain) by changing the frequency on both AODs by the same amount, with the frequency that needs to be set determined by calibration. This approach ensures pairwise all-to-all connectivity, as simultaneous application of two frequency tones on both AODs enables the addressing of an arbitrary pair of ions. When the whole ion chain is displaced with respect to the horizontal plane of the addressing unit, a vertical displacement of the laser beam can be introduced by changing the frequency on both AODs in opposite directions. This opposite change of frequencies introduces a frequency shift of the laser beam that is compensated by shifting the DP AOM frequency  $f_{\rm DP}$ . As mentioned in the preceding paragraph, the rotation axis of the MS gate can be adjusted by changing the phases of the RF signals going into each of the two AODs.

To summarize, the frequency of the laser beam incident on the ions is adjusted to

$$f_{\rm L} + 2f_{\rm DP} + f_{\rm FAOM} + f_{\rm AOD,1} - f_{\rm AOD,2} = \begin{cases} f_{\rm eg} & \text{for resonant single qubit gates} \\ f_{\rm eg} \pm f_{\rm sidebands} & \text{for MS two-qubit gates} \end{cases}$$
(3.2)

depending on the type of gate. Note that the third tone has been excluded from this equation, as it is always on during the qubit manipulation and its frequency and amplitude remain constant.

# 4. Frequency-robust entangling gate using amplitude modulation

After having introduced the necessary theoretical concepts as well as the experimental setup, the following chapter will introduce an optimal control technique with the aim of improving the currently used gate implementation. In the following Sec. 4.1, the current limitations of the AQTION setup regarding entangling gates are discussed alongside possible solutions for addressing them. Frequency-robust entangling gates using amplitude modulation from Ref. 51 are then introduced in Sec. 4.2 as a means to reduce residual mode coupling, one of the largest contributors to gate errors in the current setup. The amplitude modulated entangling gate utilizing the Mølmer Sørensen interaction promises to be more robust against motional mode frequency changes compared to unmodulated entangling gates. Furthermore the technique offers a way to scale the setup beyond 16 ions, which is currently limited among other things by the entangling gate performance. The technique was chosen based on the RF generation capabilities discussed in Chap. 5. It consists of two parts, with the numerical optimization part introduced in Sec. 4.3. The results will in turn aid the parameter choice for an experimental calibration procedure that is outlined in Sec. 4.4.

## 4.1. Limitations of current setup

In this section, the limitations of the current AQTION setup with respect to the MS gate fidelity are outlined and analyzed by constructing a rudimentary error budget based on numerical simulations. The simulations consider both the imperfection of the MS gate itself as well as environmentally induced errors. This will allow the identification of possible improvements to the setup and/or the gate execution and will show why the introduction of amplitude modulation to MS gates could reduce a major source of error.

The first part of the numerical simulation is called *phase space simulation* and is based on Eq. 2.52 with a constant Rabi frequency over the whole gate time from t=0 to  $t=\tau$ . The required inputs for this simulation are the number of ions, which is  $n_{\rm ions}=16$  for the AQTION setup, the two radial  $f_{\rm COM,x}=3095.36\,\rm kHz$ ,  $f_{\rm COM,y}=3177.00\,\rm kHz$ , and the axial  $f_{\rm COM,z}=383.20\,\rm kHz$  COM mode frequencies. Note that the two radial COM mode frequencies are measured in the experiment but the axial COM mode frequency shown here is not. Instead, an effective axial COM mode frequency is used for calculating the radial mode spectrum and it is computed by numerically minimizing the difference between the measured and calculated spectra. The reason

<sup>&</sup>lt;sup>1</sup>The underlying code for these numerical simulations is based on a Gaussian waveform for the Rabi frequency. By choosing a large width of the Gaussian waveform, a constant Rabi frequency with negligible time dependence can be realized. The simulation with the Gaussian waveform was written for the frequency-robust entangling gate that will be introduced in Sec. 4.2. The results obtained from it for a constant Rabi frequency have been successfully cross-checked with the results of a simulation that was explicitly written for a constant Rabi frequency, thus offering an additional validation step.

for this discrepancy is that the calculation of the motional mode frequencies neglects, among other things, the coupling of the radial to the axial mode frequencies. For reference, the measured axial COM mode frequency is  $f_{\rm COM,\,z,\,meas}=369.2\,{\rm kHz}$  and is only used in simulations if one would be interested in the axial mode spectrum.

From these three frequencies  $f_{\rm COM,\,x}$ ,  $f_{\rm COM,\,y}$  and  $f_{\rm COM,\,z}$  and the number of ions  $n_{\rm ions}$  the radial mode spectrum alongside the LD factors can be calculated following Ref. 14. The axial mode spectrum is not of interest in the following considerations as the AQTION setup employs radial addressing for the qubit manipulation step and the excitation of axial modes is negligible. The calculated blue sideband radial mode spectrum is shown in Fig. 4.1a, with the detuning of the laser beam by  $\delta = 1/\tau = 3.33\,{\rm kHz}$  from the radial-y COM mode indicated in grey. Clearly visible in this spectrum is the mode crowding towards the radial COM mode frequencies.

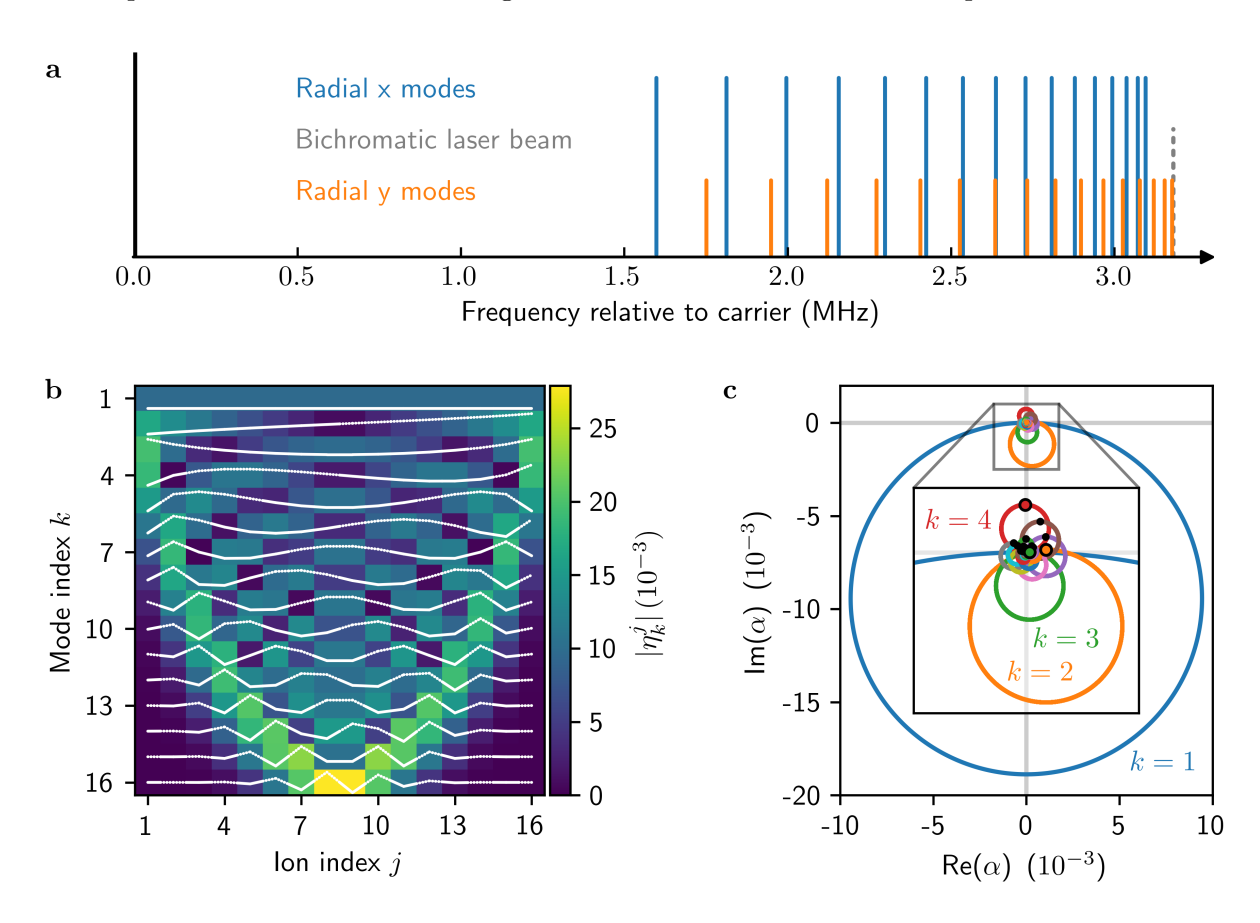


**Figure 4.1.:** a, Radial mode spectrum for 16 ions in the AQTION setup, where only the BSBs are shown. b, LD factors for ion index j and radial y-mode with index k, with the absolute value of the LD factor encoded in the colours. The white curves include the sign of the LD factors to show the dependence of the LD factor for each mode k on the ion index j. c, Phase space simulation for the outer ion pair 1-16 to indicate the displacement error at time  $t = \tau$ . The position of the phase space trajectory at time  $t = \tau$  is indicated by coloured dots in the respective colour of the mode up to k = 4, all other endpoints are shown in black.

Figure 4.1b shows the absolute values of the LD factors for the radial-y modes for a given ion index j and mode index k, with the LD factors for the radial-x modes only slightly deviating from these values due to different mode frequencies. The white curves include the sign of the LD factor

to visualize the coupling of certain modes to different ions, with solid (dotted) lines indicating a negative (positive) value. The COM mode with mode index k = 1 for example couples equally to all ions, whereas the rocking mode k = 2 couples stronger to the outer ions 1-16 compared to the center ions 8-9, with the LD factors changing sign between ions 8 and 9.

In Fig. 4.1c the phase space trajectory of an MS gate with  $\delta=3.33\,\mathrm{kHz}$  and a gate time of  $\tau=300\,\mathrm{ps}$  is shown. For a constant Rabi frequency during the gate time the COM mode completes one whole circle and is decoupled, starting and ending at the origin of phase space. This is however not true for the other modes, whose trajectory still starts at the origin of phase space but does not return to it after a time  $t=\tau$  because the detuning  $\delta_k$  is different and the relation  $\delta_k=1/\tau$  is violated. A consequence of this is that the phase space trajectory of modes with mode index k>1 take less time for a single revolution and hence complete multiple revolutions during the gate time. The displacement of those modes leads to residual spin-motion entanglement, which results in a decrease in the gate fidelity. Ensuring that all loops close simultaneously once the gate concludes would require a gate time  $\tau$  in excess of the observed coherence time. The reason for this is that one would need to take the least common multiple of loop closing times  $\tau_k=1/\delta_k$ , making the approach of scaling the gate time infeasible.

Instead, the gate time  $\tau=300\,\mathrm{ps}$  was chosen based on numerical simulations, with the results of phase space simulation illustrated in Fig. 4.2. For each gate time in the range 150 µs to 500 µs, the detuning was set to  $\delta=1/\tau$  such that the phase space trajectory of the radial-y COM mode makes a single revolution and concludes its trajectory at the origin of phase space. In a second step the Rabi frequency was adjusted such that the MS gate implements the desired entangling phase of  $\Phi=-\pi/2$ , hence there is no rotation angle error in the phase space simulation and solely the effect of displacement errors is investigated. In Fig. 4.2a only the radial-y COM and rocking mode have been considered for two ion pairs to illustrate the importance of the coupling of different modes to ions. The average gate fidelity  $\bar{\mathcal{F}}$  for the inner ion pair 8-9 stays constantly above 99.999% for all gate times because the coupling of the rocking mode to this pair is negligible. This is in contrast to the outer ion pair 1-16, where the coupling of the rocking mode is strongest among all ions and an oscillatory behaviour in the gate fidelity arises. Peaks in the fidelity indicate that the phase space trajectory of the rocking mode is closed, which in the case of 301.8 µs takes seven revolutions in phase space.

When taking into account the five highest frequency modes as shown in Fig. 4.2b, including the radial-x COM mode frequency as the fourth highest, additional structure in the fidelity on top of the oscillatory behavior arises. This leads to oscillations in the fidelity that do not exceed 99.9%fidelity anymore for gate times below 300 µs as both the rocking mode and the third highest mode do not decouple at the same gate times anymore. This is even further amplified when considering all 32 radial modes, shown in Fig. 4.2c with a different scale of the the y-axis. The corresponding phase space picture for pair 1-16 and all 32 radial modes is shown in Fig. 4.1c, where the displacement of the individual modes is visible. Based on phase space simulation, one may be inclined to choose a gate time close to 300 µs in order to guarantee the decoupling of the rocking mode at 301.8 µs after 7 revolutions as well as the third highest frequency mode at 300.3 µs after 18 revolutions. For this gate time the average gate fidelity of all 120 ion pairs is 99.43(20)%, with pair 8-9 having the maximum and pair 1-16 the minimum fidelity with 99.73 % and 98.6 % respectively. Other possibilities where the rocking and the third highest mode decouple at roughly the same gate time would be 388 µs and 475 µs. Note that the phase space simulation ignores several relevant error sources, including off-resonant carrier excitation, amplitude pulse shaping, and system-environment interactions.

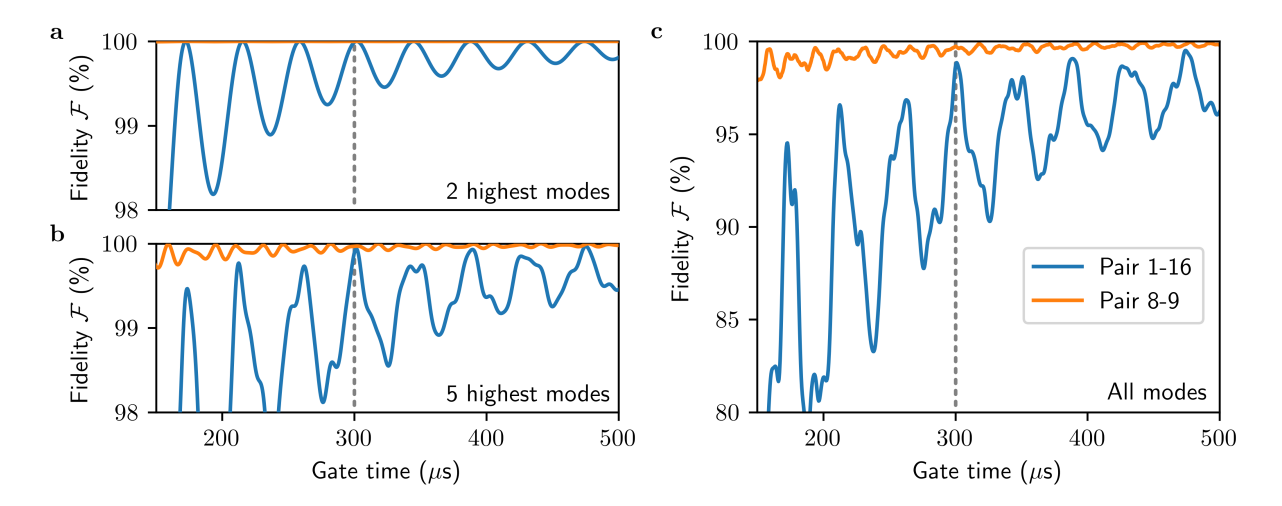


Figure 4.2.: Fidelity derived from phase space simulation. For each gate time  $\tau$ , the detuning was chosen such that the radial-y COM mode decouples after the gate time. Additionally the Rabi frequency is adjusted to implement the desired entangling phase. In  $\bf a$ , only the radial-y COM and rocking mode are considered and the fidelity is shown for the outer 1-16 and the inner ion pair 8-9. These pairs cover the minimum (1-16) as well as the maximum (8-9) fidelity of all 120 pairs in a 16-ion chain because of their LD factors. Additional structure in the fidelity can be observed in  $\bf b$ , that includes the five highest modes. All 32 radial modes are considered in  $\bf c$ , where the y-axis has a different scale compared to the left column of figures.

The latter factor is investigated in the second simulation method. One assumption up until now was that the Hamiltonian modelling the system is a closed quantum system and it can be described with a unitary time evolution. Based on this assumption, the displacement error originating from residual coupling of radial modes could be simulated with phase space simulation. In experimental settings however, the quantum system is embedded into a larger environment called total system that is considered as a closed system. Our system of interest, which is simply a subsystem of the larger total system, interacts with the environment in a non-deterministic and uncontrolled way. Given that solving the full dynamics of the total system is unfeasible, one usually resorts to so called master equations, that try to obtain the time evolution of the system from the total system. When assuming that the interaction with the environment is a stochastic Markov process, then the time evolution of the density matrix can be obtained with the Lindblad master equation, also called Gorini-Kossakowski-Sudarshan-Lindblad equation [52], which is given by

$$\dot{\rho}(t) = -\frac{i}{\hbar} [\hat{\mathcal{H}}(t), \rho(t)] + \sum_{\xi} \sum_{k} \left[ \hat{\mathcal{L}}_{\xi,k} \rho(t) \hat{\mathcal{L}}_{\xi,k}^{\dagger} - \frac{1}{2} \left\{ \hat{\mathcal{L}}_{\xi,k} \hat{\mathcal{L}}_{\xi,k}^{\dagger}, \rho(t) \right\} \right]. \tag{4.1}$$

If only the first term on the right side is considered, the equation can be identified as the Von Neumann equation that governs the time evolution of a closed quantum system. By including the second part, the interaction of the system with the environment is accounted for with so called collapse operators  $\hat{\mathcal{L}}_{\xi,k} = \sqrt{\gamma_{\xi,k}}\hat{c}_{\xi,k}$ . Here,  $\gamma_{\xi,k}$  is the rate of the interaction and  $\hat{c}_{\xi,k}$  the operator acting on mode k through which the coupling occurs. In this section we are interested in three different interactions with the environment (indicated by the index  $\xi$ ) and their effect on the fidelity of the MS gate, namely the heating rate, optical, and motional decoherence.

The Hamiltonian simulation is based on the Lindblad master equation and the time evolution of the system is obtained with the QuTiP function mesolve [53]. This function returns the density matrix of the system for each specified time and returns a unitary time evolution if no collapse operator is specified. The fidelity can be obtained directly using the state preparation fidelity  $\mathcal{F}$  from Eq. 2.58 by comparing the computed density matrix with the desired target density matrix for a maximally entangled state. Note that for this simulation only the radial-y COM mode is considered.

Typical noise sources in the experiment, like magnetic field fluctuations, vary on length scales larger than the spatial extent of the ion chain. As a consequence of this, the overlap of errors induced by these noise sources with motional modes is largest for the radial-y COM mode, to which all ions couple with equal strength. In the case of motional heating, which is mainly caused by stray electric fields, the radial-y COM mode exhibits the highest heating rate among all modes. A typical heating rate for the radial-y COM mode (k=1) measured with sideband thermometry [54] is  $\gamma_{\xi_h,1} = \Delta \bar{n}/\Delta t = 3.6 \,\text{phonons/s}$ , with  $\xi_h$  indicating motional heating. The collapse operators that describes this interaction are  $\hat{\mathcal{L}}_{\xi_h,1} \in [\sqrt{\gamma_{\xi_h}}\hat{a}_1, \sqrt{\gamma_{\xi_h}}\hat{a}_1^{\dagger}]$ . For the optical  $T_2$  and motional  $T_2^{\text{mot}}$  coherence time typical values at the AQTION experiment are  $T_2 = T_2^{\text{mot}} = 50 \,\text{ms}$ . For the motional coherence  $(\xi_{\text{mot}})$  there is a collapse operator for each mode separately given by  $\hat{\mathcal{L}}_{\xi_{\text{mot}},k} = (2/T_2^{\text{mot}})^{1/2} \hat{a}_k^{\dagger} \hat{a}_k$ , whereas for the optical coherence  $(\xi_{\text{opt}})$  the single collapse operator is given by  $\hat{\mathcal{L}}_{\xi_{\text{opt}}} = \sqrt{2/T_2} \hat{J}_z$  with the collective spin operator  $\hat{J}_z = \sum_j \hat{\sigma}_{z,j}/2$ .

The result of the Hamiltonian simulation is visible in Fig. 4.3 separated into heating rate (a) and the combined effect of the optical and motional coherence (b). Given that the rate in all three cases is constant in time, the decay in fidelity is exponential, but in the considered time scale it can be modelled as a linear dependence. For a gate time of  $\tau = 300 \,\mu\text{s}$ , the infidelity induced by the heating rate is  $0.05 \,\%$  and hence makes up the smallest contribution of the three considered effects. The effect of the optical and motional coherence times on the gate fidelity is shown in Fig. 4.3b. For coherence times  $T_2 = T_2^{\text{mot}}$  there is a  $\approx 1 \,\%$  drop in the fidelity, with  $0.41 \,\%$  coming from the motional coherence and  $0.6 \,\%$  from the optical coherence.

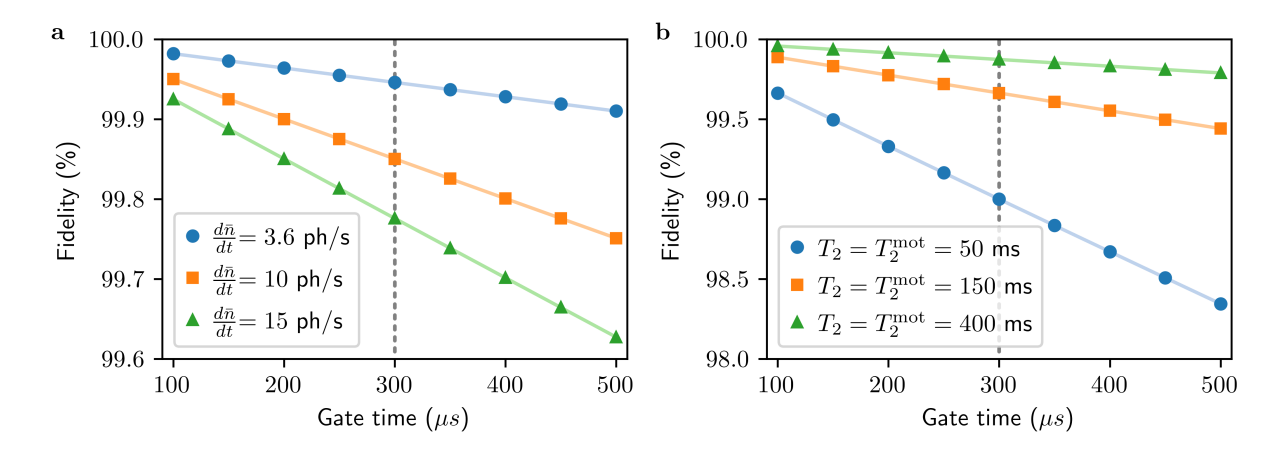
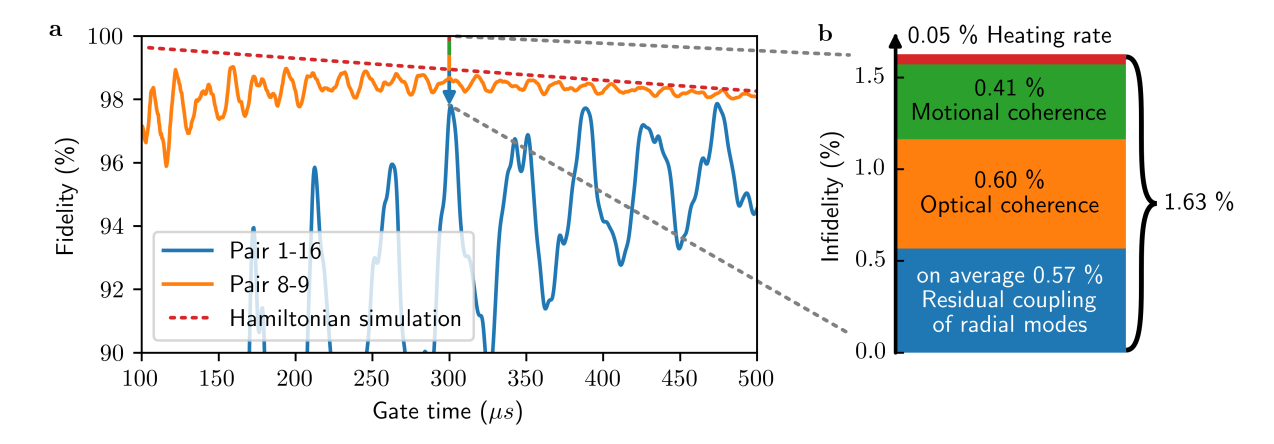


Figure 4.3.: Results from Hamiltonian simulation. **a**, The heating rate of the COM mode contributes 0.05% to the gate infidelity for a gate time of  $\tau = 300\,\mu s$ . **b**, The combined effect of the optical and motional coherence results in a  $\approx 1\%$  contribution to the gate infidelity, with the additional values shown corresponding to the Linear trap setup in Innsbruck with 150 ms and 400 ms has been measured in comparable experiments.

The combined influence of coherent and dissipative effects on the fidelity, modelled through phase space and Hamiltonian simulation respectively, is shown in Fig. 4.4 for ion pairs 1-16 and 8-9. These results are obtained by simply multiplying the fidelities of both simulations at each time step, as the environmental influence sets an upper limit on the achievable fidelity of a perfectly executed MS gate. From this it becomes apparent that a gate time of 300  $\mu$ s is the optimal choice given the system parameters. Regarding the contribution of the optical coherence on the gate fidelity, an ongoing hardware upgrade aims to decrease it by changing the magnetic field generation from coils to permanent magnets. For example coherence times of 150 ms can already result in a reduction of the gate infidelity from  $\approx 1\%$  to  $\approx 0.35\%$  and those coherence times are achieved on the Linear trap setup in Innsbruck. A coherence time of 400 ms - which has been measured in comparable experiments - would reduce the error coming from coherence times even further to  $\approx 0.1\%$ .



**Figure 4.4.: a**, Combined results obtained from phase space and Hamiltonian simulation shows that a gate time of 300 µs yields the highest fidelity. **b**, Error budget obtained from the simulation for a gate time of  $\tau = 300 \,\mu\text{s}$ , showing the average infidelity over all 120 ion pairs.

Regarding the residual coupling of radial modes, the average fidelity over all 120 pairs in a 16-ion chain is 0.57%, ranging from 0.27% for pair 8-9 to 1.4% for pair 1-16. This errors cannot be further reduced by changing either the detuning or gate time. One possible solution is to modulate the laser beam parameters during the gate time in order to achieve decoupling of more motional modes and hence increase the fidelity. This approach is outlined in the next section.

## 4.2. Theoretical motivation

In the previous section the main error sources for the MS gate in the current AQTION setup have been outlined, and the residual coupling of radial modes was identified as one of the largest contributors to the observed gate infidelity. The MS gate that is currently used in the setup uses a constant detuning  $\delta_c$  from the carrier transition  $\omega_{\rm eg}$ , phase  $\varphi_m/\varphi_s$  and Rabi frequency  $\Omega$  during the gate time  $\tau$ , apart from pulse shaping at the beginning and end of the gate time. One possibility to improve the fidelity of the MS gate is to modulate the available parameters to reduce the displacement error coming from spectator modes. Various modulation schemes exist in the literature such as phase modulation [55], frequency modulation [56], amplitude modulation [57] and combinations of them with modulation either continuously or time-discrete. In this thesis the focus is on the amplitude modulation scheme outlined in Ref. 51 and the gate is referred to

as ms\_am gate. The choice of this particular method was guided by the technical limitations of the RF generation, which is discussed in Chap. 5.

The amplitude modulation scheme outlined in Ref. 51 uses a continuous waveform that is incorporated in the time evolution by replacing the time-independent Rabi frequency  $\Omega$  with a truncated Gaussian function of the form

$$\Omega = \Omega(0 \le t \le \tau) = \Omega_0 e^{-(t - \tau/2)^2 / 2\sigma^2},\tag{4.2}$$

which is zero outside the specified times. This waveform is parameterized by the gate time  $\tau$ , the peak Rabi frequency  $\Omega_0$ , and the width  $\sigma$  that corresponds to the standard deviation of the Gaussian function. The detuning of the bichromatic laser beam frequencies from the carrier  $\delta_c$  is chosen to be constant during the gate time and it is placed inside the mode spectrum at a (numerically) pre-determined frequency, with details of how to obtain it described later in this section. These parameters that describe the gate operation are depicted in Fig. 4.5.

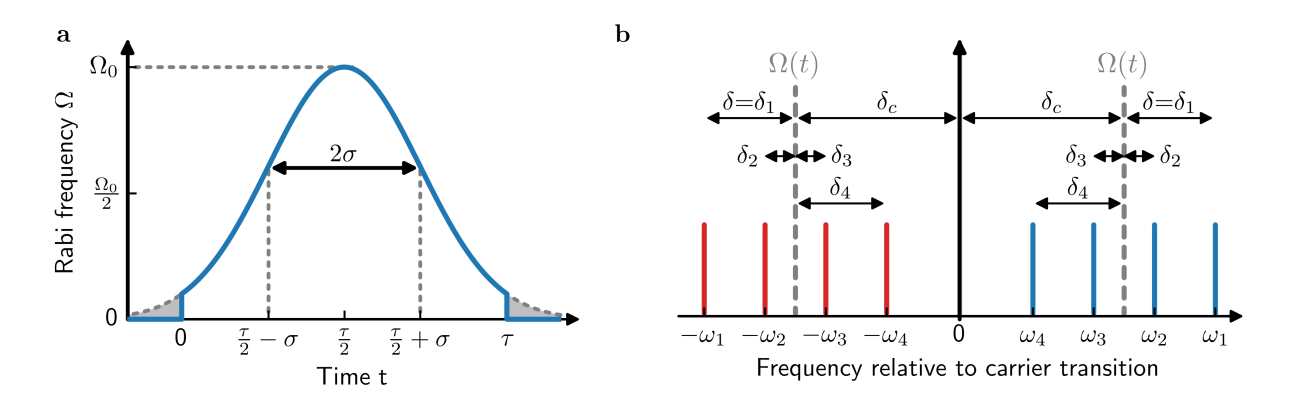


Figure 4.5.: Parameterization of the ms\_am gate. a, The Rabi frequency  $\Omega(t)$  is a truncated Gaussian waveform for times  $0 \le t \le \tau$ , with zero amplitude otherwise. b, The detuning  $\delta_c$  of the bichromatic laser beam from the carrier transition is constant during the gate time and chosen according to the condition imposed on the cost function in Eq. 4.11.

For the MS gate, the phase space trajectory  $\alpha_k(t)$  for each mode k traces out circles with the radius proportional to  $\propto \Omega/\delta_k$ , becoming smaller for modes farther away from the bichromatic laser beam frequency. In the case of amplitude modulation, the phase space trajectory for mode k is given by

$$\alpha_k(t) = i\Omega_0 \int_0^t e^{-\frac{(t' - \tau/2)^2}{2\sigma^2}} e^{-i\delta_k t'} dt'$$
(4.3)

$$= i\Omega_0 \sigma \sqrt{\frac{\pi}{2}} \exp\left[\frac{\sigma^2}{2}\kappa^2 - \frac{\tau^2}{8\sigma^2}\right] \cdot \left[\operatorname{Erf}\left(\frac{t}{\sqrt{2}\sigma} - \frac{\sigma}{\sqrt{2}}\kappa\right) - \operatorname{Erf}\left(-\kappa\right)\right]$$
(4.4)

with 
$$\kappa = \frac{\tau}{2\sigma^2} - i\delta_k$$
, (4.5)

with the error function  $\operatorname{Erf}(z)=2/\sqrt{\pi}\int_0^z \exp(-u^2)\,\mathrm{d}u$  for the complex argument  $z\in\mathbb{C}$ . The radius is now time-dependent and the normal MS gate behaviour with constant radius is recovered

for widths  $\sigma \gg \tau$ . The entangling phase  $\Phi$  is given by

$$\Phi(t) = \frac{i}{2} \sum_{k} \eta_k^{j_1} \eta_k^{j_2} \underbrace{\left[ \int_0^t \left( \frac{\mathrm{d}\alpha_k(t')}{\mathrm{d}t'} \alpha_k^*(t') - \alpha_k(t') \frac{\mathrm{d}\alpha_k^*(t')}{\mathrm{d}t'} \right) \mathrm{d}t' \right]}$$
(4.6)

$$= \sum_{k} \eta_k^{j_1} \eta_k^{j_2} \int_0^t \operatorname{Im} \left( \frac{\mathrm{d}\alpha_k(t')}{\mathrm{d}t'} \alpha_k^*(t') \right) \, \mathrm{d}t', \tag{4.7}$$

where the relations  $\operatorname{Erf}^*(z) = \operatorname{Erf}(z^*)$ ,  $\exp^*(z) = \exp(z^*)$ ,  $z_1 z_2^* + z_2 z_1^* = 2\operatorname{Im}(z_1 z_2^*)$  and the derivative of the phase space trajectory

$$\frac{\mathrm{d}\alpha_k(t')}{\mathrm{d}t'} = i\Omega_0 e^{-\frac{(t'-\tau/2)^2}{2\sigma^2}} e^{-i\delta_k t'},\tag{4.8}$$

have been used to obtain the simplified expression in Eq. 4.7. The ms\_am gate has four distinct features that make it a suitable candidate for the AQTION setup.

First, the displacement error induced by the ms\_am gate is exponentially suppressed with the distance of the mode frequency from the bichromatic frequencies  $\delta_k$ . For Gaussian waveforms whose width is small compared to the gate time  $\sigma^2 \ll \tau^2$ , the limits of integration in the phase space trajectory  $\alpha_k$  can be extended to yield

$$\alpha_k(\tau) = i\Omega_0 \int_{-\infty}^{\infty} e^{-\frac{(t'-\tau/2)^2}{2\sigma^2}} e^{-i\delta_k t'} dt'$$
(4.9)

$$|\alpha_k(\tau)|^2 \approx 2\pi\Omega_0^2 \sigma^2 e^{-\delta_k^2 \sigma^2/2},\tag{4.10}$$

which shows the exponential suppression of the displacement error by  $\delta_k^2$  when sufficiently far detuned from the closest motional mode. Second, instead of detuning the bichromatic frequencies by  $\delta=1/\tau$  from the COM mode frequency to ensure the decoupling of the COM mode phase space trajectory at the conclusion of the gate, the ms\_am gate places the bichromatic laser beam inside the mode spectrum. The so called balance point detuning  $\delta_c$  is determined by numerically minimizing the cost function

$$\frac{\mathrm{d}\Phi(\tau)}{\mathrm{d}\delta_c} = \sum_k \eta_k^{j_1} \eta_k^{j_2} \frac{\mathrm{d}\mathcal{B}_k(\tau)}{\mathrm{d}\delta_c} = 0,\tag{4.11}$$

which makes the ms\_am gate first order insensitive to rotation angle errors induced by motional mode frequency changes. At the same time the balance point detuning minimizes the second order contribution  $|d^2\Phi/d\delta_c^2|$ . The neighboring modes that are closest to  $\delta_c$  are defined as target modes for a given ion pair  $(j_1, j_2)$  and those terms usually<sup>2</sup> contribute the most to the cost function as they assume their largest value for  $\delta_k = 0$ . Without loss of generality, assume a solution is found between the target modes k = 1 and k = 2. Then the sign of the terms  $d\mathcal{B}_1/d\delta_c$  and  $d\mathcal{B}_2/d\delta_c$  is equal, but the sign of the product of LD factors  $\eta_1^{j_1}\eta_1^{j_2}$  and  $\eta_2^{j_1}\eta_2^{j_2}$  can be different. At the balance point detuning, the contribution of the target modes to the entangling phase is of opposite sign and hence compensated in first order for mode frequency changes that shift the detuning of each mode by an equal amount. This is a justified assumption as the target modes are in most cases only tens of kHz apart.

<sup>&</sup>lt;sup>2</sup>Exceptions can occur when the product of LD factors of non-target modes is larger than those of the target modes.

For large ion chains with N>10 ions, the effect of mode crowding towards the COM mode frequency becomes more pronounced. Since the contribution of motional modes k to the rotation angle is proportional to  $\Phi \propto 1/\delta_k$ , this leads to the case that several modes contribute significantly to the rotation angle. Furthermore, because of  $\Phi \propto \eta_k^{j_1} \eta_k^{j_2}$ , modes that are farther away from the bichromatic frequencies but posses a larger product of LD parameters than the target modes, could contribute more to the entangling phase than the target modes. These two effects are taken into account in the cost function by summing over all motional modes. The minimization of this cost function as well as its properties are described in more detail in the following Sec. 4.3.

Third, the ms\_am gate is described by a small set of parameters for a given mode spectrum and ion number, with the gate time  $\tau$  and width  $\sigma$  of the Gaussian waveform kept the same for all ion pairs. The ms\_am gate for individual ion pairs is then described by just the detuning  $\delta_c$  and the peak Rabi frequency  $\Omega_0$ , which simplifies the implementation in hardware. Additionally, this speeds up the numerical optimization compared to other modulation methods as only a single numerical integral has to be evaluated. Fourth, frequency-robust entangling gates are less sensitive to deviations of the waveform compared to other modulation methods. This makes them suitable for experimental use, where several factors like the AOM diffraction efficiency can alter the waveform. Figure 4.6a shows the time evolution for an ms\_am gate in comparison to a standard MS gate. The maximum excitation of the intermediate states  $|01\rangle + |10\rangle$ , where the phonon number is changed, is smaller in the ms\_am gate, illustrating the robustness against mode frequency changes. The time-dependent radii of the phase space trajectory for the ms\_am gate is shown in Fig. 4.6b.

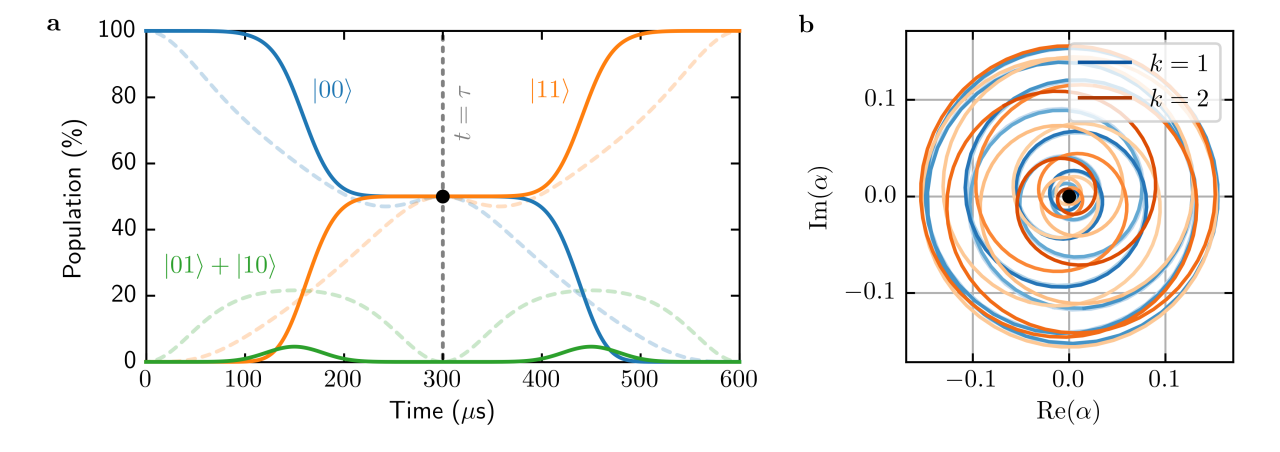


Figure 4.6.: a, Illustrative time evolution of the ms\_am gate for two modes  $f_1 = 2230 \,\mathrm{kHz}$  and  $f_2 = 2140 \,\mathrm{kHz}$ . For comparison, the dashed lines show the time evolution of a standard MS gate for a single decoupled mode  $f_1$ . Both gates realize a maximally entangled state at the gate time of 300 µs in this example. b, Phase space trajectory of the ms\_am gate showing the time-dependent radii for modes k=1 and k=2.

## 4.3. Numerical optimization

This section describes how the numerical optimization of the cost function in Eq. 4.11 was implemented in the Python programming language and discusses properties of the cost function and the phase space trajectory using a 2-ion chain from the AQTION setup as an example.

The numerical optimization is implemented in a class called GaussianOptimization and takes as input the number of ions  $n_{\rm ions}=2$ , the radial COM mode frequencies  $f_{\rm COM,\,x}=3097.6\,\rm kHz$  and  $f_{\rm COM,\,y}=3177.0\,\rm kHz$  as well as the effective axial COM mode frequency  $f_{\rm COM,\,z}=846.0\,\rm kHz$ . When the class is initialized it computes the mode spectrum, which is shown as dashed lines in Fig. 4.7, in addition to the LD factors.

The method optimize then computes the numerically optimized solutions for a specified ion pair. For a 2-ion chain the only possible pair has the indices  $j_1$ - $j_2 = 1$ -2, which in zero-based numbering that is used in Python corresponds to 0-1. Additional required inputs are the gate time  $\tau = 300 \,\mu$ s and the width of the Gaussian waveform  $\sigma = 50 \,\mu$ s. With these inputs the pseudocode of the algorithm is the following:

## Pseudocode for numerical optimization

```
0.
      for ion pair j_1-j_2 in ion_pairs:
             compute d\Phi(\tau)/d\delta_c for n_{\delta_c} detuning values in [\omega_{\min}, \omega_{\max}]
1.
             \hookrightarrow numerically find roots of d\Phi(\tau)/d\delta_c with bounds computed in 1. \rightarrow \{\delta_c\}
2.
3.
                    for root in computed_roots:
                           \hookrightarrow find peak Rabi frequency \Omega_0
4.
5.
                           \hookrightarrow calculate fidelity \mathcal{F}
                    \hookrightarrow save all obtained solutions to json file
6.
7.
      \hookrightarrow order solutions (\delta_c, \Omega_0, \mathcal{F}) by specified criterion for each ion pair
```

The first step is to evaluate the cost function for  $n_{\delta_c}$  values of the detuning between the lowest  $\omega_{\min} = \omega_4$  and the highest  $\omega_{\max} = \omega_1$  mode frequency. This is done by numerically evaluating the integral in Eq. 4.11 and then calculating the difference quotient to obtain the derivative with respect to  $\delta_c$ . The result for a 2-ion chain is shown in Fig. 4.7a, where  $n_{\delta_c} = 1000$  results in a spacing between successive points of the cost function evaluation in the simulation of 197 Hz. As can be seen in the figure marked by white dots, seven roots of the cost function corresponding to a balance point detuning  $\delta_c$  exist. In a second step each of those roots<sup>3</sup> is then numerically determined by using a root finding algorithm that returns a set of balance point detunings  $\{\delta_c\}$ . Each of those detunings is determined by searching within a specified region of detunings, with the lower and higher bounds given by subsequent points of the cost-function where the sign changes. Starting point for the root finding algorithm is the intersection of the line connecting those two points with  $d\Phi(\tau)/d\delta_c = 0$ .

For each of those roots in  $\{\delta_c\}$ , the peak Rabi frequency  $\Omega_0$  is obtained by noting that Eq. 4.7 can be written as a quadratic equation  $\Phi(\tau) = \Omega_0^2 \cdot \xi$ , with  $\xi = \sum_k \eta_k^{j_1} \eta_k^{j_2} \mathcal{B}_k(\tau, \Omega_0 = 1)$  a constant that does not depend on  $\Omega_0$ . Simply solving this equation for an entangling phase that gives a maximally entangled state  $\Phi(\tau) = |\pi/2|$  yields for the peak Rabi frequency  $\Omega_0 = \sqrt{\pi/(2\xi)}$ , with the sign of the entangling phase of the gate given by  $\operatorname{sign}(\xi)$ .

In the next step, having obtained the balance-point detuning  $\delta_c$  and the peak Rabi frequency  $\Omega_0$  that completely parameterize the ms\_am gate, the fidelity is calculated with the average gate fidelity  $\bar{\mathcal{F}}$  given in Eq. 2.59. For this M+1 parameters are needed, with M parameters given by the phase space trajectory at the gate time  $\alpha_k(\tau)$  for each mode k and the additional parameter being the realized entangling phase  $\Phi(\tau) = \pm \pi/2$  that is obtained to  $10^{-16}$  precision. Note that although multiple solutions exist for each ion pair that are robust to first-order to mode frequency

<sup>&</sup>lt;sup>3</sup>One can also specify in the code that only a subset of roots shall be further examined.

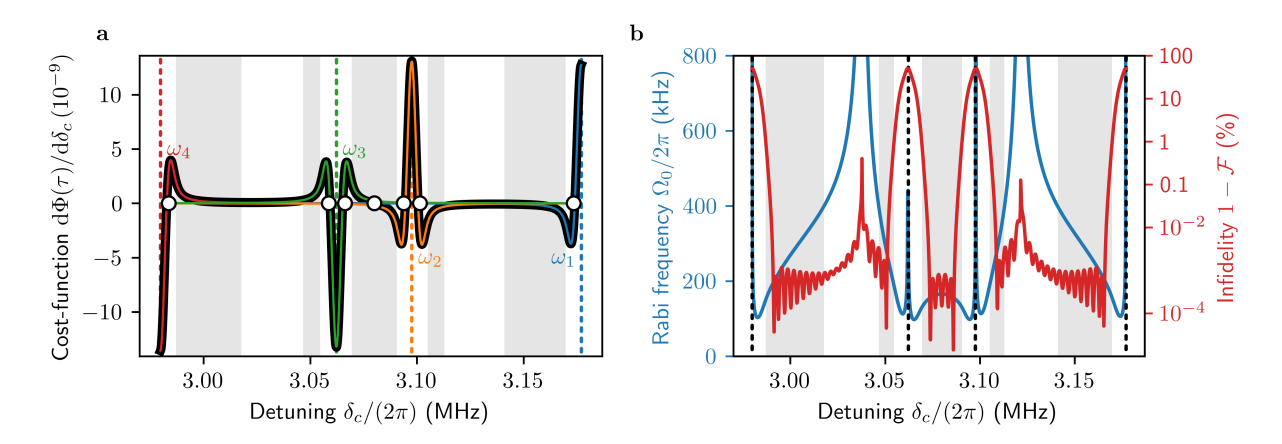
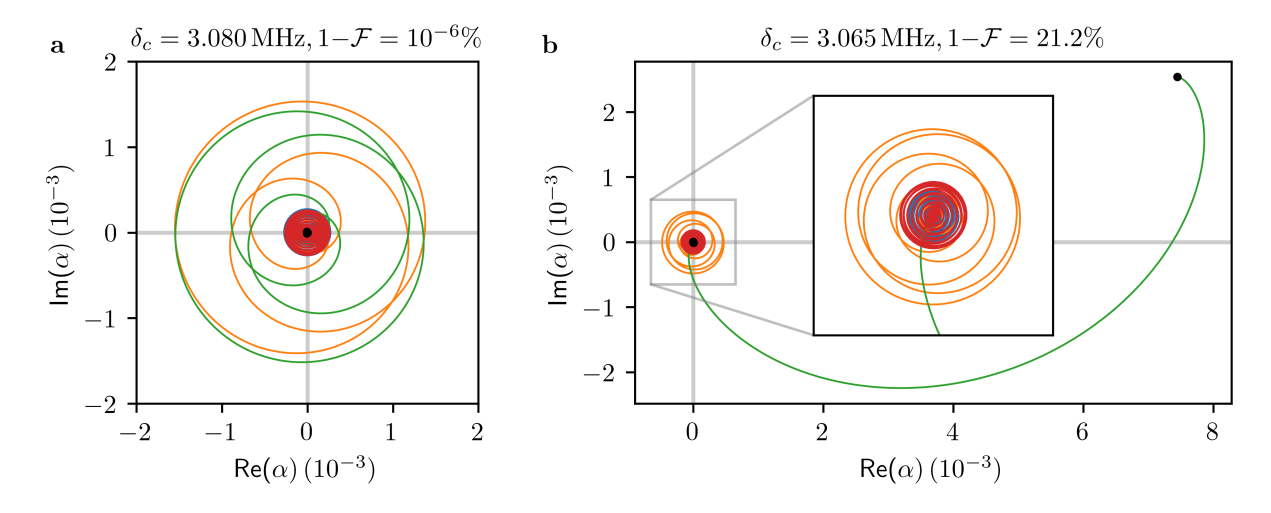


Figure 4.7.: a, Cost-function for the two ion case. The term from each of the four modes is marked in the respective colour and the seven balance-point detunings are marked in white. b, For each detuning between the four modes, the peak Rabi frequency required for creating maximally entangled states as well as the fidelity was calculated. The grey area marks gates that satisfy  $\Omega_0/(2\pi) < 400\,\mathrm{kHz}$  as well as  $\mathcal{F} > 99\,\%$ , which only one out of the seven solutions with  $\delta_c = 3.080\,\mathrm{kHz}$  fulfils.

changes, those solutions do not necessarily implement a high-fidelity ms\_am gate, as can be seen in Fig. 4.7b, where the peak Rabi frequency as well as the fidelity was calculated for multiple points. The gray areas indicate gates that simultaneously satisfy  $\Omega_0/(2\pi) < 400\,\mathrm{kHz}$  as well as  $\mathcal{F} > 99\,\%$ . Only one out of the seven solutions with  $\delta_c = 3.080\,\mathrm{kHz}$  satisfies these criteria and the corresponding phase space trajectory is shown in Fig. 4.8a. By choosing a different detuning that is not a balance-point detuning, gates that satisfy these criteria can be realized but do not offer the same robustness as gates situated at a balance-point detuning.



**Figure 4.8.:** Phase space trajectories of two out of the seven solutions for a 2-ion chain. Black points mark the phase space trajectory at the gate time  $\alpha(\tau)$ . In **a** all modes decouple, whereas in **b** mode k=3 does not. The infidelity is 21.2% higher due to the displacement error mainly coming from this mode.

Every obtained solution is then saved to a json file where they can be further analyzed. In particular, for each ion pair the solutions are ordered by the fidelity and further criteria like distance to the nearest mode can be applied. Figure 4.8 shows the phase space trajectories for

two solutions in the 2 ion case, with all modes decoupled in **a** but mode k=3 being displaced at  $t=\tau$  in **b**, resulting in a drop of the obtained gate fidelity by 21.2%.

## 4.4. Experimental calibration procedure

The experimental calibration procedure is aided by the results of the numerical simulation and aims to include experimental imperfections that affect the gate operation but are not part of the numerical simulation. There are two parameters for each ion pair that need to be calibrated to realize an ms\_am gate in the experiment, namely the balance point detuning  $\delta_c$  and the peak Rabi frequency  $\Omega_0$ .

First, the balance point detuning  $\delta_c$  is obtained by scanning the detuning of the bichromatic laser beam with respect to the carrier frequency between the target modes. For this scan the peak Rabi frequency is chosen based on numerical simulation results that give a rough estimate for the Rabi frequency that can be expected in the experiment. The minimum of the population of the  $|11\rangle$  state in the vicinity of the solution from numerical simulation then corresponds to  $\delta_c$ . This is shown in Fig. 4.9a for a 2-ion chain with mode frequencies  $f_1=2.23\,\mathrm{MHz}$  and  $f_2=2.14\,\mathrm{MHz}$ . The state populations have been obtained by means of Hamiltonian simulation with the Rabi frequency chosen to be  $\Omega_0/(2\pi)=170\,\mathrm{kHz}$  in this particular example. Second, the actual peak Rabi frequency  $\Omega_0$  in the experiment is then obtained by scanning the power of the DP-AOM, which corresponds to a scan of the peak Rabi frequency. Using the balance-point detuning from the previous calibration step, the crossing point of the  $|00\rangle$  and  $|11\rangle$  population acts as a proxy for the entangling phase that indicates maximally entangled state. In Fig. 4.9b a simulation of such a power scan is shown.

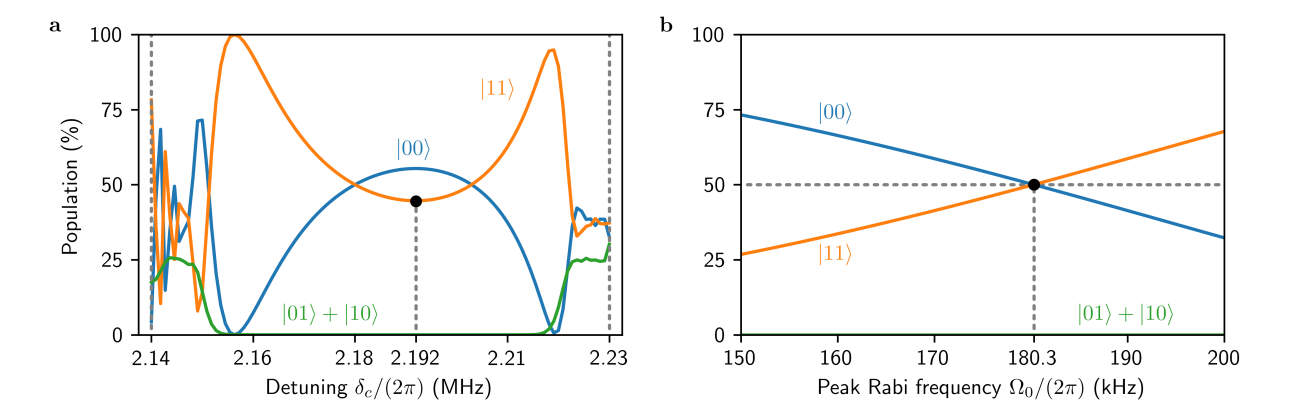


Figure 4.9.: Hamiltonian simulation for experimentally carried out calibration scans. **a**, Detuning scan to determine the balance-point detuning  $\delta_c$  situated at the minimum of the  $|11\rangle$  population in the center of the scan. **b**, Power scan to calibrate the entangling phase by adjusting the power such that the states  $|11\rangle$  and  $|00\rangle$  have the same population, hence a maximally entangled state is created.

# 5. Characterization of the ARTIQ and Sinara ecosystem

The realization of high-fidelity MS gates requires RF generators capable of synthesizing complex waveforms by controlling any combination of amplitude, phase, and frequency. Most suited for this purpose are dedicated Arbitrary Waveform Generator (AWG) devices, whose integration into the existing control software is however challenging given their standalone nature. For this reason, the Sinara "AWG" Phaser hardware module is used, which provides capabilities similar to an AWG and is already integrated into the existing software environment.

In the previous chapter the ms\_am gate was introduced as an amplitude modulated variant of the MS gate with the prospect of reducing the gate error coming from residual coupling of radial modes in the current AQTION setup. This method was chosen based on an investigation into the technical capabilities and limitations of Phaser presented in this chapter. In particular, Sec. 5.1 extends the information about the Sinara Phaser module given in Sec. 3.1 by discussing the relevant signal processing pipeline. Then, in Sec. 5.2 the RF generation capabilities of Phaser are tested by measuring the light intensity of the laser beam after a DP-AOM, which is controlled by RF signals generated by the Phaser module. Here, the focus is on the behaviour of the light intensity when changing the amplitude and/or the phase as well as on achievable parameter update times.

## 5.1. RF generation capabilities

This section provides a more comprehensive overview of the Sinara Phaser module by extending the information provided in Sec. 3.1. A simplified signal processing pipeline for one of the two output channels of the Phaser module is shown in Fig. 5.1 to illustrate which parameters are accessible and how they affect the analog RF output signal. The output signal contains up to five tones, whose frequency, phase, and amplitude can be independently set by Numerically Controlled Oscillators (NCOs) on the Kasli RTIO gateware. In the following discussions, only a single frequency tone per Phaser output channel is considered as this is sufficient for most of the MS modulation schemes that are feasible for the AQTION setup. For this single tone, a 32 bit FTW (kasli\_freq) ensures a frequency resolution of  $\sim 2.9\,\mathrm{mHz}$  in the range of  $\pm 12.5\,\mathrm{MHz}$  around the carrier frequency, whereas a 16 bit POW (kasli\_phase) provides phase control with a resolution of  $\sim 15\,\mathrm{\mu rad}$ . The amplitude of each oscillator is set via a 15 bit ASF (kasli\_amp). The NCOs generate digital in-phase and quadrature components (I/Q) for each oscillator with 25 Mega samples per second (MS/s) and the signal for each oscillator is summed up to obtain a single digital I/Q signal with 25 MS/s.

The digital I/Q signal is then sent via a FastLink connection to the FPGA gateware on the Phaser module, where it is interpolated from  $25\,\mathrm{MS/s}$  to  $500\,\mathrm{MS/s}$  using digital filters. These filters additionally remove undesired frequency components, with the amplitude of the signal varying

less than  $10^{-3}$  in the passband frequency range [-10,10] MHz. Frequencies in the stopband outside the range [-15,15] MHz are being attenuated by a minimum of 75 dB. The resulting signal is then mixed with an NCO operating at  $500\,\mathrm{MS/s}$  to implement a Digital Up-Converter (DUC). The DUC additionally allows to shift the frequency for all tones to a desired RF window with a 32 bit FTW (duc\_frequency) and also the phase can be adjusted with a 16 bit POW (duc\_phase). On the Digital to Analog Converter (DAC) "DAC34H84" the resulting signal is then interpolated from  $500\,\mathrm{MS/s}$  to  $1\,\mathrm{GS/s}$ , with a passband of  $\pm 200\,\mathrm{MHz}$  that wraps around at  $\pm 250\,\mathrm{MHz}$  (e.g.  $251\,\mathrm{MHz}$  corresponds to  $-249\,\mathrm{MHz}$  again), before it is converted to an analog I/Q signal.

This analog signal is then sent through an Anti-Aliasing (AA) filter with a specified cut-off frequency of 340 MHz, which was measured to be closer to 200 MHz due to a filter design error [58]. In the Phaser baseband version that is used in the AQTION setup, the signal is then passed through a variable attenuator (analog\_attenuation) with a maximum attenuation of 31.5 dB, whose value is set to 0 dB in all considered examples. The analog signal is then emitted at the frontend of the Phaser module at a Micro-miniature coaxial (MMCX) output port. An overview of all discussed parameters and where they are physically changed is shown in Fig. 5.1. In the next section the capabilities of Phaser in terms of parameter update times as well as the behaviour of the RF output signal when changing the amplitude and/or phase are discussed.

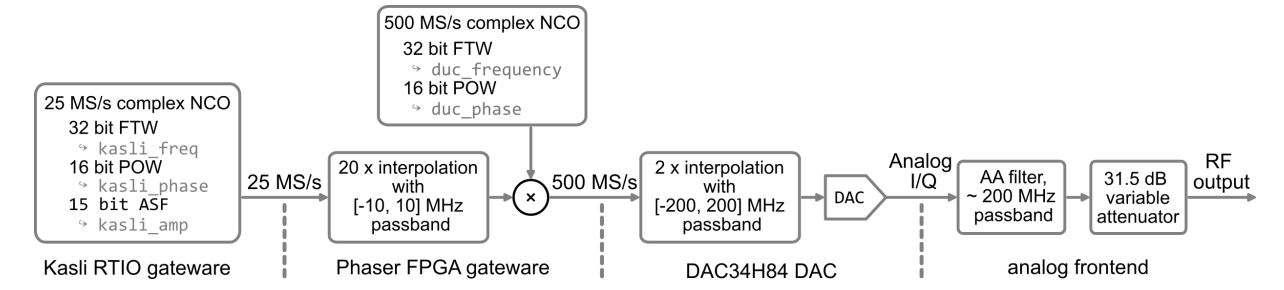


Figure 5.1.: Relevant signal processing pipeline for the Phaser module, with the physical location of each processing step indicated at the bottom. The grey font indicates parameters, that are modified by the software implementation of a standard as well as an ms\_am gate. The figure is taken from Ref. 59 and adapted to show only the relevant parts, with the measured passband frequency range of the AA filter taken from Ref. 58.

## 5.2. Phaser device characteristics

The Phaser hardware module enables in principle the simultaneous modulation of phase, frequency, and amplitude. In practice however, the signal processing pipeline outlined in the previous Sec. 5.1 imposes constraints to the parameter update time as well as to parameter changes. A DP-AOM unit was used to investigate how changes in the phase and amplitude are imprinted on the laser beam intensity with a photodiode (PD) to determine which modulation technique to pursue in the AQTION setup. For these tests the quench laser with a wavelength of 866 nm was used instead of the qubit laser with a wavelength of 729 nm, but the main results should still apply to the qubit laser wavelength. The kasli\_freq = 197.25 MHz was set such that the qubit transition  $|0\rangle = |4^2S_{1/2}, m_j = -1/2\rangle \leftrightarrow |1\rangle = |3^2D_{5/2}, m_j = -1/2\rangle$  would be driven in an experiment. Frequency modulation is intentionally excluded from all considerations in this thesis as it would additionally require the implementation and calibration of phase tracking in the control software.

First, discrete changes in the RF amplitude and their influence on the laser beam intensity were investigated. For this, a 5 µs rectangular RF pulse was sent to a DP-AOM whose kasli\_amp was varied between 30 % and 100 % of the maximum value, while the frequency and phase of the RF pulse remained constant. The corresponding PD signal is depicted in Fig. 5.2a, with the numbers indicating the kasli\_amp for the respective colored trace. For large amplitude values of the rectangular signal (80 % and above), one can observe the sinc-like overshoot behaviour of the digital interpolation filter arising from the near brick-wall frequency response of the filter [60]. This overshoot can be observed on both edges of the pulse.

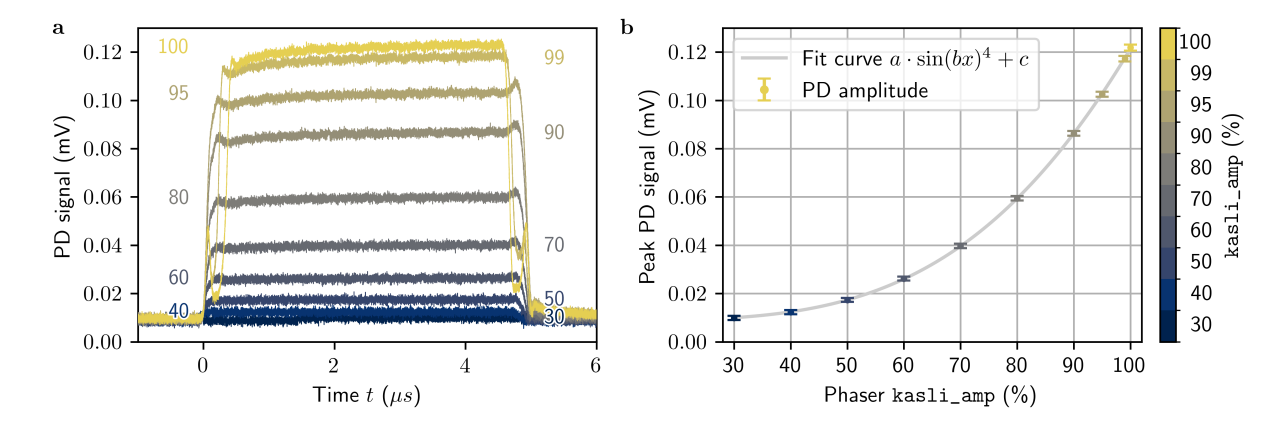


Figure 5.2.: a, Rectangular signal of 5 µs length for different kasli\_amp ASFs, with t = 0 µs indicating the beginning of the rising slope. b, Peak PD signal intensity (without overshoots) of the signals in a. Fitted is a function of the form  $a \sin(bx)^4 + c$  to illustrate the dependence of the light intensity on the amplitude that is specified in the RF generation.

In addition to an observed overshoot of the PD signal amplitude, oscillations in the rising and falling edges of the rectangular pulse can be observed for the largest two values of the kasli\_amp of 99 % and 100 %. This is the result of overflow occurring in the signal processing pipeline for changes in the amplitude that are close to 100 %. Both behaviours can be minimized by choosing smaller changes in the amplitude. Furthermore, the transient response of the AOMs can be seen by noting the slope of the signal for  $t \in [0,5]$  µs, especially for larger amplitudes. Note that this is a feature of the AOMs rather than a feature that is introduced by the RF generation of Phaser.

In Fig. 5.2b, the peak PD signal is shown as a function of the chosen kasli\_amp. It was extracted from the PD signal for the time interval  $t \in [1 \, \mu s, 4 \, \mu s]$  to exclude the overshooting behaviour for certain amplitudes. The error bars correspond to the standard deviation in these time intervals. For a DP-AOM, the expected relationship between the peak PD signal  $A_p$  and the kasli\_amp  $A_k$  is given by

$$A_{\mathbf{p}}(A_{\mathbf{k}}) = a \cdot \sin(bA_{\mathbf{k}})^4 + c, \tag{5.1}$$

with amplitude a, frequency b, and offset of the PD signal due to background illumination c. A fit to the data points clearly shows this expected dependence of the peak PD signal.

Second, to investigate the feasibility of phase modulation, a constant kasli\_amp = 95 % is set, while the kasli\_phase is repeatedly varied between 0 rad and the interval  $[0.04, 1] \pi$  rad. The PD signal for both signs of the phase change  $0 \to \text{kasli_phase}$  and kasli\_phase  $\to 0$  is shown in Fig. 5.3a. Although the amplitude is not changed in these measurements, there is a visible change in the PD signal arising from the digital signal processing pipeline of the Phaser module. The minimum PD signal was obtained for 30 subsequent changes in the phase and grouped by

the sign of the phase change to quantify this effect. From this, the reduction of the PD signal relative to the constant PD signal for kasli\_amp = 95 % was calculated. Additionally, the offset of the PD signal due to background illumination visible in Fig. 5.2 is taken into account. The mean and standard deviation over 15 phase changes is shown in Fig. 5.3b, with the error bars being smaller than the extent of the individual squares and circles representing the data points. Changes in the phase that are larger than  $0.4\,\pi$  rad results in at least 80 % reduction of the PD signal. For smaller changes there is less reduction of the PD signal, with the minimum observed reduction being equal to 20 % for a phase change of  $0.04\,\pi$  rad =  $7.2^{\circ}$ .

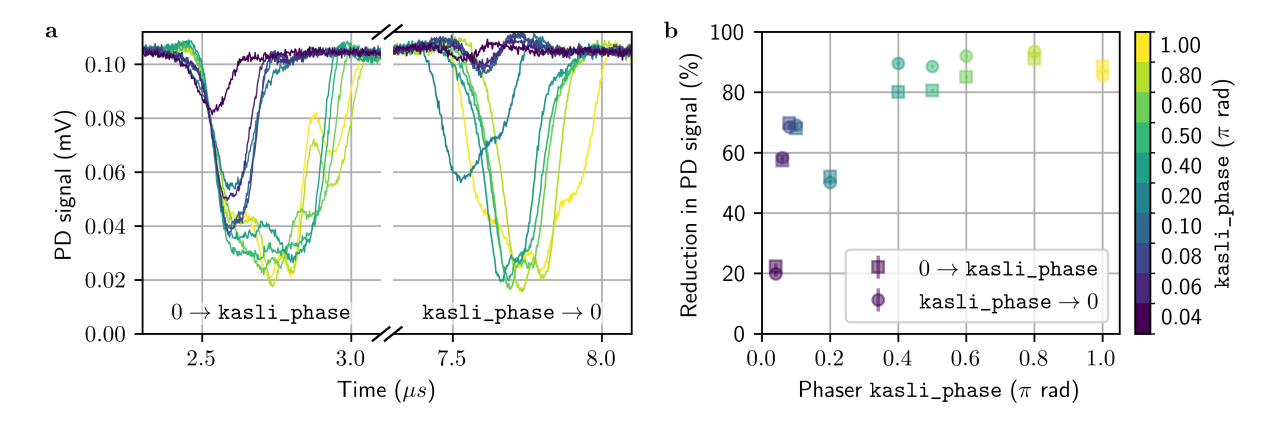


Figure 5.3.: a, For a constant kasli\_amp = 95 % set on a single channel of the Phaser module, both positive and negative changes in the phase result in a reduction of the PD signal. b, The reduction of the PD signal relative to the PD signal for kasli\_amp = 95 % is calculated for different values of the kasli\_phase for a total of 15 phase changes. The offset of the PD signal is thereby taken into account and was taken from Fig. 5.2.

One has to keep in mind that phase modulation would be carried out on a single channel of the FAOM instead of the DP-AOM, which means that the reduction in laser intensity in the experiment would be smaller than the ones shown in Fig. 5.3. Regardless of this, even a reduction of 20 % in the PD signal would result in a controlled and desired modulation of the phase accompanied by an uncontrolled modulation of the amplitude. As the modulation of the amplitude would only affect one of the two frequency tones required for the creation of the bichromatic laser beam, this results in a time-dependent imbalance of the power among the two tones. This imbalance introduces a time-dependent AC-Stark shift, which for modulation sequences requiring multiple phase changes during the gate operation will inevitably lead to a drop in the gate fidelity when uncorrected.

Third, the capabilities of Phaser regarding parameter update times were investigated, as this time determines the maximum number of segments one can realize for a given modulation scheme. Continuous functions of frequency, phase, and amplitude in time are approximated by updating them in discrete time steps, because a single channel of Phaser is limited to 5 tones with unique values for those parameters. Therefore smaller update times are more favourable to more closely approximate the desired waveform. The time it takes for a single parameter update of the amplitude or the phase can be as low as  $\approx 1$  µs before an underflow error occurs. For lower times, an RTIO event of the parameter change would be placed in the past relative to the wall clock. This would break the guarantee of the time-critical code execution and hence the program is interrupted. More details about the ARTIQ RTIO concepts are provided in Ref. 61. This lower

time was obtained in a minimal working example, where the kasli\_amp ASFs or kasli\_phase POWs are continuously varied between two values. This means that only the task of switching between those values for a single Phaser channel was realized in the program instead of having a full experimental control software running. Hence the time can be regarded as a lower limit to what one can expect in the experiment. The lower limit for simultaneously changing both the phase and the amplitude was measured to be  $\approx 2\,\mu\text{s}$ , regardless of the magnitude of change. However, one can further reduce these times by utilizing the Direct Memory Access (DMA) feature of ARTIQ.

This features allows the recording of RTIO events that implement a desired waveform and storing them on the FPGAs Synchronous Dynamic Random-Access Memory (SDRAM) on the Sinara Kasli module. Instead of having to compute the RTIO events when a kernel function is called, the saved RTIO events are simply fetched from the SDRAM and played back by the FPGA core on the Kasli module. Using this method, the change of either the phase or amplitude can be reduced to 275 ns before an underflow error occurs. Given that a typical MS gate takes 300 µs, this would correspond to more than a 1000 individual parameter updates.

An example of a Gaussian waveform with a parameter update time of 275 ns is depicted in Fig. 5.4a, where both the RF signal as well as the resulting PD signal after the DP-AOM are shown. The chosen parameters, a gate time of  $\tau=200\,\mathrm{ps}$  and a width of the Gaussian waveform of  $\sigma=25\,\mathrm{ps}$ , are both reflected in the RF signal. Note that the time is relative to the peak of the RF signal and the RF signal outside  $\pm100\,\mathrm{ps}$  is set to zero. In these regions, the resolution of the Analog-to-Digital Converter of the oscilloscope as well as background noise are visible. Given the parameter update time, more than 700 updates of the amplitude are performed within the gate time, enough to approximate the Gaussian waveform to a sufficient degree for experimental purposes.

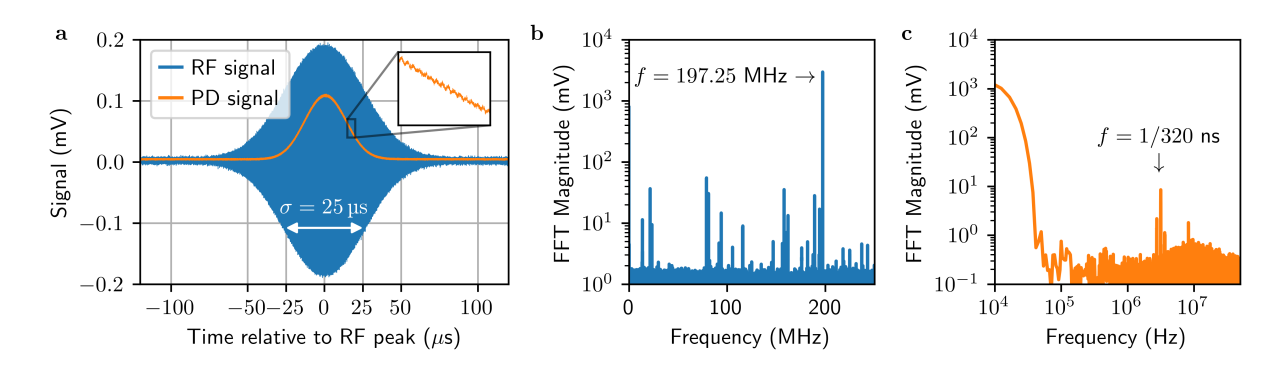


Figure 5.4.: a, RF signal of a Gaussian waveform realized on the Phaser with a parameter update time of 275 ns and a Gaussian width of  $\sigma=25\,\mathrm{ps}$  (blue) with the corresponding PD signal (orange). The width of the PD signal is smaller compared to the RF signal due to the  $\sim\sin^4$  dependence of the light intensity on the amplitude of the RF signal following Eq. 5.1 and experimentally shown in Fig. 5.2b. Oscillations of the PD are shown in the inset. b, FFT of the RF signal, showing the carrier at  $f=197.25\,\mathrm{MHz}$ . c, FFT of the PD signal, showing only the envelope of the signal. The main frequency components are below  $100\,\mathrm{kHz}$ , indicating the spectrally compact Gaussian waveform. Additional peaks arise due to aliasing from Phaser and the impact is discussed in Chap. 7.

Figure 5.4b shows the Fast Fourier transform (FFT) of the RF signal, with the main peak located at a frequency of f = 197.25 MHz, which is expected given the chosen RF parameters. In Fig. 5.4c, the FFT of the PD signal only shows the information present in the envelope of the signal, as

### 5. Characterization of the ARTIQ and Sinara ecosystem

the carrier frequency of the laser beam on the order of THz is outside the bandwidth of the PD. The main frequency components are below  $100\,\mathrm{kHz}$ , indicating the spectrally compact Fourier Transform of a Gaussian waveform. Additional peaks are located at  $f=1/320\,\mathrm{ns}=3.125\,\mathrm{MHz}$  and at  $3.6\,\mathrm{MHz}$ , coming from aliasing in the Phaser gateware when the signal is resampled from  $275\,\mathrm{ns}$  to  $320\,\mathrm{ns}$ . This effect is discussed in more detail in the outlook in Sec. 7.

The conclusion of this chapter is, that an amplitude-modulated MS scheme may be the most promising optimal control technique given the technical capabilities of Phaser, as phase changes lead to undesired changes of the amplitude of the signal. Furthermore, by using the built-in DMA feature the update times for single parameter changes can be expected to be on the order of 300 ns when embedded into the experimental control software. This time should be fast enough to approximate continuous changes of parameters, as shown for the example of a Gaussian waveform.

# 6. Experimental results

The following chapter presents experimental results from the AQTION machine obtained between October 2024 and January 2025. Numerical "phase space" simulations following Chap. 4 aid the parameter choice for the implemented  $ms_am$  gate and are shown alongside experimental findings. The chapter is divided into two parts, beginning with the results for a 2-ion chain in Sec. 6.1. Here, the dependence of the Rabi frequency  $\Omega$  on the Phaser  $kasli_amp$  is determined, which allows the generation of a Gaussian waveform in Rabi frequency  $\Omega$ . Using these results, the performance of the gate is measured by using the state preparation fidelity of a maximally entangled state as an estimate for the gate fidelity. We investigate the state preparation fidelity as a function of the number of gates and examine its robustness against motional mode frequency drifts. In the second part of the chapter, the ion chain is extended to 16 ions, leading to an increase in the number of ion pair combinations  $j_1-j_2$  from 1 to 120. Hence the main focus of Sec. 6.2 lies on a calibration technique that allows the time-efficient calibration of all 120 individual gates. We then compare the  $ms_am$  gate to the standard MS gate for all 120 pairs using the state preparation fidelity of maximally entangled states as a measure.

## 6.1. Experimental results for a 2-ion chain

In this section, the ms\_am gate is tested on a 2-ion chain with radial COM mode frequencies  $f_{\rm COM,\,x}=3097.6\,{\rm kHz}$  and  $f_{\rm COM,\,y}=3177.0\,{\rm kHz}$  as well as an effective axial COM mode frequency  $f_{\rm COM,\,z}=846.0\,{\rm kHz}$ . The numerical optimization results for the ms\_am gate, as described in Sec. 4.3, are shown in Fig. 4.7 for a gate time of 300 µs and a Gaussian width of  $\sigma=50\,{\rm µs}$ . In total, seven balance-point detunings have been found numerically, with only one solution satisfying both conditions  $\Omega_0/(2\pi)>400\,{\rm kHz}$  and  $\bar{\mathcal{F}}>99\,\%$  at the same time. This particular solution has a balance-point detuning of  $\delta_{\rm c}=3.080\,{\rm kHz}$ , with the bichromatic frequency components located between target modes k=2 and k=3. The simulated peak Rabi frequency for achieving a maximally entangled state is  $\Omega_0/(2\pi)=165.28\,{\rm kHz}$ .

As outlined in Sec. 4.2, amplitude modulation is carried out by varying the carrier Rabi frequency  $\Omega$  of the addressed ion pair. In the experiment however, the Phaser kasli\_amp ASF and thus the RF output amplitude is varied. This necessitates a mapping from the kasli\_amp  $A_k$  to the Rabi frequency  $\Omega$ . As the output of Phaser is connected to a DP-AOM, the expected dependence is of the form  $\Omega(A_k) = a \sin(bA_k)^2$ , with amplitude a and angular frequency b. This relationship is shown in Fig. 6.1, where a single ion was resonantly addressed to obtain the carrier Rabi frequency  $\Omega$  defining the entangling gate operation. The data shown here is obtained by addressing ion j=1 and the results similarly apply also to ion j=2, given that the variation in laser intensity incident on the ions is smaller than the typical experimental drift. Note that throughout the measurement, the amplitude of the RF signals which are supplied to the FAOM

<sup>&</sup>lt;sup>1</sup>For a single AOM the dependence of the intensity I on the input amplitude  $A_k$  is  $I \sim \sin(A_k)^2$  and for a DP-AOM  $I \sim \sin(A_k)^4$ . With the relation  $I \sim \Omega^2$  one arrives at the mentioned dependence.

and the addressed AODs remained constant at their typical operational value. In order to realize a Gaussian waveform in Rabi frequency, the kasli\_amp is calculated using the inverse relation  $A_k(\Omega(t)) = \arcsin\left(\sqrt{\Omega(t)/a}\right)/b$ , with  $\Omega(t)$  the time-dependent Rabi frequency following a Gaussian function from Eq. 4.2. The non-linearity of the DP-AOM causes a reduction of the pulse area on the laser beam compared to the RF signal, which is shown for a Gaussian waveform in Fig. 5.4 for the intensity ( $\sim \sin^4$ ) instead of the Rabi frequency ( $\sim \sin^2$ ) that is investigated here. By using the mapping, the desired waveform is implemented in Rabi frequency instead of in the RF signal, which increases the pulse area while simultaneously reducing the required power to implement an ms\_am gate. This ensures that the DP-AOM operates in the linear regime visible in Fig. 6.1 and that the implemented waveform also more accurately reproduces the desired Gaussian waveform in Rabi frequency underlying numerical simulations.

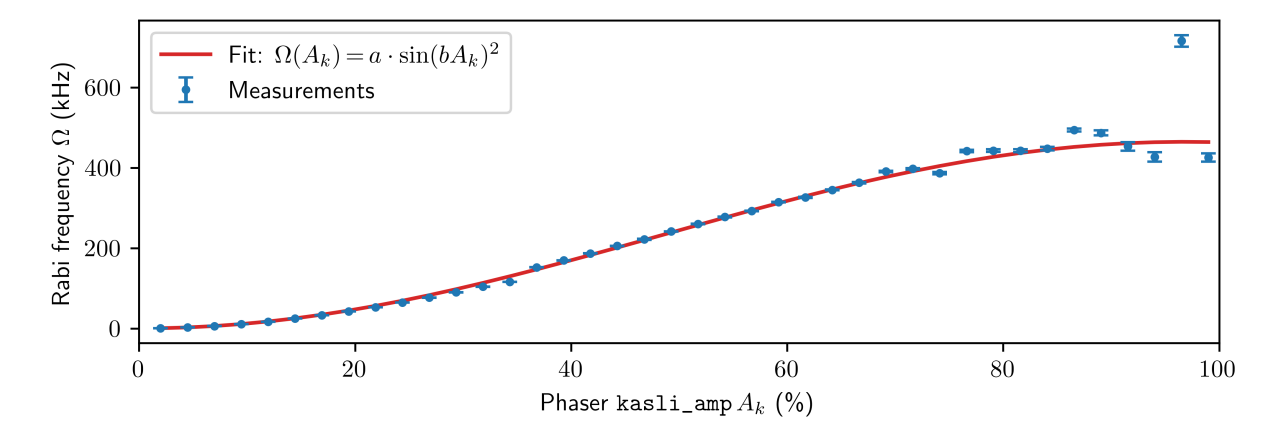


Figure 6.1.: Rabi frequency  $\Omega$  as a function of the Phaser kasli\_amp for addressing a single ion in a 2-ion chain. The fit shows the expected dependence due to the DP-AOM  $\Omega(A_k) = a \cdot \sin(bA_k)^2$  and is shown in red with parameters a and b. A Gaussian waveform in Rabi frequency  $\Omega(t)$  can be realized by solving the function for  $A_k(\Omega(t))$ .

With this mapping established, the next step is to measure the state preparation fidelity of the maximally entangled state  $(|00\rangle+i|11\rangle)/\sqrt{2}$  when starting in  $|00\rangle$ . The first measurement is shown in Fig. 6.2a and is a detuning scan for the standard MS gate around the ideal detuning of  $\delta=1/304\,\mathrm{\mu s}$  relative to the radial-y COM mode. Here, the population of the odd states  $|01\rangle+|10\rangle$ , where the phonon number is changed<sup>2</sup>, is suppressed in a  $\approx 1\,\mathrm{kHz}$  wide region around the ideal detuning. For the ms\_am gate, the same scan was carried out but this time the detuning was varied in between the target modes around the balance-point detuning of  $\delta=-97.1\,\mathrm{kHz}$ . The required peak Rabi frequency  $\Omega_0$  for this scan was chosen such that an ms\_am gate is implemented at the balance-point detuning, with the results shown in Fig. 6.2b. The region where the odd state population is suppressed is  $\approx 20\,\mathrm{kHz}$  wide for the ms\_am gate and thus larger compared to the standard MS gate when using a gate time of 300 µs for both implementations.

A robustness scan was carried out in a second step, as the detuning scan only gives an indication about the displacement error induced by the gate operation, but not on the state preparation fidelity  $\mathcal{F}$ . The idea here is to investigate the robustness of the state preparation fidelity against motional mode frequency changes, but instead of changing the applied trapping frequencies for each scan point the detuning is shifted to mimic this effect. The power of the respective gate

<sup>&</sup>lt;sup>2</sup>The odd state population also includes the effect of resonant carrier excitation. This contribution is however much smaller given that the population of odd states is significantly reduced at the ideal detuning.

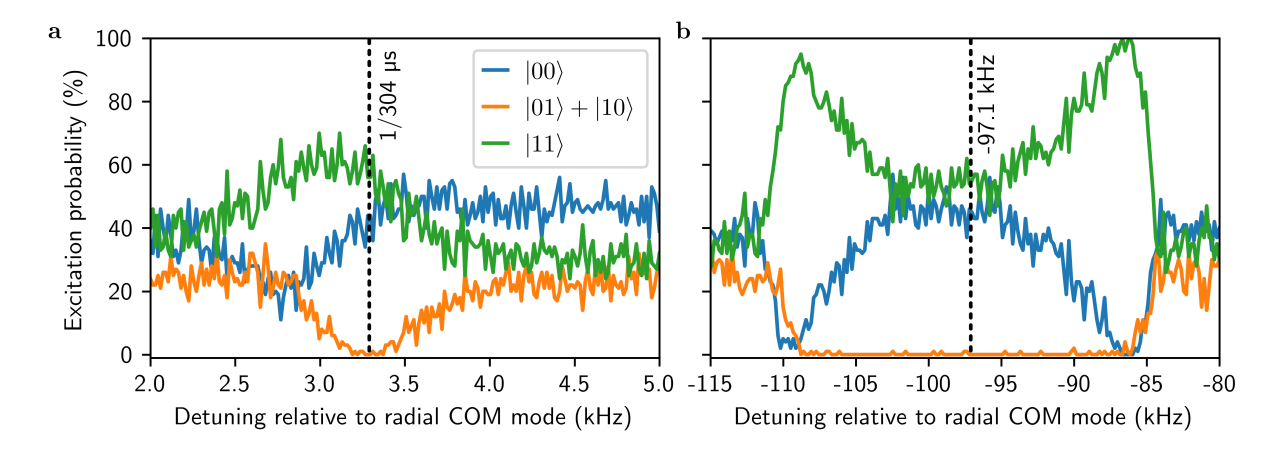


Figure 6.2.: Detuning scan for the standard MS gate shown in **a** and for the ms\_am gate in **b**, with different scales on the x-axis. The ideal detuning was chosen based on experimental measurements for the MS gate ( $\delta = 1/304 \, \mu s$ ) and for the ms\_am gate based on numerical simulations ( $\delta = -97.1 \, \text{kHz}$ ).

was calibrated at the ideal detuning (for the MS gate  $\delta=1/304\,\mu s$  and for the ms\_am gate  $\delta=-97.1\,\mathrm{kHz}$ ) and the state preparation fidelity is obtained for a different detuning using this calibrated power. The result for the standard MS gate can be seen in Fig. 6.3a, showing a  $\approx 800\,\mathrm{Hz}$  wide region where the condition  $\mathcal{F}>90\,\%$  holds. The discrepancy between the ideal detuning and the maximum fidelity obtained by the simulation may be explained by the fact that the simulation doesn't take amplitude shaping into account. For the ms\_am gate in Fig. 6.3b, this region is  $\approx 20\,\mathrm{kHz}$  wide, reinforcing the results obtained from the detuning scan showing a larger region where the population of odd states is suppressed compared to the standard MS gate.

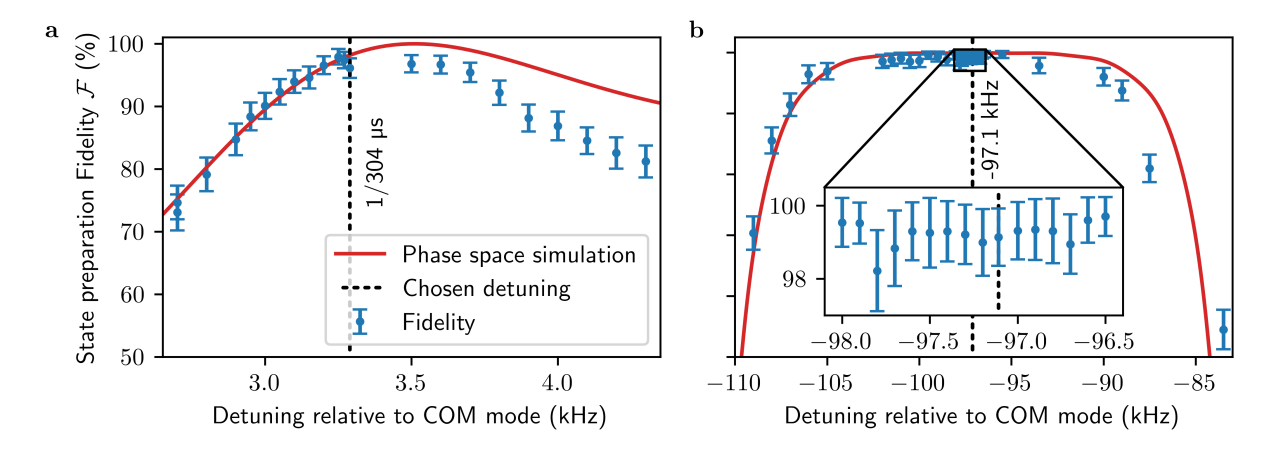


Figure 6.3.: a, Robustness scan for the standard MS gate at a detuning  $\delta = 1/304\,\mu s$ . b, Robustness scan for the ms\_am gate around the ideally chosen detuning  $\delta = -97.109\,\text{kHz}$  between the center target modes, indicating a broad region with  $\mathcal{F} > 90\,\%$ . The region where high-fidelity gates are obtained is larger compared to the standard MS gate.

However, the motional mode frequencies usually vary by only  $\pm 250\,\mathrm{Hz}$  around the ideal detuning in continuous operation, minimizing the potential advantage of the ms\_am gate. The relevant region for the ms\_am gate is shown by the inset in Fig. 6.3b, where no dependence of the state preparation fidelity is visible compared the same region for the standard MS gate. In both cases,

the red curve shows the average gate fidelity  $\bar{\mathcal{F}}$  estimated by phase space simulation, which is in agreement with the measured data towards the left of the ideal detuning, but deviates more strongly towards the right of it. Measurements were obtained left first, right afterwards with a calibration of the required power for the entangling gate before each scan point at the ideal detuning. However no other calibration scripts were run, possible resulting in an accumulation of parameter drifts increasing in severity towards the right.

Next, the state preparation fidelity for both the standard MS and the ms\_am gate is obtained for different numbers of consecutive gates  $n_g$ . Prior to each measurement point, the power of  $n_g$  consecutive gates is calibrated with a power scan, with the detuning held constant for all measurements. From these measurements, an error rate  $\varepsilon$  can be extracted by fitting the function  $\mathcal{F}(n_g) = (1-\varepsilon)^{n_g}$ , which is shown in Fig. 6.4a for the MS gate and in Fig. 6.4b for the ms\_am gate. Given that the state preparation and measurement (SPAM) error was measured separately to be well below the resolution of this measurement, a single-parameter fidelity decay model was chosen that does not include SPAM errors. The result for the standard MS gate is  $\varepsilon_{\rm MS} = 0.73(10)\,\%$  and for the ms\_am gate  $\varepsilon_{\rm ms_am} = 0.31(3)\,\%$ .

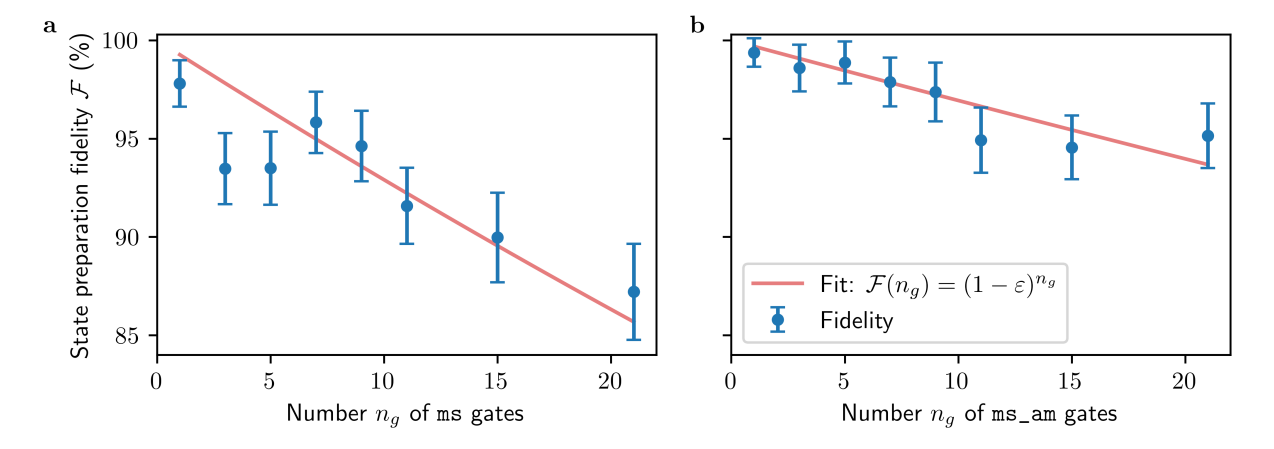


Figure 6.4.: Measured error rates  $\varepsilon$  for entangling gates with a gate time of  $\tau = 300 \,\mu s$ . a, Error rate for the standard MS gate with a detuning of  $\delta = 1/304 \,\mu s$  relative to the radial-y COM mode. b, Error rate for the ms\_am gate with a detuning of  $\delta = -97.1 \,\text{kHz}$  and a Gaussian width of  $\sigma = 50 \,\mu s$ .

During the system migration to the Sinara hardware ecosystem, a calibration error was introduced by assuming that the gate time for the standard MS gate should stay at the previously optimal  $\tau=300\,\mu s$ . Although the detuning was optimized for this gate time, we will see in the following section with 16 ions that the gate performance can be increased by choosing a longer gate time while keeping the detuning the same. Consequently, the results in this section only imply that the ms\_am gate worked and performed at least as well as the standard MS gate.

## 6.2. Experimental results for a 16-ion chain

In this chapter the ion chain is extended from 2 to 16 ions, which is the typical ion number used in the AQTION setup. Not only does the number of radial modes grow from 4 to 32, but also the number of distinct pairs that need to be calibrated expands from a single pair to 120 pairs in the 16-ion chain. This section is thus mainly devoted to an experimental calibration procedure that

achieves the calibration of all 120 pairs in a time-efficient manner, with the procedure described in the first part of this section. The second part then presents experimental results comparing the standard MS gate with the ms\_am gate with regard to their state preparation fidelity of maximally entangled states.

The experimental parameters of the individual ms\_am gates are based on the numerical simulation outlined in Sec. 4.3. For this whole section the input parameters of the simulation are the number of ions  $n_{\rm ions}=16$ , both radial COM mode frequencies  $f_{\rm COM,\,x}=3095.36\,{\rm kHz}$  and  $f_{\rm COM,\,y}=3177.00\,{\rm kHz}$  in addition to the effective axial COM mode frequency  $f_{\rm COM,\,z}=383.20\,{\rm kHz}$ . The gate time  $\tau=300\,{\rm ps}$  was chosen such that a direct comparison with the standard MS gate is possible, whereas the width  $\sigma=59\,{\rm ps}$  balances the power requirements in the experiment with the number of numerically obtained high-fidelity solutions exceeding  $\bar{\mathcal{F}}>99\,\%$ . Given the symmetry of the LD factors with respect to the ion indices  $j_1$  and  $j_2$ , only 64 out of the 120 pairs need to be simulated, as the ion pair  $j_1-j_2$  yields the same set of solutions as pair  $(17-j_2)-(17-j_1)$ . The obtained results need to be filtered further, as for each ion pair there exist multiple viable balance-point detunings leading to a high-fidelity ms\_am gate implementation.

Out of 6909 obtained solutions<sup>3</sup>, 120 possible combinations (that is one per unique ion pair) have been obtained by considering for a given ion pair only solutions with a fidelity  $\bar{\mathcal{F}} > 99\%$  and choosing the solution with the lowest peak Rabi frequency  $\Omega_0$ . All 120 solutions and their properties can be seen in Fig. 6.5, broken down in the rows of the figure by peak Rabi frequency  $\Omega_0/(2\pi)$ , balance-point detuning  $\delta_c/(2\pi)$  and gate fidelity  $\bar{\mathcal{F}}$ .

In Fig. 6.5a and b the distribution of required peak Rabi frequencies  $\Omega_0/(2\pi)$  for all 120 addressed ion pairs is shown. The minimum (maximum) Rabi frequency is required for pair(s) 4-13 (2-10 and 7-15) with  $\Omega_0/(2\pi) = 163 \,\mathrm{kHz} \,(432 \,\mathrm{kHz})$ , with the mean over all pairs being 305 kHz. In general, ion pair combinations that address an ion at the outer edge of the chain require higher Rabi frequencies as the LD factor is usually lower for these ions for the given target modes used in the gate operation. The balance-point detuning  $\delta_c/(2\pi)$  is shown in Fig. 6.5c and d, with the radial-x and -y motional mode frequencies illustrated at the top of c to indicate the respective target modes of the gate operation.

Note that solutions shown here realize an ms\_am gate with both entangling phases  $\Phi=\pm\pi/2$ , with the sign depending on the balance-point detuning and target modes. This is in contrast to the standard MS gate, where the bichromatic laser beam frequency is always positioned outside the mode spectrum ensuring the same entangling phase for all ion pairs. Having both signs of the entangling phase is however undesired in operation and adds unnecessary complexity to quantum circuit designs, hence it was decided that only positive entangling phases should be realized experimentally. This is done by correcting solutions with a negative entangling phase using the relation

$$MS(+\pi/2) = (R_z(\pi) \otimes \mathbb{1}_2)MS(-\pi/2)(R_z(\pi) \otimes \mathbb{1}_2)$$

$$(6.1)$$

by applying virtual z-rotations  $R_z(\pi) = \sigma_z$  on one of the two addressed ions. One could also restrict the solutions from numerical simulation to negative entangling phases, which comes with the disadvantage that the mean Rabi frequency would increase from 305 kHz to 345 kHz. Constraining the solutions to have only positive entangling phases would, for a width of  $\sigma = 59 \,\mu s$ , not give a solution with  $\bar{\mathcal{F}} > 99 \,\%$  for all ion pairs. The simulated fidelity  $\bar{\mathcal{F}}$  is shown in Fig. 6.5e

<sup>&</sup>lt;sup>3</sup>The numerical simulation for 64 out of 120 pairs yields 3699 solutions. As the solutions for ion pair  $j_1 - j_2$  are the same as for pair  $(17 - j_2) - (17 - j_1)$  due to the symmetry of the LD factors (equals 3210 solutions for 56 of the 64 simulated pairs), the actual number of solutions is calculated to  $489 + 2 \cdot 3210 = 6909$ .

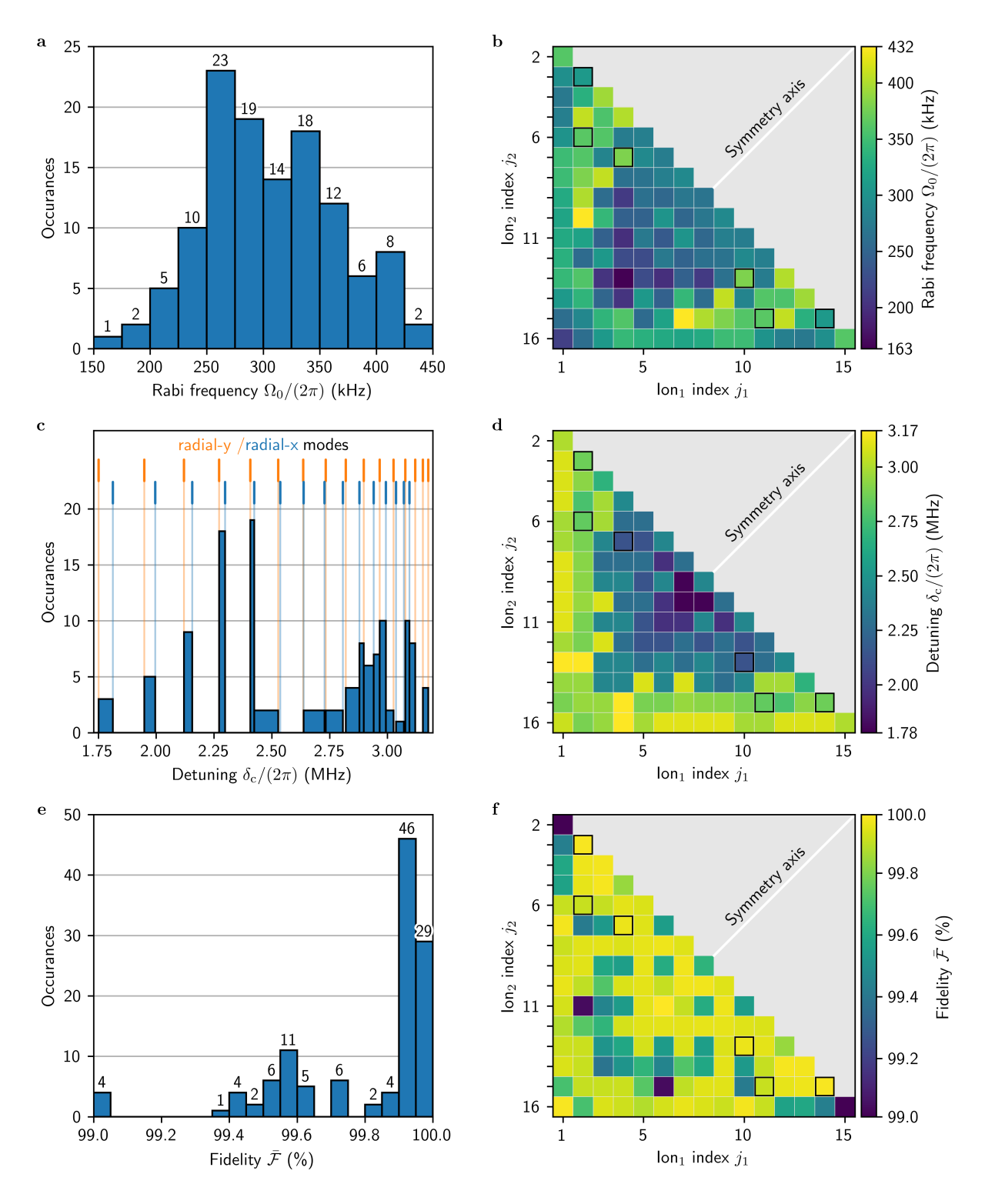


Figure 6.5.: Selected result for each ion pair from numerical simulation, with results around the symmetry axis being the same for ion indices  $j_1$  and  $j_2$  and  $(17-j_2)-(17-j_1)$ . a and b show the peak Rabi frequency  $\Omega_0/(2\pi)$ , c and d the balance-point detuning  $\delta_c/(2\pi)$ , with the radial-x and -y mode frequencies shown in c for reference. The average gate fidelity  $\bar{\mathcal{F}}$  is shown in e and f, with the minimum and maximum value of the respective quantity reflected in the colorbar of each row. For six ion pairs that are emphasized with black rectangles, the values shown here have been changed compared to the results obtained from numerical simulation, with the changes discussed in the main text.

#### 6. Experimental results

and **f**, with a mean of 99.8(2) %. The majority of solutions are above 99.9 %, with notable outliers being ion pairs 1-2 and 2-11 (by symmetry also 15-16 and 6-16) with an average gate fidelity of 99 %. The lower simulated fidelity for certain ion pairs arises from the fixed combination of gate time and width of the Gaussian waveform given the experimental mode spectrum. Simulation results suggest that relaxing this constraint would result in higher simulated fidelities without having to extend the gate time significantly. No clear dependence of the fidelity on the ion pair has been found.

After having identified a set  $\{\Omega_0, \delta_c\}$  for each ion pair, the next step is to devise a calibration method based on experimental detuning and power scans following Sec. 4.4. The naive approach would be to regularly carry out 240 separate scans using the numerical solution as a starting point. However this would take in excess of 40 min (with a single scan lasting for more than 10 s), making this approach infeasible for a target calibration interval of 30 min or less. Instead we can leverage the demonstrated robustness of the ms\_am gate against motional mode frequency changes shown in Fig. 6.3b. It was found that simply using the numerically pre-determined balance-point detuning results in high-fidelity gate operations for all but six ion pairs, which are emphasized with black rectangles in the right column of Fig. 6.5. For ion pairs 1-2 and 13-14, odd state population was found to be unacceptable high at the expected balance-point detuning, which most probable comes from sum-frequency terms of the bichromatic frequencies with the compensation tone frequency resonantly exciting either the carrier transition or motional sideband transitions. In this case the detuning was adjusted from  $\delta_c/(2\pi) = 2.849711 \,\mathrm{MHz}$  to  $2.858000 \,\mathrm{MHz}$  and the required Rabi frequency as well as fidelity have been calculated for this new value in Fig. 6.5. The same reason applies to ion pairs 1-5 and 10-14, where the detuning was changed by 10 kHz from  $\delta_c/(2\pi) = 2.845\,282\,\mathrm{MHz}$  to  $2.835\,282\,\mathrm{MHz}$ . Furthermore, the fidelity for ion pairs 3-6 and 9-12 was below expectation, with the underlying reason still unknown. This problem was simply circumvented by choosing another one of the available balance-point detunings, which increased the required Rabi frequency from 225 kHz to 380 kHz but yielded the expected result.

Given that scanning the power of 120 ion pairs would still be too time-consuming during normal operation, efforts were made to reduce the calibration to a single power scan. The idea here is to first obtain the required power (or more specifically the required Phaser kasli\_amp that in turn determines the power) for all 120 pairs with pair-specific power scans once. Pair-specific in this context refers to the scan range of the power scan, as the required power for different ion pairs varies by roughly 40% of the kasli\_amp. This is in contrast to the standard MS gate, where the power for all pairs is confined to the range kasli\_amp  $\in$  [42.6, 46.0] %, owing to the fact that the main contribution always comes from the radial-y COM mode. The results of this power scan for the ms\_am gate are depicted in Fig. 6.6a, where the peak kasli\_amp  $A_c$  is shown as a function of the simulated peak Rabi frequency  $\Omega_0/(2\pi)$ . A linear fit shows that the simulation gives a reasonable estimate for the expected power, with the absolute value of the residuals for each ion pair shown in Fig. 6.6b. However, the simulation does not account for various experimental factors, like different Rabi frequencies on the two target ions or optical crosstalk on non-target ions, which are reflected in the power scans. Nonetheless the estimate coming from simulation can be used to narrow down the scan region of the power scan even further, which was conservatively chosen to obtain the results shown in Fig. 6.6.

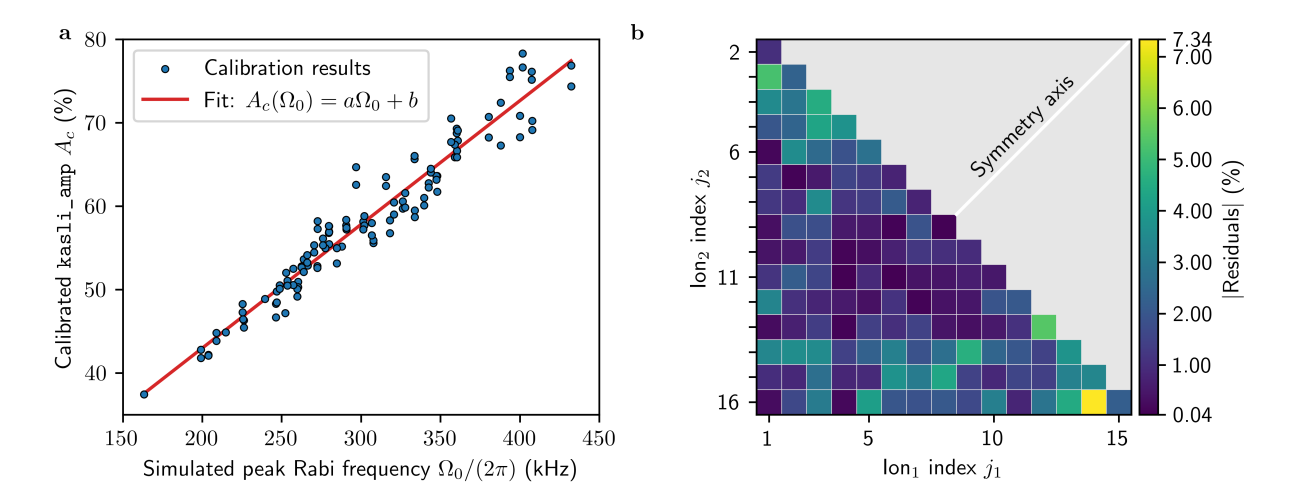


**Figure 6.6.:** a, Power calibration results for all 120 ion pairs using the balance-point detunings from the numerical simulation in Fig. 6.5. No error bar is shown as these results are used for calibration and the red line shows a linear fit between numerical simulation and experimental calibration data. **b**, Residuals for each ion pair, indicating unaccounted for experimental factors leading to deviations from the simulation.

The calibrated amplitude for each ion pair is then saved in a matrix  $A_{\text{ref}}(j_1, j_2)$  and the ion pair 1-5 was chosen to act as a reference pair. Instead of scanning 120 pairs, only the power for this pair is calibrated, with the resulting kasli\_amp  $A_C(1,5)$  used to update the amplitude of all other ion pairs with

$$A_C(j_1, j_2) = A_C(1, 5) \cdot \frac{A_{\text{ref}}(j_1, j_2)}{A_{\text{ref}}(1, 5)}.$$
 (6.2)

For the standard MS gate, the same calibration procedure is used with the reference pair being 1-2. The resulting state preparation fidelity  $\mathcal{F}$ , averaged over 5 runs per ion pair, is shown in Fig. 6.7a for the standard MS gate and in Fig. 6.7b for the ms\_am gate, where the mean over 8 runs was calculated. Both subplots share a common colorbar scale, with the minimum and maximum state preparation fidelity indicated in each respective colorbar for the corresponding gate implementation. A histogram is shown in Fig. 6.7c along with the mean value over all ion pairs to facilitate comparison between the two methods. As the distributions is asymmetric, the uncertainty is calculated using the 68 % quantile centered around the median value. As a result, the mean state preparation fidelity for the standard MS gate is  $97.90^{+0.52}_{-0.47}\%$  and for the ms\_am gate  $98.48^{+0.48}_{-0.47}\%$ .

The  $\approx 0.6\,\%$  difference between them is consistent with simulation results from Fig. 4.4, although the absolute values deviate from the simulation. The main reasons for this discrepancy include the calibration procedure itself and the errors introduced during state preparation  $(0.3\,\%)$ , single qubit gates required for the parity scans  $(0.36\,\%)$ , and measurement  $(0.3\,\%)$ , with error probabilities in brackets from Ref. 62. However, these are separately measured error probabilities and further investigations are required to quantify the exact contribution of each factor to the observed state preparation fidelity.

Note that in total 4 out of 1560 scans have been discarded for this analysis (1/600 for the MS gate and 3/960 for the ms\_am gate), as in these scans the population of non-addressed ions exceeded 10%. This behaviour is most likely explained by the generation of higher diffraction orders when applying two frequency tones to the addressing unit. While the first diffraction

### 6. Experimental results

orders create optical beam spots with no frequency shift and their spatial position aligned to the ions, the mixing with higher order diffraction terms leads to off-resonant spots that are displaced from the ion positions. For certain combinations of addressing frequencies, the frequency of those spots is resonant with a carrier transition. Due to the fact that entangling operations are driven with far more power than resonant single-qubit operations would require, multiple ions are excited, resulting in the described behaviour. A strong indication for this explanation is that this behaviour could be turned on and off by changing the addressing frequencies by  $\approx 10\,\mathrm{kHz}$ . As such, it is justified to discard those scans as the result does not reflect the performance of the gate.

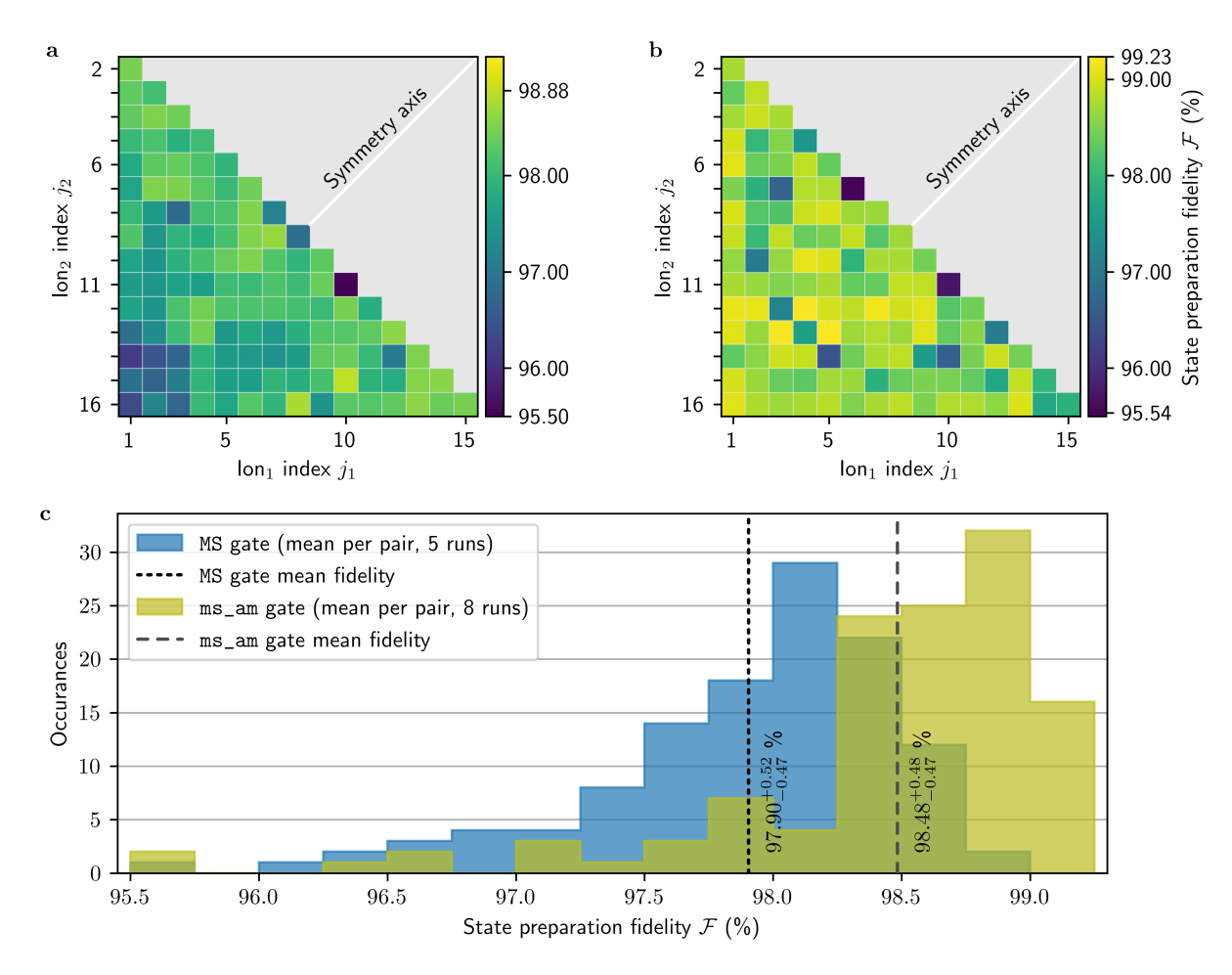


Figure 6.7.: Comparison of state preparation fidelities for each ion pair in **a** for the standard MS gate and in **b** for the ms\_am gate. Shown is the mean over 5 and 8 runs respectively. The scale of the colorbar is the same for both subfigures, with the minimum and maximum value indicated. **c**, Histogram for comparing the two gate implementations, with the dotted lines indicating the mean over all ion pairs. Errors are calculated by using the 68% quantile centered around the median of the data.

# 7. Conclusion and outlook

The aim of this work was to implement high-fidelity MS gate operations for optical qubits in  $^{40}$ Ca<sup>+</sup> and this was accomplished via amplitude modulation as an example of an optimal control solution to this problem. To this end, the necessary theoretical background was introduced in Chap. 2 such that the underlying control problem can be formulated both in the abstract language of control theory as well as in the setting of trapped-ion quantum information processors. This was followed in Chap. 3 by a brief description of the components of the AQTION setup relevant to two-qubit gates. In particular, the hard- and software necessary for generating RF signals was described, as AOMs controlled by these RF signals enable the execution of coherent operations on the qubit register.

The results from numerical simulations for a 16-ion chain were presented in Chap. 4 to identify the main error sources affecting the entangling gate operation in the setup. The main contribution to the gate infidelity, aside from the motional/optical coherence with respectively 0.41 %/0.60 %, was identified to be the residual spin-motional coupling of radial modes with an average contribution to the gate infidelity of 0.57 % per ion pair. In its current form, the numerical simulation assumes a rectangular pulse shape for simplicity. A natural extension of this work would be to incorporate the Blackman window for the rising and falling edges of the standard MS gate, as this would align the simulation with the waveform used in the experiment. Moreover, the current model only accounts for the radial-y COM mode in the evaluation of the motional coherence and the heating rate. Modifying the simulation to include multiple motional modes and incorporating additional effects such as off-resonant carrier excitation could provide a more accurate estimation of the dominant error mechanisms limiting the fidelity achieved in the experiment. This will become especially important after a planned hardware upgrade, where the magnetic field generation is changed from coils to permanent magnets, in turn reducing the decoherence induced by magnetic field fluctuations. However, the  $\approx 1 \,\mathrm{s}$  lifetime of the metastable state in  $^{40}\mathrm{Ca}^+$  sets an upper limit to the achievable coherence time and hence to the gate performance. This influence can only be reduced by either reducing the gate time relative to a given coherence time or by extending the coherence time by either changing to a ground state qubit in <sup>40</sup>Ca<sup>+</sup>, or by using a different qubit isotope/species like <sup>43</sup>Ca<sup>+</sup> or <sup>137</sup>Ba<sup>+</sup>.

Based on these simulations, frequency-robust entangling gates using amplitude modulation were introduced as one possible optimal control method to reduce the infidelity coming from residual mode coupling. An advantage of this scheme is that the RF pulse, which follows a Gaussian waveform in Rabi frequency, can be described by a small set of parameters, simplifying both the implementation in hardware as well as the numerical simulation. This numerical simulation of the gate dynamics was then described, supporting experimental calibration procedures to calibrate the required power and the detuning. The characterization of the ARTIQ and Sinara ecosystem was presented in Chap. 5 and guided the selection for the chosen optimal control method. First, the RF generation capabilities of the Phaser hardware module were outlined, followed by experimental tests using a DP-AOM unit. Overshooting behaviour and oscillations in the rising and falling slope were observed for rectangular signals, but are minimized/removed

#### 7. Conclusion and outlook

when smaller amplitude target values were used. Additionally it was shown that one can achieve amplitude parameter updates every 275 ns by using the built-in DMA feature of Sinara, which is short enough to sufficiently approximate continuous functions like the Gaussian waveform required for the chosen optimal control technique in this thesis. Furthermore, it was found that phase changes cause at least a 20 % reduction in laser beam intensity even though it should remain constant. Expanding the characterization of these reductions to varying RF output amplitudes could offer additional insights into the feasibility of phase modulation sequences. Further research directions would involve the characterization of frequency changes and their impact on the laser beam intensity, possibly opening up frequency modulation schemes for testing.

Experimental results from the AQTION setup were covered in Chap. 6 and divided into data for a 2- and 16-ion chain. First, the mapping between the output amplitude of Phaser and the corresponding Rabi frequency was obtained in order to realize a Gaussian waveform in Rabi frequency that is required for the optimal control technique. The robustness against motional mode frequency drifts was then investigated, showing for the standard MS gate a  $\approx 800\,\mathrm{Hz}$  wide region around the ideal detuning where the fidelity exceeded 90 %. The ms\_am gate extends the region significantly to  $20\,\mathrm{kHz}$ , with the improvement in fidelity being smaller but still present for typical motional mode frequency changes of  $\pm 250\,\mathrm{Hz}$ . Furthermore, an effective error rate was obtained from the decay in state preparation fidelity over different numbers of consecutive gates. The measured error rates were  $\varepsilon_{\mathrm{MS}} = 0.73(10)\,\%$  for the standard MS gate and  $\varepsilon_{\mathrm{ms_am}} = 0.31(3)\,\%$  for the ms\_am gate. Different shaping parameters introduced by the system migration to the Sinara ecosystem resulted in a calibration error related to the ideal gate time and limited the performance of the standard MS gate. This issue was rectified for the 16-ion chain, enabling a fair comparison of both gate implementations.

For the 16-ion chain, which is the usual number of ions in the AQTION setup, a calibration method was introduced that enables the time-efficient calibration of all 120 ion pairs. Taking the detuning from numerical simulation, the required power for all 120 pairs was measured once. Then based on the required power of a reference pair, the power of all other 119 pairs is updated. Using this technique, the mean fidelity over all 120 pairs was determined to  $97.90^{+0.52}_{-0.47}\%$  for the standard MS gate and to  $98.48^{+0.48}_{-0.47}\%$  for the ms\_am gate, showing an improvement when using the modulation scheme with the difference in fidelity between implementations aligning with simulation results.

While our results are promising, opportunities for improvement persist in several areas. For example, in all experiments a sample period of 500 ns was used instead of a multiple of the Phaser frame time of 320 ns. As illustrated in Fig. 5.4, this leads to aliasing from resampling to the Phaser frame time that could possibly deteriorate the gate performance when the carrier transition is unintentionally excited by this frequency component. Despite the simulation suggesting a negligible difference in fidelity between ion pairs, the observed lower fidelity in some pairs remains unexplained. One potential explanation for this discrepancy could be a mismatch between the balance-point detuning from simulation and the experiment, arising from an incomplete model of the underlying system. Dedicated detuning scans for all ion pairs could reveal further insights into this matter and narrow down the possible cause of the discrepancy.

Improvements to the calibration technique itself can be realized by revising how the required power for all pairs is obtained in the beginning. Repeated power scans may induce thermal effects in the optical devices, which in turn can result in instabilities and a subsequent decrease in the power that is incident on the ions. Obtaining the required power of a pair relative to the reference pair would have the potential benefit of accounting for this shift in power. There

#### 7. Conclusion and outlook

may also be merit in accounting for a non-linear scaling similar to Ref. 36, which has already been shown to improve the performance in a different calibration technique. While out of the scope of this work, it would also be beneficial to investigate how different amplitude shapes influence the gate behaviour. From a theoretical standpoint, using a Slepian window instead of a Gaussian waveform should result in lower power requirements for the gate implementation. This is because as the eigenfunction of the discrete Fourier transform, this function provably maximizes the energy contained in the main lobe [63], but it remains to be seen if this translates to an experimental setting.

It was stated in the introduction of this thesis that one of the outstanding challenges in quantum computing is scaling up the number of qubits while at the same time reducing errors induced by the control field. While this thesis presented results showing improvements in the fidelity for a given ion number, it remains to be seen how well the ms\_am gate performs for larger ion numbers in the experiment. This is insofar an interesting question as one of the main limitations in having higher ion numbers confined in the same trapping potential is that the fidelity of the entangling gate operation drops significantly due to mode crowding. As there is no proof that every ion pair has a solution for a high-fidelity ms\_am gate, it could be necessary to lift the requirement of all pairs having the same gate time and width.

# A. Analysis method for parity oscillations

In this thesis, the state preparation fidelity of maximally entangled states was used as an estimate for the gate fidelity following [27, 64]. As described in Sec. 2.2.3, the state preparation fidelity  $\mathcal{F}$  is given by the average of the population  $P = p_{00} + p_{11}$  and the coherence C as  $\mathcal{F} = (P + C)/2$ . The coherence in turn is given by the amplitude of parity oscillations

$$\mathcal{P}(\varphi, \{C, \varphi_0\}) = C\cos(N_{\mathcal{P}}\varphi + \varphi_0), \tag{A.1}$$

with  $N_{\mathcal{P}}=2$  the number of qubits in the maximally entangled state (not the number of ions in the chain N!), the phase  $\varphi$  and a phase offset  $\varphi_0$ . The parity oscillation measurements in this thesis consist of  $n_p=30$  equidistant phases  $\varphi=\{\varphi_i\,|\,i=1,\ldots,n_p\}$ , for which the mean population over  $n_s=100$  measurements is returned. One scan thus consists of 3000 individual measurements and the parity is then given for each phase by  $\mathcal{P}(\varphi_i)=p_{00}(\varphi_i)+p_{11}(\varphi_i)-p_{10}(\varphi_i)-p_{01}(\varphi_i)$ . Instead of directly using the parity  $\mathcal{P}(\varphi_i)\in[-1,1]$ , we will use the probability  $p(\varphi_i)\in[0,1]$  of measuring a positive parity. We are interested in obtaining estimates for the coherence C and the phase offset  $\varphi_0$  with

$$p(\varphi, \{C, \varphi_0\}) = \frac{1}{2} \left[ 1 + C \cos(N_{\mathcal{P}} \cdot \varphi + \varphi_0) \right], \tag{A.2}$$

utilizing three different evaluation methods in this thesis. The first two approaches rely on a least-square fitting routine, where estimates for the most-likely coherence  $C^f$  and phase offset  $\varphi_0^f$  are obtained by minimizing the function

$$C^{f}, \varphi_{0}^{f} = \arg\min_{C, \varphi_{0}} \sum_{i=1}^{n_{p}} \frac{\left[p(\varphi_{i}, \{C, \varphi_{0}\}) - p(\varphi_{i})\right]^{2}}{\Delta p(\varphi_{i})^{2}}.$$
(A.3)

Here,  $w_i = 1/\Delta p(\varphi_i)^2$  is the weight assigned to each data point. In the first unweighted fit method, all data points are treated with equal weight by setting  $w_i = \Delta p(\varphi_i)^2 = 1$ . One shortcoming of this method is that it doesn't take into account the finite amount of measurements  $(n_s = 100)$  and the obtained value of the probability  $p(\varphi_i)$  for determining the errors or variance of the fit parameters. Given that  $p(\varphi_i)$  can be identified as a binomial distribution with two outcomes (either positive parity has been observed or not), the variance of the mean is given by

$$\Delta p(\varphi_i) = \max\left\{\sqrt{\frac{p(\varphi_i)(1 - p(\varphi_i))}{n_s}}, \frac{1}{n_s + 2}\right\}.$$
(A.4)

The first part is referred to as quantum projection noise [65] and is equivalent to the "Wald" binomial proportion confidence interval using a normal approximation [66]. One disadvantage of using this confidence interval is that the variance would vanish for probabilities 0 and 1. As such the definition is expanded by Laplace's "Rule of Succession", which sets a lower bound to the variance depending on the number of measurements  $n_s$  [67].

The third method uses Bayesian interference and aims to maximize the *posterior* probability P(model|data), such that the probability of the model  $p(\varphi, \{C, \varphi_0\})$  describing the data from the experiment  $p(\varphi)$  is highest. For this Bayes' theorem is used

$$P(\text{model}|\text{data}) = \frac{P(\text{data}|\text{model})P(\text{model})}{P(\text{data})},$$
(A.5)

with the *prior* probability P(model) indicating the knowledge about the most likely model before any data from the experiment is taken into account. We opted for a flat prior with P(model) = 1, however choosing a "noninformed" prior is a challenging task [68]. The prior is then updated by the likelihood P(data|model) of the experimental data describing the model and is given by

$$P[\varphi | p(\varphi, \{C, \varphi_0\})] = \prod_{i=1}^{n_p} P[\varphi_i | p(\varphi_i, \{C, \varphi_0\})]$$
(A.6)

$$= \prod_{i=1}^{n_p} \beta \left[ p(\varphi_i, \{C, \varphi_0\}), p(\varphi_i), n_p \right]. \tag{A.7}$$

Given that the data follows a binomial distribution, the probability mass function is given by

$$\beta\left[p := p(\varphi_i, \{C, \varphi_0\}), p(\varphi_i), n_p\right] = \binom{n_p}{p(\varphi_i)} p^{p(\varphi_i)} (1-p)^{n_p - p(\varphi_i)}, \tag{A.8}$$

and returns the likelihood that a certain coherence and phase offset are describing the obtained probability  $p(\varphi_i)$ . Both the coherence 0 < C < 1 and the phase offset  $0 \le \varphi_0 < 2\pi$  are inherently bounded and this is considered by evaluating Eq. A.7 within this bounds<sup>1</sup>. For computational purposes, the logarithm of the likelihood is considered, which transforms the product into a sum. The normalization factor P(data) in Eq. A.5 is called marginal likelihood and ensures that the grid containing the likelihood for combinations of the coherence and phase offset is normalized to one. The probability distribution function for the coherence  $\text{tr}_{\varphi_0}(P\left[\varphi \mid p(\varphi, \{C, \varphi_0\})\right])$  and the phase offset  $\text{tr}_C(P\left[\varphi \mid p(\varphi, \{C, \varphi_0\})\right])$  is obtained by tracing out the respective other parameter, which simply means summing up along different axes in the program. From those functions, the mean  $C^f$  and the standard deviation  $(\delta C^f)^2$  (similar for  $\varphi_0^f$  and  $(\delta \varphi_0^f)^2$ ) is given by

$$C^{f} = \int_{0}^{1} dC C \operatorname{tr}_{\varphi_{0}}(P[\varphi | p(\varphi, \{C, \varphi_{0}\})],$$
(A.9)

$$(\delta C^f)^2 = \int_0^1 dC \, (C - C^f)^2 \, \operatorname{tr}_{\varphi_0}(P \, [\varphi \, | \, p(\varphi, \{C, \, \varphi_0\})] \,. \tag{A.10}$$

All presented results in Chap. 6 show the state preparation fidelity obtained via the Bayesian fitting method. The rest of this chapter will show the same results but with all three fitting methods and we will discuss, why the Bayesian method was chosen in the main text. First, the error rate is shown for all fit methods in Fig. A.1a for the MS gate and in b for the ms\_am gate, with the corresponding Fig. 6.4 in the main text. From this it becomes apparent that the weighted fit indicates the lowest error rate, while the unweighted and Bayesian fit methods yield similar results in both their estimate as well as their uncertainty.

<sup>&</sup>lt;sup>1</sup>Evaluating the complete parameter space numerically would be too time consuming. We instead obtain estimates for the coherence and phase offset from the unweighted fit and consider only a region around this estimates in the evaluation of the likelihood.

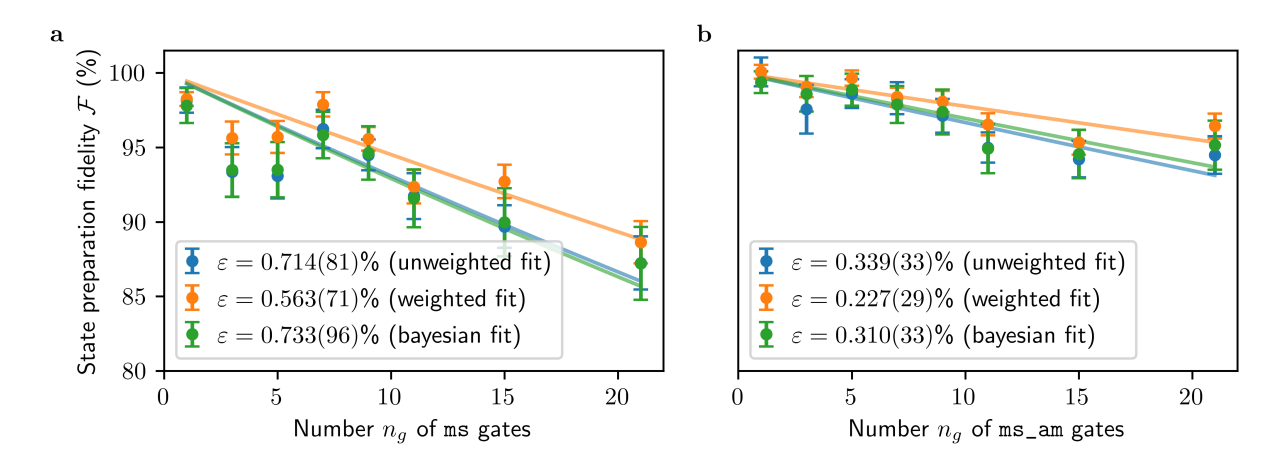


Figure A.1.: Measured error rates  $\varepsilon$  for entangling gates with a gate time of  $\tau = 300 \,\mu\text{s}$ , showing the result for all three fit methods. **a**, Error rate for the standard MS gate with a detuning of  $\delta = 1/304 \,\mu\text{s}$  relative to the radial-y COM mode. **b**, Error rate for the ms\_am gate with a detuning of  $\delta = -97.1 \,\text{kHz}$  and a Gaussian width of  $\sigma = 50 \,\mu\text{s}$ .

Next, the state preparation fidelity for all 120 pairs of a 16-ion chain is shown in Fig. A.2a for the MS gate (averaged over 5 runs) and in b for the ms\_am gate (averaged over 8 runs). For both gate implementations, the weighted fit returns a  $\approx 1.2\,\%$  higher mean state preparation fidelity compared to the other two methods. The reason for this is that probabilities close to either zero or one have a higher weight, which in some cases leads to a nonphysical coherence above one and in general increases the obtained state preparation fidelities. Both the unweighted as well as the Bayesian fit lead to similar results, with the uncertainty being smaller in the Bayesian method.

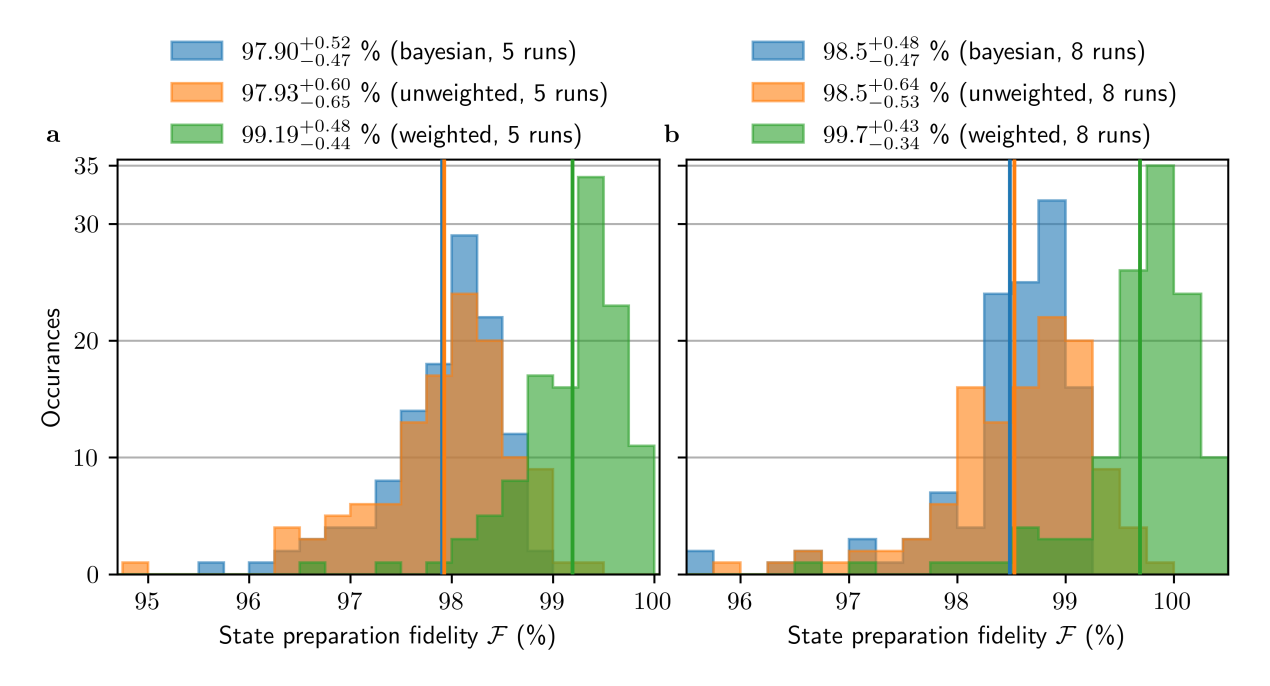


Figure A.2.: Comparison of state preparation fidelities for each ion pair in **a** for the standard MS gate and in **b** for the ms\_am gate for all three fit methods. Shown is the mean over 5 and 8 runs respectively.

Last, a correlation analysis using the Pearson correlation coefficient  $\rho$  was carried out between results from the different fit methods. For two random variables x and y it is given by the expression

$$\rho(x,y) = \frac{\text{Cov}(x,y)}{\sigma_x \sigma_y},\tag{A.11}$$

where  $\mathrm{Cov}(x,y)$  is the covariance and  $\sigma_x$  and  $\sigma_y$  the standard deviation of the respective random variable [69]. The result of the correlation analysis is shown in Fig. A.3a for the MS gate and in **b** for the ms\_am gate, showing a strong linear correlation of  $\rho > 0.88$  between all obtained results. One the one hand this shows that the obtained results for the state preparation fidelity are consistent between fitting methods for the same underlying data, on the other hand these results suggest that the choice of a particular fit method should be chosen by careful consideration beyond numerical results.

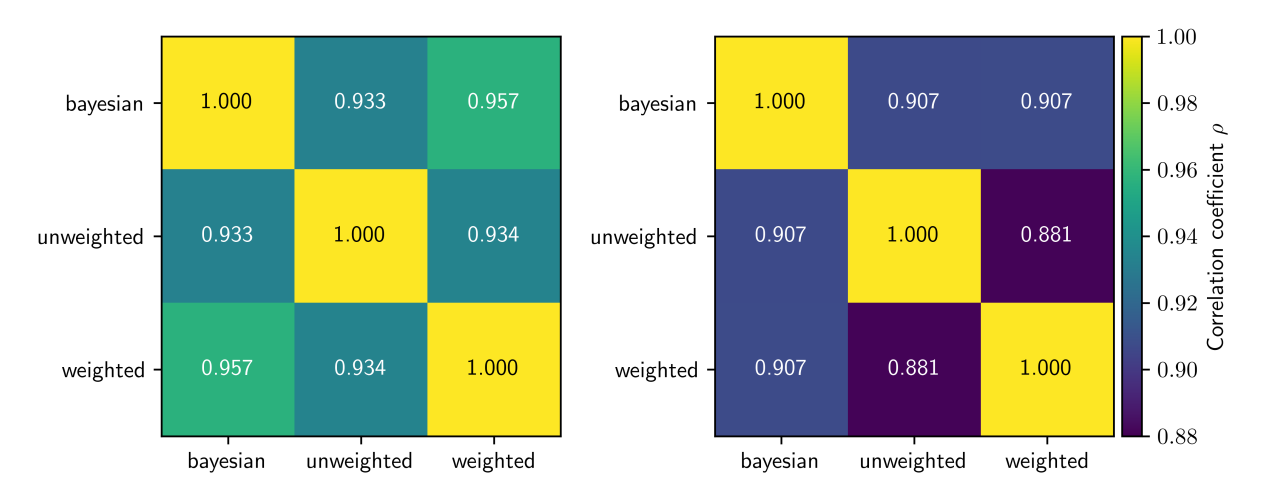


Figure A.3.: Correlation coefficient  $\rho$  for the MS gate in **a** and for the ms\_am gate in **b**, showing a strong correlation with  $\rho > 0.88$  between different fitting methods.

The Bayesian fit method was chosen for the main text because it conservatively estimates the state preparation fidelity, while taking the inherent bounds for the coherence and phase offset into account. Given that the results are similar to the unweighted fit, the unweighted fit method would be however preferable as a quick analysis tool as it takes significantly less time to obtain the results. Furthermore, the weighted fit is based on the quantum projection noise and a heuristic lower error bound given by Laplace's "Rule of Succession". One could instead use the "Wilson Score Interval" to obtain error estimates for the individual parameters, which doesn't rely on the normal approximation and would more accurately reflect the true error bounds [66].

# **B.** Bibliography

- [1] DERA Deutsche Rohstoffagentur in der Bundesanstalt für Geowissenschaften und Rohstoffe, Silizium und Ferrosilikolegierungen – Zwischenprodukte auf Basis von Quarz, tech. rep. 59, Datenstand: Oktober 2023 (DERA Rohstoffinformationen, Berlin, 2023), p. 238.
- [2] E. Sharma, R. Rathi, J. Misharwal, et al., "Evolution in Lithography Techniques: Microlithography to Nanolithography", Nanomaterials 12, 2754 (2022).
- [3] J. P. Dowling and G. J. Milburn, "Quantum technology: the second quantum revolution", Philosophical Transactions of the Royal Society of London. Series A: Mathematical, Physical and Engineering Sciences **361**, 1655–1674 (2003).
- [4] P. Shor, "Algorithms for quantum computation: discrete logarithms and factoring", in Proceedings 35th Annual Symposium on Foundations of Computer Science (1994), pp. 124–134.
- [5] R. Landauer, "Information is a physical entity", Physica A: Statistical Mechanics and its Applications 263, Proceedings of the 20th IUPAP International Conference on Statistical Physics, 63–67 (1999).
- [6] I. L. Chuang, N. Gershenfeld, and M. Kubinec, "Experimental Implementation of Fast Quantum Searching", Physical Review Letters 80, 3408–3411 (1998).
- [7] J. Clarke and F. K. Wilhelm, "Superconducting quantum bits", Nature **453**, 1031–1042 (2008).
- [8] L. Henriet, L. Beguin, A. Signoles, et al., "Quantum computing with neutral atoms", Quantum 4, 327 (2020).
- [9] J. I. Cirac and P. Zoller, "Quantum computations with cold trapped ions", Physical Review Letters 74, 4091–4094 (1995).
- [10] F. Schmidt-Kaler, H. Häffner, M. Riebe, et al., "Realization of the Cirac-Zoller controlled-NOT quantum gate", Nature 422, 408–411 (2003).
- [11] J. J. DiStephano, Schaum's outline of feedback and control systems, 2nd ed, McGraw-Hill's AccessEngineering (McGraw-Hill, New York, 2014).
- [12] D. E. Kirk, *Optimal control theory: an introduction*, first published in 2004, unabridged republication of the thirteenth printing (Dover Publications, Mineola, N.Y, 2004).
- [13] M. A. Nielsen and I. L. Chuang, Quantum computation and quantum information, 10th anniversary edition (Cambridge university press, Cambridge, 2010).
- [14] C. Marquet, F. Schmidt-Kaler, and D. James, "Phonon-phonon interactions due to non-linear effects in a linear ion trap", Applied Physics B: Lasers and Optics **76**, 199–208 (2003).
- [15] D. Leibfried, R. Blatt, C. Monroe, et al., "Quantum dynamics of single trapped ions", Reviews of Modern Physics **75**, 281–324 (2003).
- [16] B. Tyff, "Randomised Measurements with Strings of Trapped Ions", Available at http://quantumoptics.at., PhD thesis (University of Innsbruck, 2021).
- [17] C. J. Foot, *Atomic Physics*, Oxford Master Series in Atomic, Optical and Laser Physics (Oxford Univ. Press, Oxford, 2011).
- [18] C. Hempel, "Digital quantum simulation, Schrödinger cat state spectroscopy and setting up a linear ion trap", PhD thesis (University of Innsbruck, 2014).

- [19] D. James, "Quantum Computation with Hot and Cold Ions: An Assessment of Proposed Schemes", Fortschritte der Physik 48, 823–837 (2000).
- [20] D. C. McKay, C. J. Wood, S. Sheldon, et al., "Efficient Z gates for quantum computing", Physical Review A **96**, 022330 (2017).
- [21] A. Sørensen and K. Mølmer, "Quantum Computation with Ions in Thermal Motion", Physical Review Letters 82, 1971–1974 (1999).
- [22] G. Kirchmair, J. Benhelm, F. Zähringer, et al., "Deterministic entanglement of ions in thermal states of motion", New Journal of Physics 11, 023002 (2009).
- [23] C. Langer, "High Fidelity Quantum Information Processing with Trapped Ions", PhD thesis (University of Colorado, 2006).
- [24] A. Sørensen and K. Mølmer, "Entanglement and quantum computation with ions in thermal motion", Physical Review A **62**, 022311 (2000).
- [25] C. F. Roos, "Ion trap quantum gates with amplitude-modulated laser beams", New Journal of Physics **10**, 013002 (2008).
- [26] Y. Wu, S.-T. Wang, and L.-M. Duan, "Noise analysis for high-fidelity quantum entangling gates in an anharmonic linear Paul trap", Physical Review A 97, 062325 (2018).
- [27] T. Monz, P. Schindler, J. T. Barreiro, et al., "14-Qubit Entanglement: Creation and Coherence", Physical Review Letters 106, 130506 (2011).
- [28] C. Roos, "Controlling the quantum state of trapped ions", PhD thesis (University of Innsbruck, 2000).
- [29] F. G. Major, V. N. Gheorghe, and G. Werth, *Charged particle traps: physics and techniques of charged particle field confinement* (Springer, Berlin; New York, 2005).
- [30] A. Steane, "The ion trap quantum information processor", Applied Physics B: Lasers and Optics 64, 623–643 (1997).
- [31] D. James, "Quantum dynamics of cold trapped ions with application to quantum computation", Applied Physics B: Lasers and Optics **66**, 181–190 (1998).
- [32] S. Gulde, D. Rotter, P. Barton, et al., "Simple and efficient photo-ionization loading of ions for precision ion-trapping experiments", Applied Physics B 73, 861–863 (2001).
- [33] J. Jin and D. A. Church, "Precision lifetimes for the Ca<sup>+</sup> 4p <sup>2</sup>P levels: Experiment challenges theory at the 1% level", Physical Review Letters **70**, 3213–3216 (1993).
- [34] P. A. Barton, C. J. S. Donald, D. M. Lucas, et al., "Measurement of the lifetime of the  $3d^2D_{5/2}$  state in  $^{40}Ca^+$ ", Physical Review A **62**, 032503 (2000).
- [35] S. Stenholm, "The semiclassical theory of laser cooling", Reviews of Modern Physics 58, 699–739 (1986).
- [36] I. Pogorelov, "Quantum error correction in a compact ion-trap quantum computer", PhD thesis (University of Innsbruck, 2025).
- [37] D. Wineland and H. Dehmelt, "Proposed  $10^{14} \Delta \nu < \nu$  laser fluorescence spectroscopy on TI<sup>+</sup> mono-ion oscillator II", in Bulletin of the american physical society, Vol. 20(4) (1975), p. 637.
- [38] H. Häffner, S. Gulde, M. Riebe, et al., "Precision Measurement and Compensation of Optical Stark Shifts for an Ion-Trap Quantum Processor", Physical Review Letters **90**, 143602 (2003).
- [39] F. Harris, "On the use of windows for harmonic analysis with the discrete Fourier transform", Proceedings of the IEEE **66**, 51–83 (1978).
- [40] L. Gerster, F. Martínez-García, P. Hrmo, et al., "Experimental Bayesian Calibration of Trapped-Ion Entangling Operations", PRX Quantum 3, 020350 (2022).

- [41] A. Kaplan, M. Fredslund Andersen, and N. Davidson, "Suppression of inhomogeneous broadening in rf spectroscopy of optically trapped atoms", Physical Review A 66, 045401 (2002).
- [42] I. Pogorelov, T. Feldker, C. D. Marciniak, et al., "Compact Ion-Trap Quantum Computing Demonstrator", PRX Quantum 2, 020343 (2021).
- [43] M-Labs, 1124 Carrier Kasli 2.0 Datasheet, https://m-labs.hk/docs/sinara-datasheets/1124.pdf, 2024.
- [44] M-Labs, 2118 BNC-TTL / 2128 SMA-TTL Datasheet, https://m-labs.hk/docs/sinara-datasheets/2118-2128.pdf, 2022.
- [45] Joe Britton, Grabber Sinara Hardware Repository, https://github.com/sinara-hw/Grabber/wiki, accessed on 05.01.2025, 2020.
- [46] G. Kasprowicz, T. Harty, S. Bourdeauducq, et al., "Urukul Open-source Frequency Synthesizer Module for Quantum Physics", International Journal of Electronics and Telecommunications, 123–128 (2021).
- [47] Analog Devices, Inc., A Technical Tutorial on Digital Signal Synthesis, https://www.analog.com/media/cn/training-seminars/tutorials/450968421DDS\_Tutorial\_rev12-2-99.pdf, 1999.
- [48] Analog devices, Datasheet AD9910, https://www.analog.com/media/en/technical-documentation/data-sheets/AD9910.pdf, 2008.
- [49] Joe Britton, *Phaser Sinara Hardware Repository*, https://m-labs.hk/experiment-control/sinara-chttps://github.com/sinara-hw/Phaser/wiki/, accessed on 05.01.2025, 2022.
- [50] N. Krackow, "Short Time Fourier Transform Pulse Generator for Trapped Ion Quantum Computing", Master's Thesis (Technische Universität Berlin, 2020).
- [51] B. P. Ruzic, M. N. Chow, A. D. Burch, et al., "Leveraging motional-mode balancing and simply parametrized waveforms to perform frequency-robust entangling gates", Physical Review Applied 22, 014007 (2024).
- [52] D. Manzano, "A short introduction to the Lindblad master equation", AIP Advances 10, 025106 (2020).
- [53] J. Johansson, P. Nation, and F. Nori, "QuTiP: An open-source Python framework for the dynamics of open quantum systems", Computer Physics Communications 183, 1760–1772 (2012).
- [54] H. Haffner, C. Roos, and R. Blatt, "Quantum computing with trapped ions", Physics Reports 469, 155–203 (2008).
- [55] A. R. Milne, C. L. Edmunds, C. Hempel, et al., "Phase-Modulated Entangling Gates Robust to Static and Time-Varying Errors", Physical Review Applied 13, 024022 (2020).
- [56] M. Kang, Q. Liang, B. Zhang, et al., "Batch Optimization of Frequency-Modulated Pulses for Robust Two-Qubit Gates in Ion Chains", Physical Review Applied 16, 024039 (2021).
- [57] L. Cheng, S.-C. Liu, L. Geng, et al., "Robust segmented entangling gates with pulse gradient and power optimization using a hypersurface-tangent method", Physical Review A 107, 042617 (2023).
- [58] Jonah-Foley, *Phaser Baseband AA Filter Specification*, https://github.com/sinara-hw/Phaser/issues/158, accessed on 26.02.2025, 2024.
- [59] SingularitySurfer, *Phaser DSP Gateware*, https://github.com/quartiq/phaser/wiki, accessed on 26.02.2025, 2021.
- [60] M-Labs, ARTIQ Core Drivers Reference Phaser Module, https://m-labs.hk/artiq/manual/core\_drivers\_reference.html, accessed on 27.02.2025, 2025.

- [61] M-Labs, ARTIQ Real-Time Input/Output (RTIO), https://m-labs.hk/artiq/manual/rtio.html, accessed on 26.02.2025, 2025.
- [62] L. Postler, F. Butt, I. Pogorelov, et al., "Demonstration of Fault-Tolerant Steane Quantum Error Correction", PRX Quantum 5, 030326 (2024).
- [63] D. Slepian and H. O. Pollak, "Prolate Spheroidal Wave Functions, Fourier Analysis and Uncertainty I", Bell System Technical Journal 40, 43–63 (1961).
- [64] T. Monz, "Quantum information processing beyond ten ion-qubits", PhD thesis (University of Innsbruck, 2011).
- [65] W. M. Itano, J. C. Bergquist, J. J. Bollinger, et al., "Quantum projection noise: Population fluctuations in two-level systems", Physical Review A 47, 3554–3570 (1993).
- [66] S. Wallis, "Binomial Confidence Intervals and Contingency Tests: Mathematical Fundamentals and the Evaluation of Alternative Methods", Journal of Quantitative Linguistics 20, 178–208 (2013).
- [67] S. L. Zabell, "The rule of succession", Erkenntnis 31, 283–321 (1989).
- [68] R. E. Kass and L. Wasserman, "The Selection of Prior Distributions by Formal Rules", Journal of the American Statistical Association 91, 1343–1370 (1996).
- [69] K. Pearson, "VII. Mathematical contributions to the theory of evolution.—III. Regression, heredity, and panmixia", 187, 253–318 (1896).